Seismic Imaging of Sandbox Models

Dissertation
zur Erlangung des akademischen Doktorgrades
doctor rerum naturalium (Dr. rer. nat.)
im Fachbereich Geowissenschaften
der Freien Universität Berlin
vorgelegt von

Maike-Liselotte Buddensiek

Berlin, Februar 2009

Tag der Disputation: 27. Februar 2009

Gutachter

Prof. Dr. Onno Oncken (1. Gutachter)
Freie Universität Berlin, GeoForschungsZentrum Potsdam

Prof. Dr. Charlotte Krawczyk (2. Gutachter)
Technische Universität Berlin, LIAG Hannover

Die Probleme der modernen Wissenschaft sind nun mal nicht komisch.

Loriot

Ich versichere, daß ich die vorliegende Arbeit selbständig verfaßt und kein anderes als die angegebenen Hilfsmittel genutzt habe. Die Stellen der Arbeit, die anderen Werken wörtlich oder inhaltlich entnommen wurden, sind durch entsprechende Quellenangaben gekennzeichnet. Diese Arbeit hat in gleicher oder ähnlicher Form noch keiner Prüfungsbehörde vorgelegen.

(Maike-Liselotte Buddensiek, Februar 2009)

Contents

Summary

Analog sandbox simulations have been applied to achieve qualitative and quantitative insight into geological processes occurring in compressional and extensional settings. A direct comparison of model and nature is possible, because suitable analog materials, such as sand or glass beads, exhibit a similar Mohr-Coulomb behavior as sediments and rocks of the upper crust. Thus, analog models are scaled geometrically to nature by the density and frictional properties of the material used in the experiments. For example, to study the evolution of accretionary wedges in subduction zones, a typical experimental apparatus consists of a fixed horizontal plate (few meters $\times$ few decimeters) on which a conveyor belt, representing the subducting oceanic plate, is dragged underneath a rigid back wall, acting as the rigid part of the continental margin. The sand, representing deposited sediments, is sieved in layers onto the conveyer belt, and upon convergence, accumulates in regular imbricates in front of the back wall. Internal structures of sandbox models and their temporal evolution can only be directly observed in 2-D profiles along the glass walls confining the experiment or indirectly by surface observations by means of particle imaging velocimetry (PIV). When investigating regimes with along-strike variations, 3-D information of the sand models is needed, but can only be obtained by either very expensive and very elaborate X-ray tomography on small models (few centimeters), or, after the deformation is finished, by solidifying the model with transparent resin and cutting slices. This method provides high resolution 2-D slices to analyze 3-D structures. However, after solidification, further deformation of the model is impossible.

To extend the simulations to three dimensions, I perform non-invasive seismic physical modeling on these analog sandbox models. The long-term objective of this approach is to image seismic and seismological events of static and actively deforming 3-D analog models. To achieve this objective, a new small-scale seismic apparatus, composed of a water tank, a PC control unit including piezo-electric transducers (PETs), and a positioning system, was built for laboratory use. To build the models, I use granular materials such as quartz sand, garnet sand and glass beads, so that brittle deformation can take place. Unlike typical analog sandbox models, the granular models now are required to be completely water saturated so that the sources and receivers are directly and well coupled to the propagating medium. Ultrasonic source frequencies ($\sim$500 kHz) corresponding to wavelengths $\sim$5 times the grain diameter are necessary to be able to resolve small scale structures. When thus doing seismic physical modeling of granular models, two aspects besides the model scaling require particular attention to assess the feasibility of this setup and method: The transducer properties with respect to their use in seismic reflection surveys on mm-scale, and the acoustic material properties.

The properties of specially designed PETs with reduced directionality were tested to assess their feasibility for seismic profiling on millimeter-scale with respect to their frequency sensitivity, their directionality, and the change of waveform as a function of offset. The experiments show that the PETs produce the best quality data at frequencies around 350-550 kHz, which is sufficient to resolve structures of $\sim$2-1.5 mm dimension within saturated granular material. However, to inhibit ringing, a better control over the emitted source signal should be achieved. For these frequencies, the amplitudes decay to ringing noise level at incidence angles of $<35°$; for a 10 cm deep reflector that results in a 14 cm source-receiver offset. Below this offset, the first and second phase of the recorded signals still coincide so that a normal-movout correction during seismic data processing improves the signal. This shows that the special design of the PETs amounts to a reduced directionality compared to traditional transducers while maintaining the en-

ergy output. However, the energy output is fairly low for a highly attenuative material such as sand, so that the penetration depth is only 5 cm. Nevertheless, to this date, these are the most suitable transducers available to bridge the gap between the unwanted directionality and the desired energy output.

The acoustic properties of various granular materials are reviewed and tested experimentally in order to identify materials of sufficient impedance contrast. However, the sound velocity of various granular materials, such as quartz sand, garnet sand and glass beads, under atmospheric pressure is difficult to obtain. Only the velocity measurements of glass beads produce reasonable results of 1.8 km/s. The extreme variability of quartz and garnet sand prevents, that the true velocity can be deduced. The reason for this variability is that sound velocity primarily depends on the coordination number, which is a measure of the nature of the grain-to-grain contacts. Therefore, the velocity and attenuation are highly sensitive to small changes in packing, which are difficult to control when building a model. Hence, a reflection of an interface cannot be coerced by different acoustic velocities above and below the interface, but by an interface that has a contrasting coordination number compared to the model material above and below. The clearest reflections are generated in glass bead models where the interface is sprinkled with glass powder filling the intergranular space, and then graded flat. Seismic sections over layers made of glass beads contain less internal noise and attenuation than those made of sand due to the better sorting and smoother surface of glass beads compared to sand grains. Hence, the use of very well-sorted materials consisting of well-rounded grains, independent of mineralogy, reduces the inhomogeneities in packing and therefore improves the data quality.

Since it is not only desired to seismically image layer interfaces, but also shear bands within a deforming model, I show seismic images of a model before and after a string has been pulled through to simulate the decompaction occurring at shear bands. The decompaction of grains due to the string produces a reflection that can be detected in seismic data. The shear band is better resolved in sand than in glass beads. Different to field surveys, laboratory surveys are able to resolve the shear zone itself.

Finally, seismic reflection processing of a multiple-offset survey over a two-layer structural model containing channels and a shear band enhances the data quality and resolution significantly. This result is an improvement to previous studies, in which zero-offset surveys were conducted under the assumption that the directionality of the transducers impedes the advantages of multiple-offset data. Here, this assumption does not hold true due to the advanced PETs and to the survey geometry which is optimized to the properties of these particular PETs. However, especially for more complex models, the clarity and penetration depth need to be improved to study the evolution of geological structures in analog models with this method. As long as no source with a considerably higher energy output and spherical wave emission is available, I suggest to do ultrasonic seismic surveys across rather shallow models.

Nevertheless, even with model thicknesses above the penetration depth, the 3-dimensional albeit shallow information gained by seismic imaging of the models is feasible and would be beneficial in combination with PIV imaging, which provides a 2-D image of high spatial and temporal resolution over the entire depth of the model.

Zusammenfassung

Zur Erforschung der Gesetzmäßigkeiten, die die zeitliche und geometrische Entwicklung geologischer Strukturen in kompressiven und extensiven Regimes bestimmen, werden häufig analoge Modellsimulationen angewandt. Die direkte Vergleichbarkeit der Strukturen in Natur und Modell ist durch das Mohr-Coulomb-Verhalten der Gesteine der oberen Kruste sowie der Modellmaterialien gewährleistet. Für die Simulation geeignete Materialen, wie zum Beispiel Sand oder Glasperlen, bilden daher geometrisch skaliert dieselben Deformationsstrukturen wie die Kruste, sofern auch ihre Dichte und ihre Reibungskoeffizienten entsprechend skaliert sind. Ein typischer Experimentaufbau zur Analyse der Entwicklung von Akkretionskeilen, die an Subduktionszonen entstehen, besteht zum Beispiel aus einer feststehenden horizontalen Grundplatte (wenige Meter × wenige Zentimeter), auf der ein Förderband, das die ozeanische Platte repräsentiert, unter einer festen Rückwand, welche die kontinentale Platte darstellt, hindurchgezogen wird. Auf das Förderband wird in Schichten ein granulares Medium als Sediment gesiebt, das sich während der Subduktion des Förderbandes in Schuppen vor der Rückwand auftürmt. Die so entstandenen internen Strukturen und ihre zeitliche Entwicklung können direkt in 2-D Profilen durch die Glasscheiben, die das Experiment seitlich begrenzen, beobachtet werden, oder aber indirekt durch hoch aufgelöste Oberflächenbeobachtung mittels *Particle Imaging Velocimetry (PIV)*. 3-D Modelle, die Variationen in Streichrichtung aufweisen, können bisher nur mittels teurer und aufwendiger Röntgen-Tomographie während der Deformation aufgelöst werden. Alternativ ist es möglich, ein deformiertes Modell mit Kunstharz auszuhärten und anschließend in Scheiben zu schneiden, anhand derer ein 3-D Bild der Strukturen rekonstruiert werden kann. Eine weiterführende Deformation ist jedoch ausgeschlossen.

In der vorliegenden Arbeit wird das Ergebnis der Anwendung des seismischen Reflexionserkundungsverfahrens auf diese Analogmodelle gezeigt, um das Abbilden der Strukturen zerstörungsfrei auf 3-D zu erweitern. Die langfristigen Ziele sind hierbei das seismische und seismologische Abbilden von statischen und transienten Strukturen in 3-D Analogmodellen. Zu diesem Zweck wurde ein Experimentaufbau entwickelt, der aus einem Wassertank, einer Computersteuerung, piezoelektrischen Sensoren und einem Positionierungssystem besteht. Um eine Mohr-Coulomb Deformation zu ermöglichen, bestehen die Modelle auch hierfür aus granularen Medien wie Quartzsand, Granatsand und Glasperlen. Für diese Anwendung müssen die Modelle jedoch vollständig wassergesättigt sein, damit die Sensoren, die als Quelle und Empfänger dienen, direkt und gut an das Modell gekoppelt sind. Die Quellfrequenz liegt um 500 kHz, damit die resultierende Wellenlänge kleinskalige Strukturen einer Größe von ungefähr fünf Korndurchmessern auflösen kann. Um die Anwendbarkeit dieser Methode auf Analogmodelle zu beurteilen, müssen erstens die Eigenschaften der Sensoren in Bezug auf ihre Anwendung in Reflexionsexperimenten auf Millimeter-Skala untersucht werden. Zweitens müssen die granularen Medien nach ihren akustischen Eigenschaften in diesem Frequenzbereich ausgesucht werden.

Die Anwendbarkeit dieser speziell für diesen Zweck entwickelten piezoelektrischen Sensoren in seismischen Reflexionsexperimenten auf Millimeter-Skala hängt von ihrer Frequenzsensitivität, ihrem Abstrahlverhalten und der Änderung der aufgezeichneten Wellenform mit dem Quell-Empfänger-Abstand ab. Die Messung dieser Eigenschaften ergibt, daß die Sensoren im Frequenzbereich von 350-550 kHz das beste Signalverhalten aufweisen. Damit sind die Sensoren geeignet, um innerhalb von gesättigtem Sand,

Strukturen von ungefähr 2 mm Mächtigkeit aufzulösen. Trotzdem ist eine verbesserte Kontrolle über das emittierte Signal wünschenswert, die die Resonanzvibrationen stärker unterdrückt. Innerhalb dieses Frequenzbereichs nehmen die Amplituden ab Einfallswinkeln von $<35°$ auf das Niveau des Rauschens ab. Das bedeutet bei einer Reflektortiefe von 10 cm, daß das reflektierte Signal bis zu einem Quell-Empfänger-Abstand von 14 cm noch erkannt werden kann. Innerhalb dieses Abstandes interferieren die erste und zweite Phase des eingegangen Signals, so daß eine *Normal-Moveout (NMO)* Korrektur zu einer Verbesserung des Signal/Rauschen-Verhältnisses führt. Dieses Ergebnis zeigt, daß der spezielle Aufbau dieser Sensoren in der Tat zu einem weniger gerichteten Abstrahlverhalten führt, ohne den Energieausstoß nennenswert zu verringern. Damit sind diese Sensoren für den Zweck des seismischen Erkundens von Sandkastenmodellen optimiert. Dennoch ist die abgestrahlte Energie relativ gering, um stark dämpfende Medien wie Sand zu durchdringen. Die Eindringtiefe in den Experimenten mit Glasperlen und Sand liegt bei nur 5 cm.

Um granulare Materialien unterschiedlicher Impedanzen für den Modellbau zu bestimmen, wurden die akustischen Eigenschaften granularer Medien anhand von existierenden Publikationen zu dem Thema rezensiert, und eigene Durchschallungsmessungen an Quartzsand, Granatsand und Glasperlen durchgeführt. Die Messungen an Glasperlen verschiedener Korngrößen ergeben eine Kompressionswellengeschwindigkeit von 1,8 km/s, während die Ergebnisse an Quarz- und Granatsand so große Schwankungen aufweisen, daß die Geschwindigkeit nicht zuverlässig bestimmt werden kann. Der Grund für diese Schwankungen liegt darin, daß die Kompressionswellengeschwindigkeit in granularen Medien unter atmosphärischem Druck hauptsächlich von der Art der Korn-zu-Korn Kontakte abhängt, und nicht von der Mineralogie. Deswegen ist sie sehr abhängig von kleinen Variationen in der Kornpackung, die beim Sieben

der Proben und Modelle nur schwierig zu kontrollieren sind. Dieses Prinzip nutzend, kann man auf Impedanzkontraste der Schichten verzichten und lokal nur die Fläche zwischen zwei Schichten andersartig präparieren als die Schichten selbst, um eine Reflexion hervorzurufen. Auf diese Weise werden die stärksten Reflexionen in Glasperlen-Modellen aufgezeichnet, wenn die Schichtgrenze mit Glasperlenpulver, das die Kornzwischenräume ausfüllt, bestreut und anschliessend geglättet wird. Die seismischen Sektionen von Glasperlenmodellen zeichnen sich gegenüber den Sandmodellen durch geringeres Rauschen und höhere Eindringtiefen aus, da die Glasperlen besser sortiert sind und somit eine homogenere Packung aufweisen als Sand. Die raue Oberfläche von Sandkörnern verhindert eine vollständige Sättigung, was sich in einer zusätzlichen Dämpfung des Signals auswirkt. Für die Analyse der Strukturen innerhalb von Sandkastenmodellen ist es nicht nur sinnvoll die Schichtgrenzen abzubilden, sondern auch die Scherzonen, die sich durch die Deformation herausbilden. Zu diesem Zweck wurde ein Faden quer durch ein Sandmodell gezogen, um eine der Scherzone ähnliche Dekompaktion der Körner hervorzurufen. Seismische Abbilder dieses Models vor und nach der Dekompaktion beweisen, daß die diese "Scherzone" im Labor seismisch abgebildet werden kann, wobei die Scherzone in Sandmodellen deutlicher sichtbar ist als in Glasmodellen.

Schließlich wird gezeigt, daß die Datenbearbeitung von seismischen Reflexionsdaten mit mehrfachen Quell-Empfänger-Abständen die Bildqualität und -auflösung deutlich verbessert. Dieses Ergebnis ist ein Fortschritt zu bisherigen Studien, in denen seismische Experimente in Millimeter-Skala hauptsächlich mit einem Sensor, der gleichzeitig Quelle und Empfänger ist, durchgeführt wurden, da die üblichen Sensoren mit ihrer starken Abstrahlbündelung die Vorteile weiter Abstände zwischen Quelle und Empfänger zunichte machen. Diese Annahme trifft auf die hier verwendeten Sensoren we-

gen ihres speziellen Aufbaus und einer für sie optimierten Quell-Empfänger-Geometrie nicht zu. Gleichwohl sollte das Signal und die Eindringtiefe der Sensoren verbessert werden, um komplexere Modelle als die hier gezeigten, zufrieden stellend seismisch abbilden zu können. Bis eine solche Quelle zur Verfügung steht, sollten die seismischen Experimente eher an gering mächtigen Sandkastenmodellen angewandt werden. Gleichwohl liefern die seismischen Experimente, besonders im Zusammenspiel mit 2-D *PIV*-Analysen, wertvolle, wenn auch oberflächennahe, Strukturinformationen in 3-D.

1 Introduction

To achieve qualitative and quantitative insight into geological processes occurring in compressional and extensional settings, researchers use surface observations in nature, and apply numerical and analog modeling techniques. In contrast to observations in nature, modeling techniques allow to observe the development of structures through time. However, any modeling technique is bound by assumptions and simplifications. With evolving computer power, numerical modeling techniques offer cheap and fast results in three dimensions. Nevertheless, analog 'sandbox' modeling is frequently applied on big and more complex models.

The fundamental assumption, that allows a direct comparison of analog models and nature, is that rock deformation in sediments and rocks in the upper 1-15 km of the crust is governed by pressure-dependent, time-independent Coulomb behavior including strain hardening and softening, before and after failure, respectively (Byerlee, 1978; Davis et al., 1983; Schellart, 2000; Lohrmann et al., 2003). Due to the scale-invariance of the Mohr-Coulomb-failure criterion, suitable analog materials can be scaled to nature with respect to their length units, density and frictional properties (Hubbert, 1937; Schellart, 2000) in order to have a brittle fracture and frictional sliding behavior similar to that of crustal rocks. Materials such as dry sand, barium sulphate, and sand mortar, to name a few, have been measured for these properties and were confirmed to fit this description (Lohrmann et al., 2003).

For example, a typical analog experimental apparatus (Schreurs et al., 2006) to study the evolution of accretionary wedges in subduction zones, consists of a fixed horizontal plate (few meters × few decimeters) on which a conveyor belt, representing the subducting oceanic plate, is dragged underneath a rigid back wall, acting as the rigid part of the continental margin. The sand, representing deposited sediments, is sieved in layers onto the conveyer belt, and upon convergence, accumulates in regular imbricates in front of the back wall (Koyi, 1995, 1997; Storti et al., 2000; Lohrmann et al., 2003; Hampel et al., 2004; Hoth et al., 2007). For basin-building studies, either an elastic base is stretched or a solid base is moved sideways or downward (Gartrell et al., 2005; Lohr, 2007), so that the sand layers react to the increasing space with normal faulting.

In these experiments, the conveyor belt or base is glass-sided, so that the sand layers, and their reaction to shortening or extension, can be observed through the glass walls and from the surface as seen in Figure 1.1 (Hoffmann-Rothe et al., 2004). Hereby, cameras are deployed to take highly resolved photos of the deformation at regular time intervals, such that the evolution of structures can be evaluated in high spacial and temporal resolution by a computer software (e. g., PIV - particle image velocimetry, Adam et al., 2005). In this manner, a high-resolution 2-D profile along the glass wall, and indirect 3-D information by surface observation can be achieved. True 3-D information can only be obtained by solidifying the model with transparent resin and cutting slices, after the deformation is finished. This method provides high resolution 2-D slices to analyze 3-D-structures. However, after solidification, further deformation of the model is impossible.

When investigating regimes with along-strike variations, e.g. oblique convergences, transfer zones, or varying crustal structures, 3-D information of the sand models is required throughout the deformation. Such non-invasive methods, that are able to resolve shear zones in 3-D, are provided by X-ray tomography and possibly by seismic imaging methods, because they are sensitive to the dilation associated with shearing (Lohrmann et al., 2003).
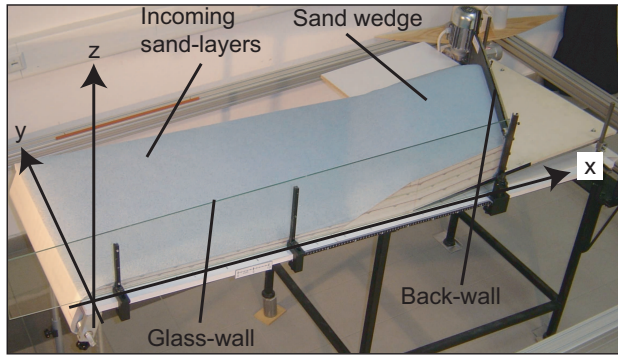
Figure 1.1: Photo of a 3-D sandbox model investigating a compressional regime (Hoffmann-Rothe et al., 2004). Convergence is in x-direction, while parameters vary along-strike in the y-direction. Using optical methods, analysis of the structure developing upon convergence is possible only by surface observations or in 2-D through the glass wall.

X-ray tomography has been used to image fault structures in cross sections of evolving models in Bern and at the IFP Rueil Malmaison (Colletta et al., 1991; Schreurs et al., 2006). Hence, the three-dimensional evolution of fault structures can be non-invasively observed from a series of neighboring X-ray cross-sections. This procedure provides a very high resolution (200 μm), albeit on a rather small cross-sectional area of 105×105 mm (Colletta et al., 1991). However, X-ray scanning is fairly elaborate and expensive: First of all, the experimenters should not be exposed to the X-ray radiation. Secondly, the X-ray equipment has either to be purchased, or the whole laboratory experiment has to be moved to a hospital, whose personnel naturally are fastidious regarding the hygiene, and are quite expensive as well.

Seismic imaging is a cheeper, less dangerous, high-resolution, and non-invasive method that is capable to obtain full 3-D information of a model under deformation. Based on the work of Sherlock (1999) and Sherlock and Evans (2001), my objective is to combine analog sandbox simulation techniques with seismic physical modeling of these models. The ultimate goal of this approach is (1) the imaging of seismic and seis-

mological events of actively deforming and static 3-D analog models, and (2) the assessment of the transferability of model data to field data in order to improve field data acquisition and interpretation according to the addressed geological problem.

To achieve this objective, a new small-scale seismic apparatus for laboratory use was designed and developed, composed of a water tank, a PC control unit including piezo-electric transducers (PET), and a positioning system (Krawczyk et al., 2007). Within the scope of this doctoral dissertation, the feasibility of this setup and method is shown on 2-D sandbox models that contain structures as we expect them to develop under extension or compression. However, time-lapse experiments to seismically image an evolution of structures have not been performed yet. When thus doing seismic physical modeling of granular models, two aspects besides the model scaling require particular attention:

(1) While the scaling of the model and material properties have been discussed above, the seismic frequencies need to be scaled so that they resolve the 2-3 mm wide shear structures, that are developing in the model. Therefore, the wavelength is required to be less than 6 mm, which at an approximate acoustic velocity of 1700 m/s, results in source frequencies higher than 300 kHz. The upper frequency limit is determined by the grain size. To prevent scattering from single grains, the wavelength should be at least $5\times$ the grain diameter (>200 μm), i.e. the frequency must be less than 850 kHz. The piezo-electric transducers, however, have a diameter of 12 mm and are thus at least twice as big as the wavelength. Therefore they generate a directed wave field rather than a spherical one. Hence in Chapter 2, the transducer properties are thoroughly investigated regarding their feasibility for seismic profiling in millimeter-scale. The results show that the PETs are suitable to be used for seismic reflection surveys on millimeter-scale for source frequencies of 350-550 kHz and for incidence angles $<35°$,

which corresponds to a 14-cm offset at water depths of 10 cm. This study is accepted for publication in the international scientific journal *Geophysics*.

(2) Because the elastic properties of the granular material determine the acoustic wave propagation and have a first-order effect on the seismic data quality, the acoustic wave velocity of various granular materials is studied in Chapter 3. The objective is to identify granular materials of sufficient acoustic velocity and density contrast to record reflections of layer interfaces. However, since the acoustic properties of sediments at low pressure depend mainly on the nature of the grain contacts (Sherlock, 1999; Agnolin and Roux, 2008), velocity and attenuation are highly sensitive to small changes in packing, and show great variability and little repeatability. A second purpose of this chapter is to be a guideline for anyone who may continue this work. This chapter is not intended for publication in an international journal.

Finally in Chapter 4, the results of seismic experiments across three different two-layer models are presented and discussed. Here, the results of Chapter 2 are used to choose a source-receiver geometry and water depth. The first model is, to some degree, a continuation of Chapter 3, in the sense that it helped to overcome the problem with the inability to measure the acoustic velocities. The results show that interfaces of layers of granular materials can be resolved depending on the interface preparation more than the material itself, because the procedure employed to assemble the grains has a first-order effect on the elastic moduli of a granular material (Agnolin and Roux, 2008). In the second model, a string is pulled through the model to simulate the decompaction of a shear zone. The decompaction created by the string caused a reflection that can be detected in the seismic data. In the third model, I perform a seismic reflection survey across a model that contains both the prepared interface and a simulated shear zone, and I ap-

ply 2-D-seismic reflection processing to improve the resolution. These experiments show, that especially for more complex models, the clarity of the images and the penetration depth of the signal need to be improved to study the evolution of geological structures in transient models with this method. However, it was also shown that seismic imaging of sandbox models, that are structurally evolving, is feasible. This chapter is intended for publication in a scientific journal.

Detailed information about previous studies, and background information to each of the specific topics are presented in the introductions of each chapter. Also, working procedures, experiment setups, processing steps, etc., are thoroughly reported in the following chapters.

A summarizing discussion of the results of these three chapters, and a proposal for future studies are presented in Chapter 5.

2 Performance of Piezoelectric Transducers in Terms of Amplitude and Waveform

Abstract

For seismic physical modeling, mostly piezoelectric transducers (PETs) are used as sources and receivers. Their properties have significant effects on the data, especially if they are to be processed as seismic data: 1. Strong resonance at one frequency causes a ringy signal and a narrow frequency band. 2. The pronounced directionality effectively limits the offsets at which energy arrives. 3. Because the dimension of the transducer with 12 mm is bigger than the wavelength (1.5-10 mm), the recorded waveform changes with offset. To reduce the pronounced directionality of the transducers at ultrasonic frequencies, we have designed PETs that have a smaller effective diameter than traditional ones. To test their applicability for laboratory seismic profiling, we test their frequency sensitivity, their directionality, and the change of waveform as a function of offset due to their size compared to the wavelengths. The experiments show that the PETs produce their best quality data at frequencies around 350-550 kHz and source-receiver offsets $\leq$ 14 cm. For these frequencies, the amplitudes decay to ringing noise level at incidence angles of $<35°$; for a 10 cm deep reflector that results in a 14 cm source-receiver offset. For these offsets and frequencies, the spacious dimension of the PETs

does not cause the waveform to change such that further processing is compromised. Also, we present an analytical solution to the changing waveform problem which predicts the temporal divergence of the signal as an additional resolution limit to the Fresnel effect; the loss of high frequencies is not only caused by attenuation, but is also due to the spacious dimension of the sensors.

2.1 Introduction

Since the 1920s, seismic physical modeling has been a successful tool for research in wave phenomena (i.e. the kinematics of wave propagation and the validation of wave theoretical predictions). In the first experiments, optical methods were used to record surface motion (Tsuboi, 1994) or wavefronts through transparent media (Rieber, 1936, 1937; Schmidt, 1939).

These experiments were performed on models such as rods (1-D), or elastic plates (2-D and 3-D) (e.g., Berryman et al., 1958; Redwood, 1960; Purnell, 1986; Zhang et al., 1996; Wandler et al., 2007, among many others). However, before 2001 virtually all models were made of solid materials, and thus were static. Dynamic models in which the material is deformed while monitoring require viscous or granular media such as sand, but severe attenuation and scattering of seismic waves in sand prevented the application of seismic imaging methods on sandbox models (Purnell, 1986). Sherlock (1999) and Sherlock and Evans (2001) were the first to try to overcome these problems and performed zero-offset seismic surveys at the mm-scale using piezoelectric transducers (PET) on sandbox models.

One reason to repeatedly try to perform seismic imaging on sandbox models is that these dynamic sandbox experiments have provided qualitative and quantitative insights into specific geological problems (e.g., Koyi, 1995, 1997; Storti et al., 2000; Lohrmann et al., 2003;

Gartrell et al., 2005; Hoth et al., 2007). So far, the internal structure of sandbox models can only be directly observed in 2-D profiles along glass walls confining the 2-D models or indirectly by surface observations (e.g. PIV - particle image velocimetry; Adam et al., 2005) or by X-ray tomography (Colletta et al., 1991). An improved seismic imaging system could provide non-invasive albeit less resolved 3-D information.

To achieve this objective, a new small-scale seismic apparatus for laboratory use was designed and developed, composed of a water tank, a PC control unit including PETs, and a positioning system (Krawczyk et al., 2007) with the ultimate goal to apply 3-D seismic and seismological imaging methods to sandbox models subject to deformation. These models are made of saturated granular materials so that deformation can take place. Resulting structures like shear bands are 2-3 mm wide and the layers have a thickness of a few millimeters to centimeters. Hence, the source frequencies need to be between 250 kHz and 1 MHz to generate waves with wavelengths between 6 to 1.5 mm, so that they are able to resolve these structures. Higher frequencies generate wavelengths that are approximately as big as the grain size of the material, so that each grain scatters arriving energy causing high attenuation.

When doing seismic physical modeling of solid or granular models, three aspects require particular attention: Scaling, transducer and material properties. In contrast to the continuing discussion about scaling factors within the geological physical modeling community, scaling for seismic physical models is trivial: Length and time scale factors are arbitrary, as long as the ratio of geological feature size to wavelength is the same in both the field and the model (Ebrom and McDonald, 1994). In nature as well as in the model, only the Nyquist criterion must be obeyed for temporal and spatial sampling. Regarding the equipment, most experimenters used electromechanical transducers, beginning

with the work of Kaufman and Roever (1994). Sometimes sparks (Kaufman and Roever, 1994; Hilterman, 1970) were used as seismic sources, but mostly PETs have served both as sources and receivers, such that the results are in the same form as field records (Riznichenko, 1994; O'Brien and Symes, 1994). However, the proper scaling of source and receiver dimension to wavelength is inevitably violated (in the field, individual sources and receivers are generally small compared to a wavelength), which imposes limitations on the use of PETs in seismic physical modeling:

- strong resonance at one frequency (i.e. restricted bandwidth),

- pronounced directionality, and

- source and receiver dimensions in the same order of magnitude as the wavelengths.

Furthermore, the material available for seismic physical modeling has several limiting effects: The parameter ranges for velocity and density are limited to those materials that are available or can be fabricated. Additionally, the attenuative properties and scattering effects of modeling materials cause substantial weakening of the received signals. Good source and receiver coupling to the model can be achieved by performing the experiments in a water tank.

The effects of the source and receiver dimension have been frequently neglected or dismissed in published physical modeling studies, despite the fact that they can have a first order effect on the data. Dellinger and Vernik (1994) numerically modeled whether experiments to measure velocities of layered rocks are more likely to measure the group velocity or the phase velocity of p- and s-waves. In their models they addressed the effect of a spatial source on wave propagation, and their Figure 5 shows nicely the waveform divergence with increasing offset or increasing source and receiver size at zero offset. However, they explained it solely as a result

of the anisotropic wave propagation in a layered medium with a slope and did not stress, that part of this divergence occurs even in a homogeneous medium.

Within the scope of this publication, we test the properties of our PETs with respect to their use in seismic reflection surveys of models and geometries as described above. We analyze the above mentioned properties analytically and experimentally and discuss the limitations and opportunities imposed by them.

2.2 Effects of piezoelectric transducers in ultrasonic experiments

The three limitations of piezoelectric transducers (PET), namely the strong resonance at one frequency, large dimensions and directionality, have the following effects on the seismic signal:

1. ringy signal at resonance/eigen frequency,

2. changing waveform with offset (temporal divergence),

3. high attenuation with offset (spatial divergence) in the plane parallel to the emitter surface.

2.2.1 Resonance frequency

Due to the piezoelectric effect, a piezocrystal can be excited to oscillate by applying AC. The amplitude of the oscillation is dependent on the source frequency and has its maximum at the resonance frequency of the PET (Krautkrämer and Krautkrämer, 1986). In order to reduce the oscillation subsequent to the excitation period, particularly at resonance frequency, the PETs are damped by a tungsten/resin filling. However, some ringing remains. This can be either reduced by a deconvolution filter, or the signal can be recorded at all angles and then used as a cross-correlation wavelet.

2.2.2 Changing waveform

The shape of a wavelet propagating from a source to a receiver changes with offset when their dimensions are bigger or of the same size as the emitted wavelength, because the length difference of the rays may be well over a wavelength λ, as illustrated by the two sample rays r_1 and r_2 in Figure 2.1. Hence, we have to consider each point of the source as an individual source point and assume that it emits energy at the same time (or at least within one or two sampling intervals) as all other source points. Due to different raypath lengths to any of the receiver points, the energy emitted at one instant arrives over a continuous time period which is increasing with offset. We call this effect "temporal divergence" following the concept of "spherical divergence" where energy propagating from a source point is distributed over a greater area. This effect is very similar to the Fresnel zone effect, only that the Fresnel zone is defined as the area to within half a wavelength around the reflection point that is contributing to the signal. In this case, it is the area of the source and the receiver that contribute; depending on the wavelength these areas can also have a radius of more than half a wavelength. This has to be taken into account additionally to the Fresnel zone when considering the spatial resolution.

The problem with the changing waveform is that stacking as an important step in the seismic imaging process assumes that the waveform stays constant, otherwise the superposition of the signals may not add constructively. Hence, we need to determine the critical offset below which stacking improves the signal quality for any applied source frequency.

The waveform as a function of offset can be predicted either numerically, e.g. by finite-element or finite-difference solutions (Savic and Ziolkowski, 1994), or analytically. The solutions depend highly on the geometry of the emitting surface. Therefore, we derive in the following a 3D-semi-analytical solution for the
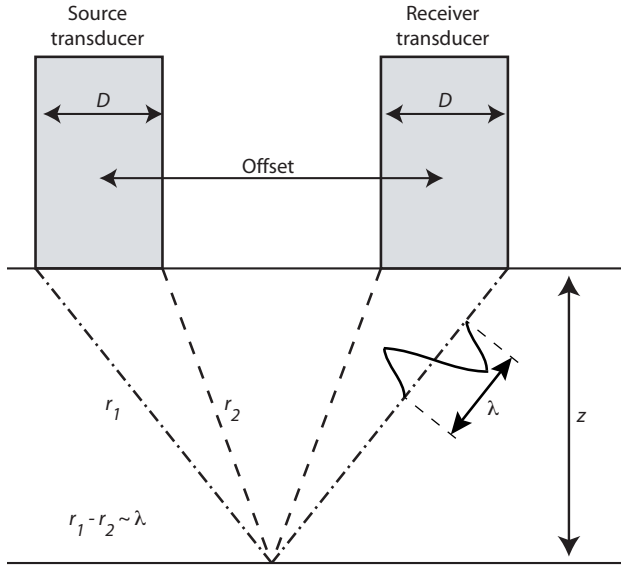
Figure 2.1: Sketch to illustrate that the waveform changes with offset, when high frequency energy propagates between two spatial transducers of diameter D. The two sample rays r_1 and r_2 show the maximum and the minimum raypath lengths possible for the given source-receiver geometry. The length difference can be greater than a wavelength λ, so that the shape of the recorded wavelet can differ significantly from the emitted one.
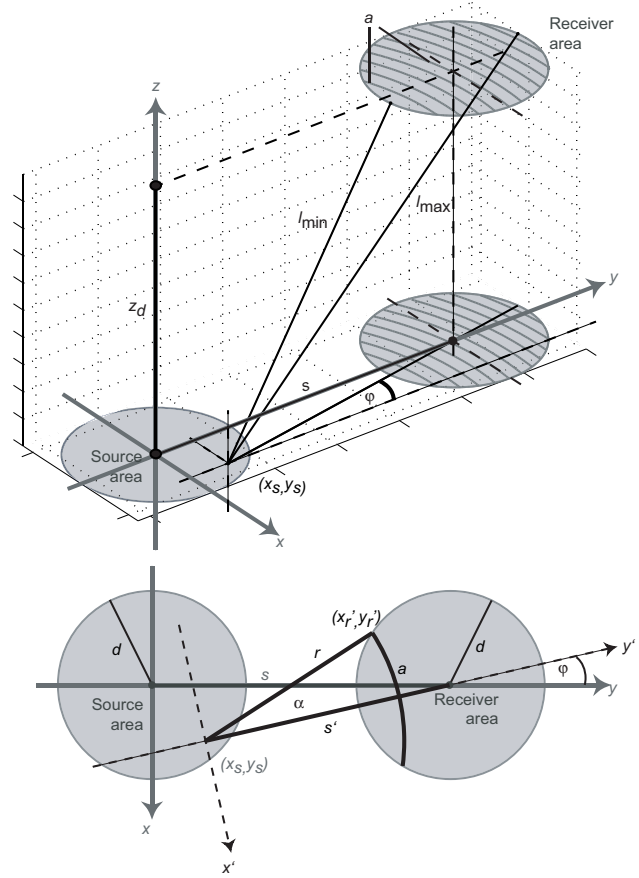

Figure 2.2: Geometrical sketch of all variables needed to calculate the arc length a. For detailed explanation, see text and equations 2.1 to 2.11.

energy-time-distribution as a function of offset and then compare it to experimental data in the results section.

3D-semi-analytical solution

The general idea for this solution is, that a certain amount of source area $A_s = \int_{x_s} \int_{y_s} dx_s dy_s$ contributes linearly to the energy E arriving at a certain time t at the receiver area $A_r = \int_{x_r} \int_{y_r} dx_r dy_r$ (Figure 2.2). Assuming an isotropic medium and perfect coupling, the arrival time t is equivalent to the ray path length l. Hence, we have to solve the following integral equation:

$$E(l) = \int_{x_s} \int_{y_s} \int_{x_r} \int_{y_r} \delta(x_s, y_s, x_r, y_r) dx_s dy_s dx_r dy_r,$$

(2.1)

with

$$\delta(x_s, y_s, x_r, y_r) = \begin{cases} \infty & \text{if } (x_r - x_s)^2 + \\ & (y_r - y_s)^2 + \\ & z_d^2 = l^2 \\ 0 & \text{else,} \end{cases}$$

(2.2)

where z_d is the vertical distance between the source and the receiver. Each point (x_s, y_s) of the source area A_s acts as a point source and the ray path length l to any point of the receiver (x_r, y_r) can be calculated geometrically. Furthermore, the set of (x_r, y_r) that are l apart from (x_s, y_s) describe an arc a on the area of the receiver. Hence, for each source point, we calculate the arc length a that contributes to the energy recorded at a certain time t, i.e. l. In this manner, instead of calcu-

lating an area, we calculate the arc lengths a for each l and integrate over A_s:

$$A(l) = \int_{A_s} a(x_s, y_s, l) dA_s. \qquad (2.3)$$

Then, for a given source point (x_s, y_s), an offset s to the receiver center and a depth z_d between source and receiver, the arc length a can thus be expressed as a function of l:

$$a_{x_s, y_s}(l) = 2r(l)\alpha, \qquad (2.4)$$
$$r(l)^2 = l^2 - z_d^2, \qquad (2.5)$$
$$\alpha(r) = \tan^{-1}\left(\frac{x_r'}{y_r'}\right), \qquad (2.6)$$
$$y_r' = \frac{1}{2s'}(r^2 - d^2 + s'^2), \qquad (2.7)$$
$$x_r' = r^2 - y_r'^2, \qquad (2.8)$$
$$s' = (s - y_s)\cos(\varphi), \qquad (2.9)$$
$$\varphi = \tan^{-1}\left(\frac{x_s}{s - y_s}\right), \qquad (2.10)$$

where d is the radius of both source and receiver plane, and r the projection of l onto the x-y-plane. The arc angle α is determined by the intersection (x_r', y_r') of the arc and the receiver outline in a new coordinate system (x', y'). This new coordinate system is offset by (x_s, y_s) and rotated by φ to the old one (x, y). s' is the distance to the center of the receiver plane from the origin of (x', y') and thus the offset of the receiver to the source point (x_s, y_s).

Since the integration of a over A_s is not trivial, we evaluate $a(l)$ at regularly spaced, discrete (x_s, y_s) positions:

$$A(l) = \sum_{y_s} \sum_{x_s(y_s)} a(x_s, y_s, l). \qquad (2.11)$$

As long as the spacing dx is smaller than the Nyquist theorem requests to prevent spatial aliasing, the discretized solution to $A(l)$ is proportional to the integral solution. Hence, the evaluated waveform and its amplitude are also proportional to a purely analytical solution.

Source and receiver radius d:	12 mm
Vertical displacement z_d:	100 mm
Spatial discretization dx:	0.075 mm
Sampling rate dt:	50 ns
Offsets s:	every 6 mm from 0 to 120 mm
Source frequencies:	175, 250, 350, 500, 750, 1000 kHZ

Table 2.1: List of parameters used to calculate the waveforms for different offsets and frequencies. The geometry corresponds to that used in the experiments, and the sampling rate is equal to that of the recording equipment in the laboratory.

To obtain the waveform theoretically recorded at offset s and depth z_d, $A(l)$ is convolved with the signal emitted by the point source on A_s, assuming that each point of A_s has the same signal. This assumption obviously does not hold true in reality, because the waveform is, during its course from a digital signal to its emission, subject to several interactions that change its shape inherently. To adjust the analytical waveform to resemble the real one, one needs an appropriate weighting function $\omega(x_s, y_s)$ to apply to the source area $a(x_s, y_s)$. However, we refrain from applying a weighting function or other corrections to the emission function and analyze the changing waveform rather qualitatively. Thus, the energy function is computed for offsets ranging from 0 to 120 mm and different frequencies using the parameters listed in Table 2.1.

The resulting waveforms are shown in Figure 2.3. As it can be clearly seen, the waveforms for smaller offsets (blue) are much more compact and resemble the original waveform, whereas the far offset waveforms (yellow to red) have smaller amplitudes (first column), and later peaks and continue over a longer period of time (center column). The frequency spectra (right column) show that the center frequency of the received signal decreases as the offset and the frequency increases.
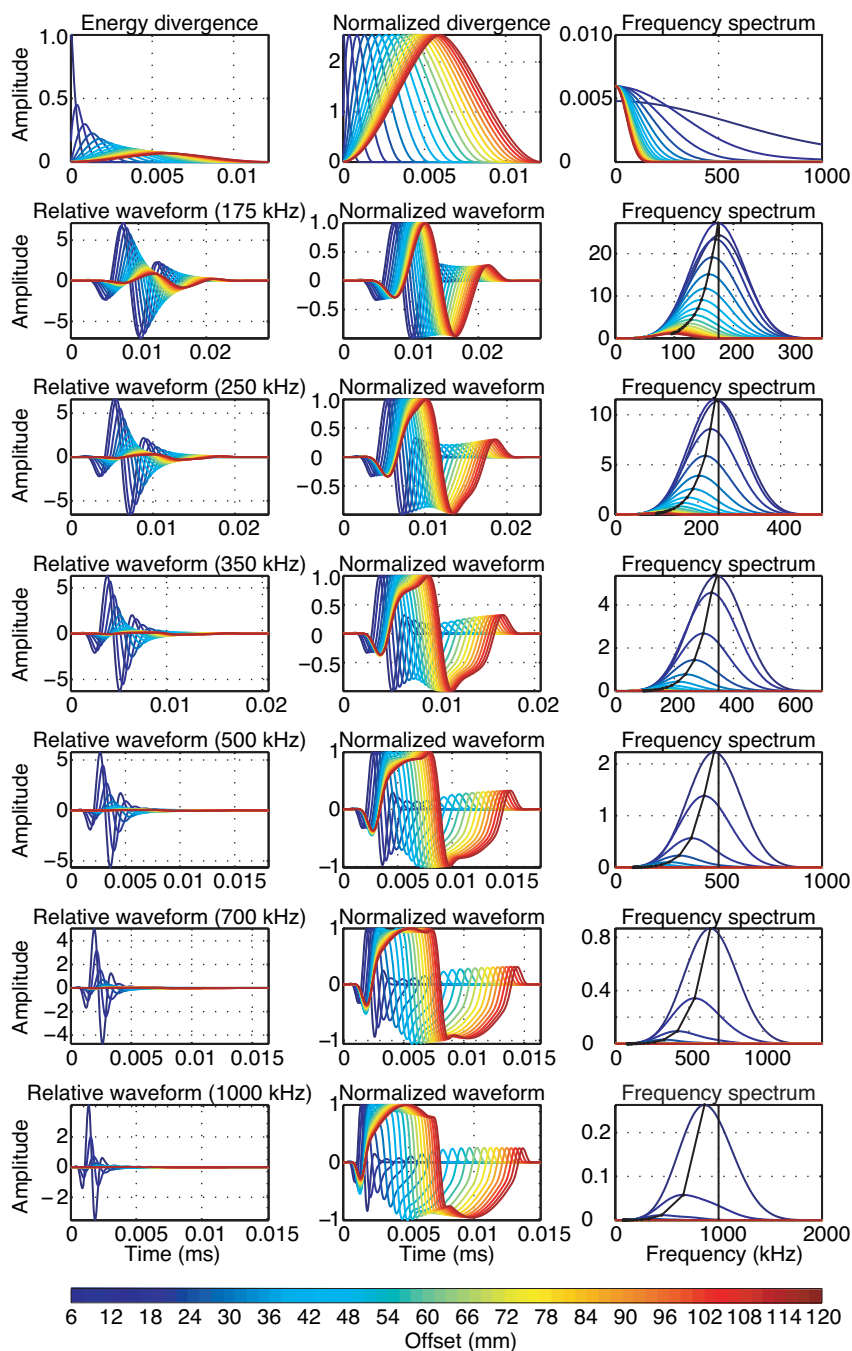
Figure 2.3: Resulting waveforms of the analytical solution for two spatial circular transducers according to the geometry described in Table 2.1 for offsets between 6 (blue) and 120 mm (red). First row: Temporal energy divergence (relative and normalized) and its frequency spectrum. Second row to last row: Relative and normalized waveforms (source signal convolved with energy divergence function) and the (relative) frequency spectrum for six different source signal frequencies. The vertical black line in the third column delineates the center frequency of the source, the curved line shows the actual frequency maxima being smaller than the source frequency. The waveforms of smaller offsets are much more compact whereas the far offset waveforms have smaller amplitudes and later peaks and continue over a longer period of time.
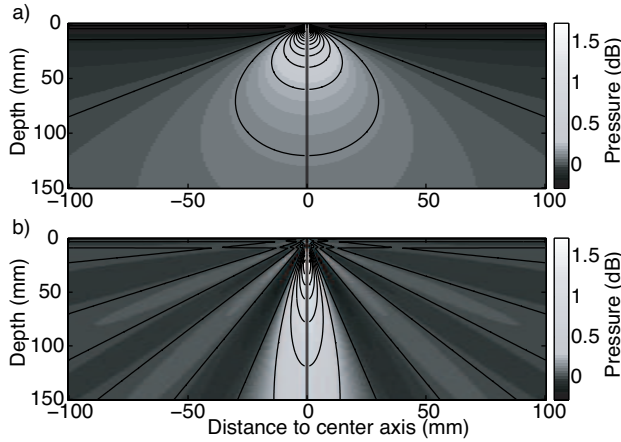
a)

b)

Figure 2.4: The calculated pressure field (see eq. 2.12) for a diameter of 12 mm as a function of depth and angle for 200 kHz (a) and 800 kHz (b). The higher the frequency the more focussed is the beam.

2.2.3 Directionality

For circular sources with a flat surface, the spatial divergence of the pressure field can be analytically described as a function of distance to the emitting plane and angle from the axis through the center of the plane by Krautkrämer and Krautkrämer (1986):

$$p(p_0, D, \lambda, z, \gamma) = 4p_0 \frac{J_1(X)}{X} sin\left(\frac{\pi D}{8\lambda z}\right),$$
(2.12)

with

$$X = \frac{\pi D}{\lambda} sin\gamma,$$
(2.13)

where p_0 is the initial pressure, i.e. amplitude, D the diameter of the emitter, λ the wavelength, z the distance to the emitting plane, γ the angle to the cylinder axis, and J_1 the Bessel function. Hence, the higher the applied frequencies and the shorter the wavelengths are, the more directed is the pressure field of a circular transducer as illustrated in Figure 2.4. This implies that less energy propagates at high angles, i.e. far offsets.

However, the emitting plane of the PETs used for this study is made of a piezocrystal of 5-mm
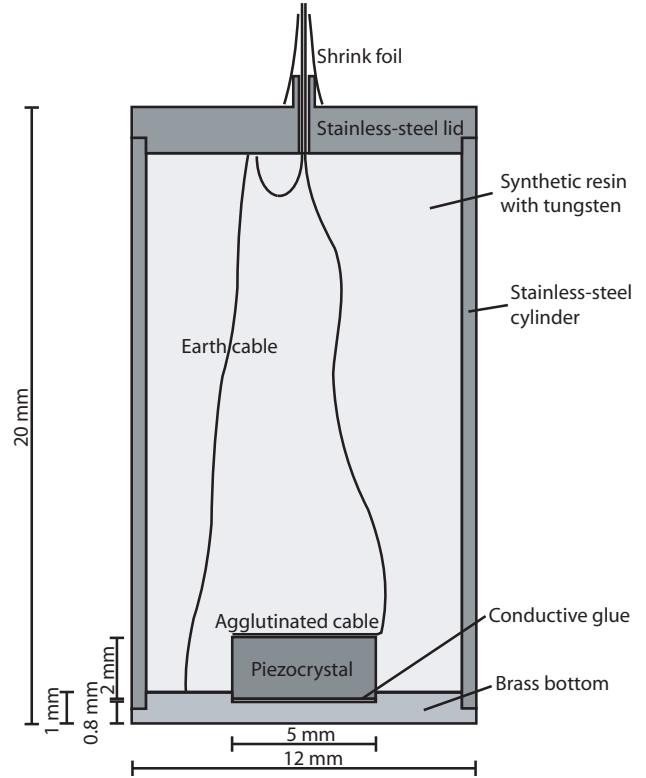

Figure 2.5: Sketch of the cross section of the piezoelectric transducers. The piezocrystal has a diameter of 5 mm and a height of 2 mm and is glued onto a brass plate of 12 mm diameter. For damping, the cylinder is filled with a mix of resin and tungsten. The transducer is in an unexpanded state and the emission area flat.

diameter glued onto a brass plate of 12-mm diameter (Figure 2.5). Hence, both the piezocrystal and the brass plate contribute to the emitted wavefield, such that it has a broader beam (Figure 2.6) at the expense of a smaller amplitude compared to usual PETs of this diameter. Since this is the first time these PETs are used, we determine the effective diameter experimentally by measuring the pressurefield at a fixed distance. We define the effective diameter (Figure 2.6) as the diameter which, when inserted into equation 2.12, gives the best match to the observed amplitudes. This effective diameter is frequency dependent.

2.3 Transducer design and experimental setup

For this study, we used 15 piezoelectric transducers (PET) which were manually build in Germany. The transducers have a 5-mm piezocrystal glued onto a brass plate of 12-mm diameter and 0.8-mm thickness underneath the piezocrystal according to Figure 2.5. The brass plate is very thin to keep the effect of internal reflections between the crystal and the plate reasonably small. The resin/tungsten filling is supposed to diminish the resonance ringing of the PET. In order to decrease the effective diameter of our PET, such that its directionality is less pronounced, the emitting plane differs from traditional ones: Commonly, the piezocrystal's diameter is that of the emitting plane (Figure 2.6, left panel) and equation 2.12 applies. In our case, the piezocrystal's diameter of 5 mm is smaller than the 12-mm diameter of the emitting plane. Hence, both the piezocrystal and the brass plate contribute to the emission such that the effective diameter may be anywhere between 5-12 mm, as illustrated in Figure 2.6. In fact, the bulging emitting surface creates a directivity pattern that is similar to that of a normal transducer of an even smaller diameter, which we define as the effective diameter of our transducers. In the results section, we determine the effective diameter experimentally.

A schematic illustration of the major components of the laboratory seismic system is shown in Figure 2.7 and the specifications are listed in Table 2.2. Briefly summarized, a well defined digital wavelet is converted to an analog electric current and sent to the piezocrystal of the source PET, which in turn expands and contracts according to (the time derivative of) the current. However, despite of the damping material, some ringing remains. Also, interaction between the piezocrystal and the brass plate affects the emitted source wavelet. The effectively emitted source wavelet is therefore different from the digitally inserted signal. After passing through
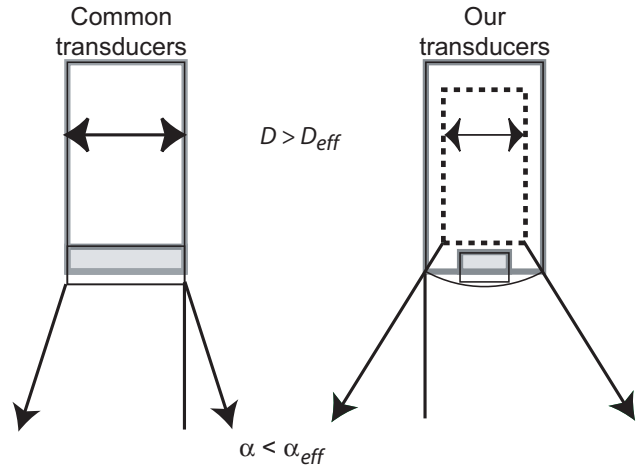

Figure 2.6: Sketch of a traditional piezoelectric transducer versus one of ours with a bulging emitter surface (not to scale). The geometry of an unexpanded piezocrystal is outlined in gray, whereas the expanded geometry is outlined with the thin black line. The traditional transducer has a diameter D and a beam angle α, whereas the bulging emitter surface causes the effective beam angle α_{eff} to be wider and hence the effective diameter D_{eff} to be smaller (outlined by the dotted black line).

the brass plate, the pulses propagate as pressure waves through room-temperature tap water and are received by a PET of the same build. The process of a digital signal to an analog pressure pulse is reversed for the receiver and the digital signal is recorded and stored in SEG-Y format.

As a source signal we used 2-4 periods of a sine function of the center frequency tapered with a cosine[4] for six different center frequencies. The shape of the source signal was the same for all applied frequencies. The frequencies ranged between 175 kHz and 1 MHz, the sampling rate was 0.05 μs and, because the signal showed remarkable consistency, we improved it by vertical stacking 256 times to overcome the weak power output of the transducers.

To determine the directionality as a function of incidence angle and the waveform as a function of offset, two different experiment setups were used as illustrated in Figure 2.8. The geometry for these setups is comparable to that in the sandbox experiments. For these experiments
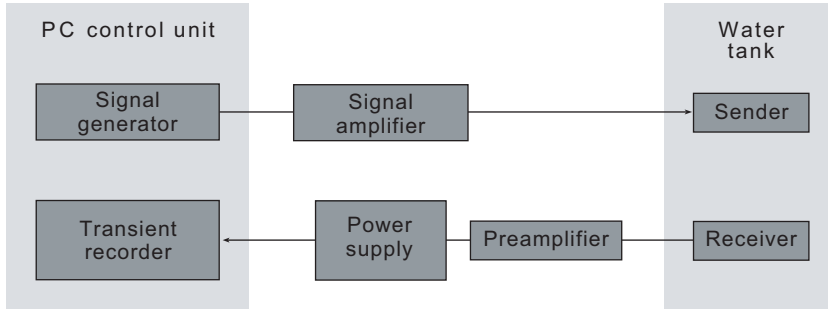
Figure 2.7: Schematic illustration of the functions performed for these experiments by the PC control unit and the positioning system modified after Krawczyk et al. (2007).

PC system with control unit:	Industry PC (type IPC-9401).
Signal generator:	PCI-board (type MI6030); Max. output 125 MHz (14 bit); Max. 8 Msamples; Max. output amplitude $\pm$ 3 V.
Signal amplifier:	AC voltage signal amplifier; Input -2 to +2 V; Input resistor 200 Ohm; Output -141 to +141 V; Output resistance 2 kOhm; Band width 20 Hz-500 kHz (-3 dB), 20 Hz-1000 kHz (-6 dB).
Preamplifier:	(Type VV30) 30 dB voltage amplification and impedance tuning; Frequency range 1 kHz-2 MHz; Max. output amplitude $\pm$ 3 V.
Transient recorder:	Three 4-channel PCI-boards (type MI4022); For each channel signal amplifier and AD-converter; Max. sampling 20 MHz (14 bit); Max. memory 2 Msamples/channel.

Table 2.2: Technical specifications of the components in the ultrasonic recording system (Krawczyk et al., 2007).

the transducers have been tested one by one and at water depths and distances to container walls such that reflections arrive much later in time than the direct waves that are to be analyzed.

The directionality was determined experimentally by opposing two PETs (one source, one receiver) with a constant distance of 10 cm, and rotating the source with a precision of at least $0.25°$; the rotation axis was positioned at the emitting end of the source perpendicular to the cylinder axis (Figure 2.8a). The measurements were repeated approximately every $2.15°$ from direct incidence up to $43.8°$ for six different source frequencies. The maximum amplitudes for each incidence angle and each PET were then automatically picked by a computer.

We define the effective diameter (Figure 2.6) as the diameter that gives the best match between the observed and the theoretical amplitudes from

equation 2.12. For this, we implemented a least-squares inversion routine to find D, p_0, and λ which best match these amplitudes:

$$\mathrm{erf}(p_0, D, \lambda) = \qquad (2.14)$$
$$\sum_{\gamma} [p_{obs}(\lambda, \gamma) - p(p_0, D, \lambda, z, \gamma)]^2,$$

with

$$\lambda = c_w / f_{src}, \qquad (2.15)$$

where the initial pressure p_0, the diameter D, and the wavelength λ are the PET and signal parameters, which the error function minimizes for. Additionally, p_0 is left to be a variable, because the transducers do not respond with equal amplitudes to the electric signal due to their variable sensitivity to frequencies. λ is calculated via the wave velocity in water c_w (1500 m/s) and the center frequency of the source signal f_{src}. However, because the recorded frequency maxima are smaller
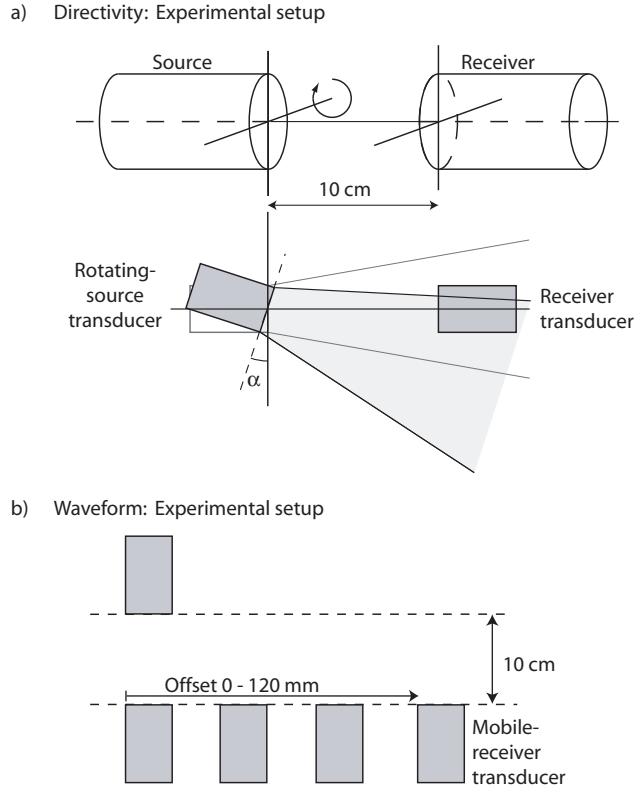
a) Directivity: Experimental setup

b) Waveform: Experimental setup

Figure 2.8: Experiment setup for measuring a) the directionality as a function of incidence angle α, and b) the waveform as a function of offset.

Figure 2.9: Frequency spectrum of piezoelectric transducers used here. The transducers are most sensitive at 425 ± 25 kHz with a half-power bandwidth of 250 to 675 ± 25 kHz.

offsets is subtracted accordingly. The receiving transducer was the same for all experiments. The zero-offset traces were used to determine the sensitivity of the PETs to different frequencies and the resonance frequency.

2.4 Experimental results

2.4.1 Resonance

The measured amplitudes for different source frequencies are displayed in Figure 2.9. The piezoelectric transducers (PET) are most sensitive at 400-450 kHz with a half-power bandwidth of 250 to 675 kHz.

2.4.2 Waveform

Before analyzing the waveforms, we looked at the length of the source signal, i.e. the number of periods in the source wavelet. We used the waveform experimental setup (Figure 2.8b) and procedure with a source signal of two, three, and four periods of a 350 kHz sine-function tapered with a cosine[4]. Theoretically, for a signal created as described above, the bandwidth is broader, as the

than the digital center frequencies, we also allow to minimize for λ within according boundaries.

The distance between source and receiver z and the angle to the cylinder axis γ are determined by the experiment setup. We consistently replace the pressure given in decibel by Krautkrämer and Krautkrämer (1986) by amplitudes in mV as they are recorded by our system. Hence, in equation 2.15 we minimize for the effective diameter D, the initial pressure p_0, and, within reasonable boundaries, for λ.

The waveform experimental setup (Figure 2.8b) provides a method for recording the signal as a function of offset by moving the receiving transducer parallel to the emitter surface of the source transducer. The distance z was 10 cm and the offset varied between 0 and 12 cm. To compare the actual waveforms at different offsets, the arrival time delay due to increasing
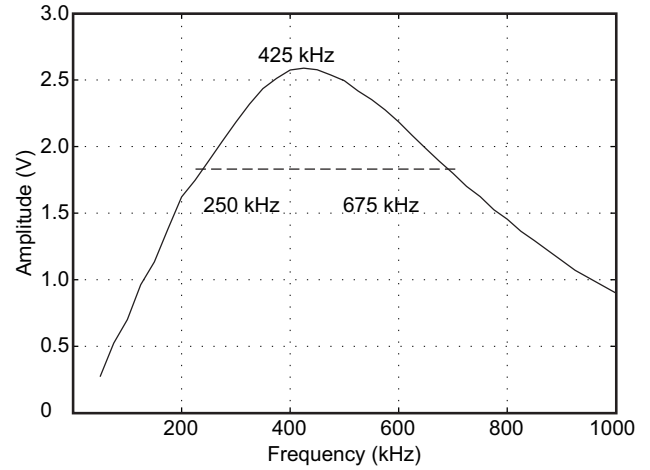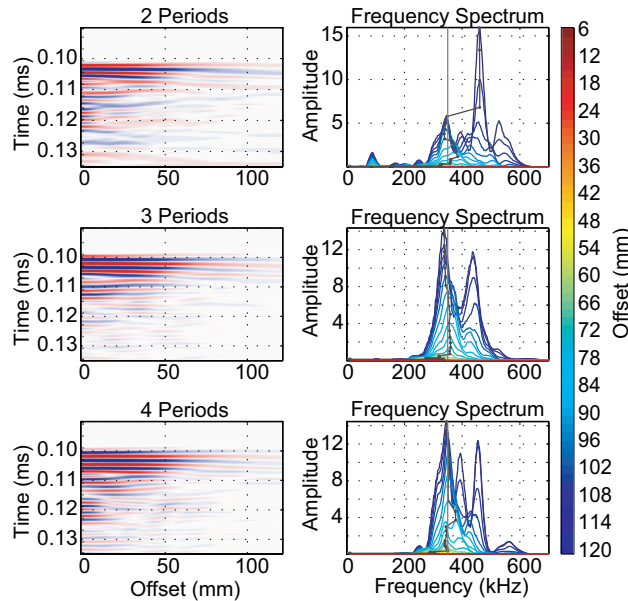
Figure 2.10: Recorded seismograms (350 kHz source frequency) and their frequency spectra for source signals of 2, 3, and 4 periods length as a function of offset (color coded). The maximum frequencies are delineated in gray.

signal shortens. However, Figure 2.10 shows that the bandwidth of the recorded signal is equally broad for three different source signal lengths, but the three-period source signal (2nd row panels) produces a better quality spectrum and the second positive phase is clearly defined. The four-period signal requires deconvolution for further use. Hence, for the following experiments, we show the results of the three-period signal experiments.

To analyze the recorded waveforms, we applied different source frequencies using the same experimental setup (Figure 2.8b). In Figure 2.11, we compare the waveform and frequency content for different source frequencies. Aside from the amplitude decay (i.e. directionality), which we deal with in the next section, it is noteable that the first peak arrives later in time for higher offsets, and later phases interfere destructively with varying offsets as is predicted by the analytical solution.

The recorded waveforms look very different to the predicted ones, because the analytical solu-

tion does not account for the interactions between the piezocrystal, the damping material and the cylinder walls. The influence of the brass bottom and the glue on the wave propagation are thought to be negligible because their thickness is much smaller than the wavelength. In any case, these interactions can hardly be predicted and may even vary from transducer to transducer. However, the waveforms and amplitudes are comparable in their frequency dependence and therefore the conclusion remains the same:

For all frequencies < 700 kHz, the first peak and trough along all offset-traces are in-phase, whereas the end of the signal and the following ringing vary over the offsets. Since we stacked the signal 256 times, we can assume that the ringing is coherent for each offset and use that to our advantage: Since only the first two phases interfere constructively, NMO-stacking reduces the ringing. However, because of the narrow frequency band of the signal, a traditional velocity analysis produces non-unique results. One reflection causes several semblance maxima, one for each peak in the signal at every period of 2-3 μs, at different velocities. Hence, further processing could be greatly improved by knowing the velocities of the media within a model in advance. Since we know the media that we use to build the model, we can as well measure their velocity beforehand by transmission through a known thickness of the medium.

The strong dependency on the eigenfrequency is revealed by the frequency spectra (Figure 2.11, right column): Each spectrum contains several local frequency maxima; the highest one delineated by the dotted gray line differs from the center frequency of the source (gray line) by ± 100 kHz for source frequencies < 1000 kHz. The recorded spectra fit the source frequencies when they are between 350-500 kHz. The local maxima listed in Table 2.3 show that many maxima are multiples (± 10 kHz) of 110 kHz. Hence, 110 kHz is the main eigenfrequency. Only the maxima at 165 and 190 kHz cannot be associated
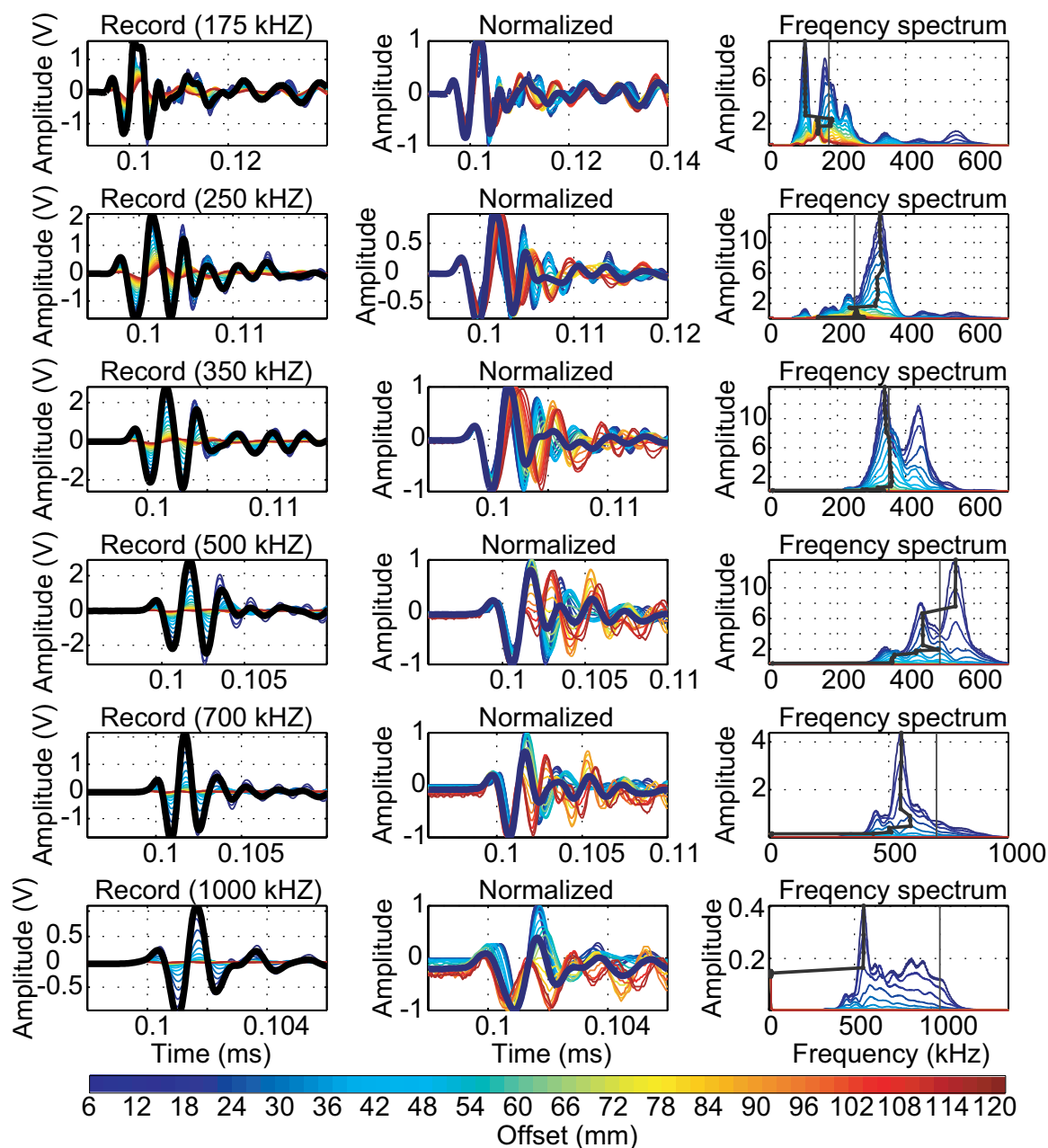
Figure 2.11: Change of recorded waveforms with offset (color code) and frequency (row 1-6) seen in the recorded traces (left), the normalized traces (center), and frequency spectra (right). The stack of all traces is shown in black. The vertical line delineates the source signal frequency, the dotted line the recorded maximum frequencies for all offsets. The first peak and trough are in-phase whereas the end of the signal and the following ringing vary over the offsets.

Source frequency (kHz)	Recorded frequency maxima (kHz)
175	**105**, **165**, 190, 225, 340, 440, 545
250	105, 165, 190, 230, **325**, 450, 545
350	**340**, **440**, 540
500	340, **445**, **550**
700	445, **550**
1000	**550**

Table 2.3: Recorded peak frequencies for different source frequencies. The major maxima are bold.

with the eigenfrequency and can be due to oscillations in a different plane.

Hence, for the preferred source frequencies of 250-675 kHz with respect to the sensitivity, the first two phases are not affected by the changing waveform. Destructive interference for later phases works to our advantage in further data processing. The spectra fit the source frequency best for source frequencies of 350 and 500 kHz, and both contain a major peak at 550 kHz. This reduces the suitable frequency range to 350-550 kHz, even though all frequencies between 100 to 1000 kHz can be applied to the transducers.

2.4.3 Directionality

The seismograms of a 5-mm PET for six different source frequencies, i.e. wavelengths, illustrate how the amplitudes decay with increasing incidence angles (Figure 2.12). This effect of directionality is more pronounced with higher frequencies. At 500 kHz source frequency, the signal cannot be distinguished from ringing noise at an incidence angle $< 35°$, whereas for 1000 kHz, the limiting angle is around $23°$. Note, that later phases of the waveform change at around $20°$ for frequencies > 350 kHz. This is due to the changing geometry with the rotation.

Continuing with this sample PET, we display the maximum amplitudes (Figure 2.13, solid lines) as a function of incidence angle for all tested frequencies (color coded) together with the best-fit curves (dashed lines). These best-fit amplitudes are the result of inserting the parameters of the best-fit solution (eq. 2.15) into the pressure
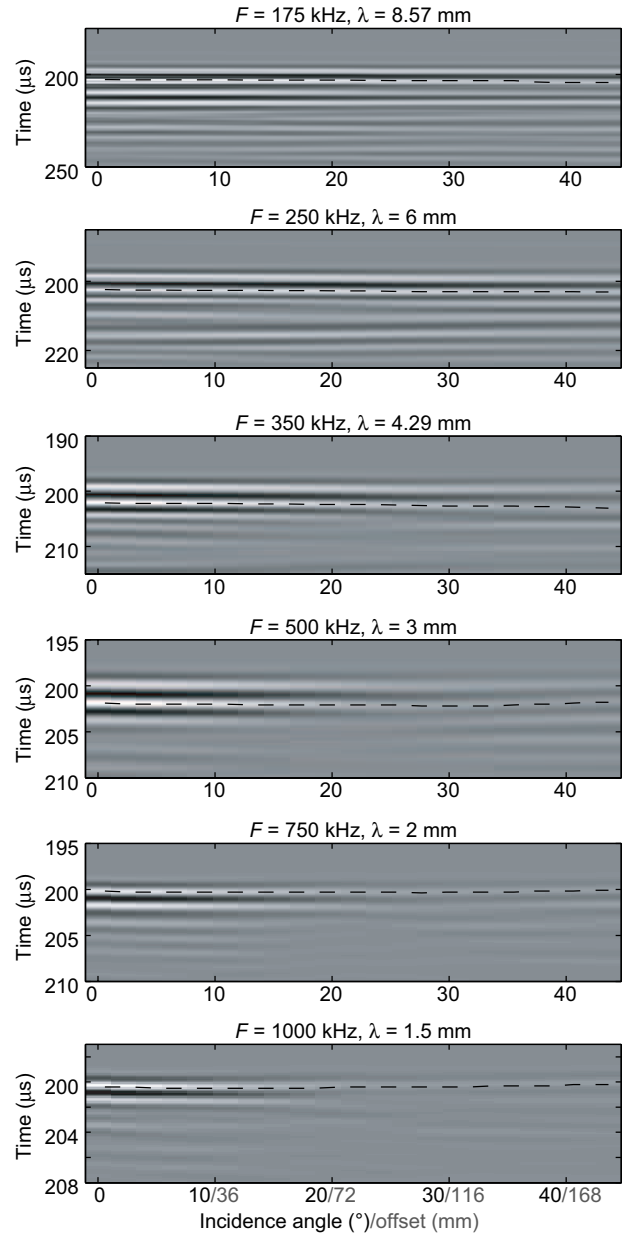

Figure 2.12: Recorded seismograms of a sample transducer as a function of incidence angle for different source frequencies (F), that, in water, are equivalent to the given wavelengths (λ). The gain has been maintained at a constant value. The incidence angle increases from left (direct) to right ($44°$). The respective offset indicated is calculated assuming a reflector depth of 10 cm. The dashed line indicates the picked maximum amplitude used for the minimization.
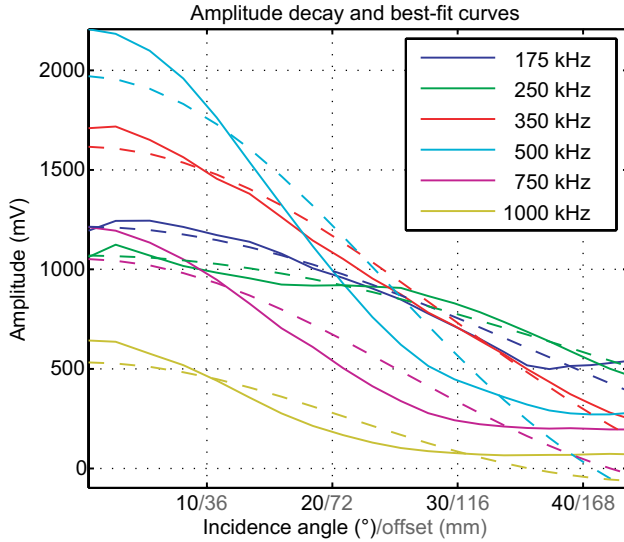
Figure 2.13: Amplitude decay of the sample transducer (solid) and the best-fit theoretical curves (dashed) for different source center frequencies (color coded). The incidence angle increases from left (direct) to right ($44°$). The respective offset indicated is calculated assuming a reflector depth of 10 cm.

field equation 2.12. The variability of the direct-incidence values illustrates the sensitivity of the transducers to frequency. The amplitude decay is most prominent for frequencies where the direct-incidence values are high.

The maximum amplitudes of all PETs are shown in Figure 2.14. Each panel represents one source frequency. The amplitudes of the 5-mm transducers (gray) vary $\pm$ 500 mV for 350-500 kHz; however, the amplitude decay follows the same course for all frequencies. The mean decay course is delineated in red and the blue lines represent the best-fit curves of the mean effective parameters. Hence we conclude, that the 5-mm transducers are comparable in their directionality and, for higher frequencies, in their sensitivity. For comparison, the amplitude decay of a tested 7-mm PET (black) has much higher amplitudes at direct incidence and is much more directed. Although the energy output of the 7-mm transducer is better than that of the 5-mm transducers, its strong directivity disinclines us to use it for multiple-offset surveys.
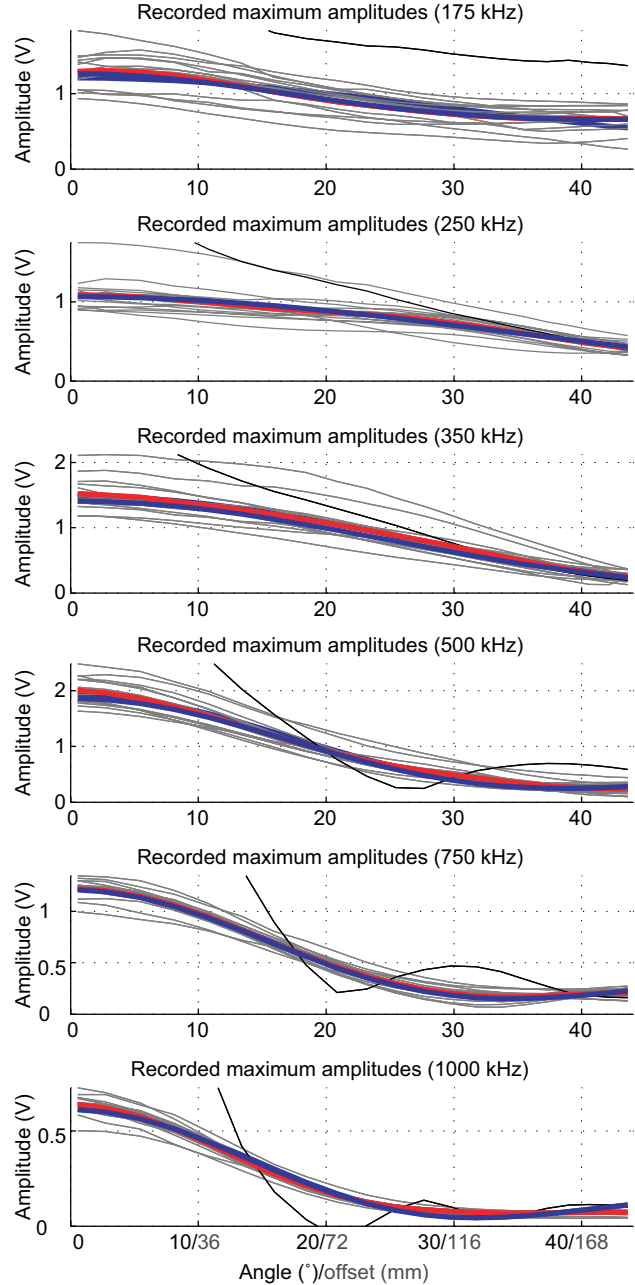

Figure 2.14: Comparison of the amplitude decay of the 5-mm piezoelectric transducers (PET) delineated in gray, their mean (red), their best-fit curve (blue) to the mean results from Figure 2.15, for six different source frequencies. Also shown is the amplitude of a 7-mm PET (black).

The best-fit parameters (D_{eff}, p_0, and λ) of all PETs (gray) and their mean (blue) are shown as a function of frequency in Figure 2.15. When these mean values are inserted into equation 2.12, the resulting amplitudes are nearly coincident with
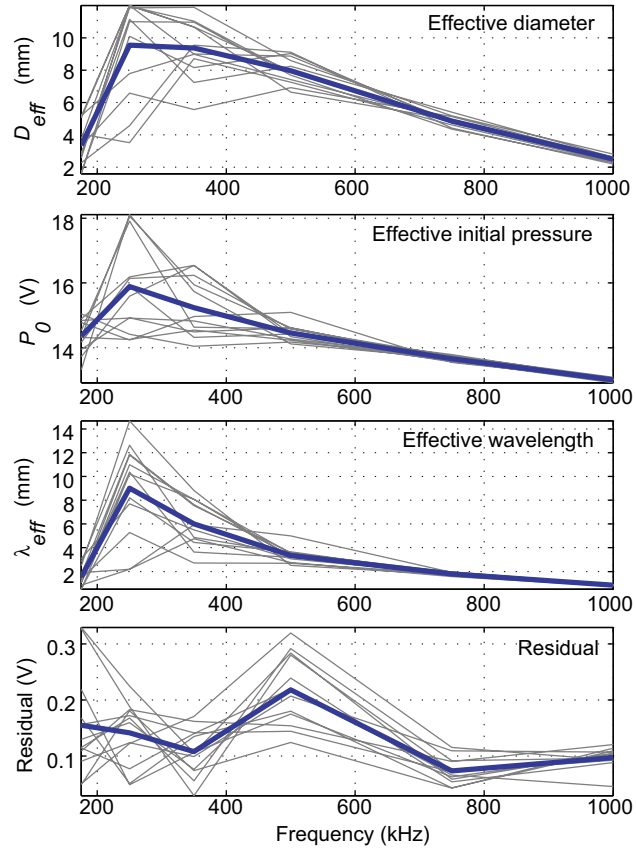
Figure 2.15: Effective parameters (diameter D_{eff}, wavelength λ, and initial pressure p_0) determined from measurements with different source frequencies. The results for each individual piezoelectric transducer (PET) are displayed in gray and their mean value in blue.

Source frequency (kHz)	D_{eff} (mm)
175	3.36 ± 1.30
250	9.54 ± 3.12
350	9.37 ± 1.81
500	7.96 ± 0.82
700	4.85 ± 0.30
1000	2.51 ± 0.17

Table 2.4: Mean and standard deviation of effective diameters D_{eff} for different source frequencies.

our design in fact reduces the effective diameter of the PETs.

2.5 Discussion

The experiments tested the piezoelectric transducers (PET) for their frequency sensitivity, and for the change of waveform and directivity as functions of offset and frequency. The results are summarized in Table 2.5.

All frequency requirements considered, the best quality results were achieved with a 350-550 kHz source frequency, because the PETs are most sensitive in that range and the recorded spectra best match the source frequency spectrum. The waveform changes more rapidly the higher the source frequencies are, however, the first two phases of the recorded wavelet are in phase for up to 12 cm in offset. Later phases interfere destructively to some degree, so that stacking actually focuses the signal. With the experimental setup used here, where the receiver is opposing the source, the effect of the offset on the waveform is not as big as it will be when both source and receivers are on the surface while surveying sandbox models. On the other hand, the velocities in sand and other granular material are around 1700 m/s (Sherlock and Evans, 2001), so that the wavelengths increase at the water-model interface. That, and the smaller path difference at deeper offsets counter-balance the waveform change at reflections within the model. Hence, the fit between the first two phases is sufficiently close, so that the changing waveform remains to be a minor problem when both source and receivers are at the surface. During further pro-

the mean amplitude decay in Figure 2.14. The inversion for the 175 kHz source signal was poorly conditioned and did not converge, therefore the 175 kHz results are not very meaningful and are not discussed in the following. The relatively high standard deviation of the best-fit parameters for the lower frequencies is also a result of the variation in the data. In the high frequency range, the transducers are more similar in their behavior and the inverted parameters are more consistent.

For all transducers, the determined effective diameter is decreasing with increasing frequency (see Table 2.4) and at high frequencies it in fact does go below the piezocrystal's diameter of 5 mm ($D_{eff} = 4.85$ mm at $f_{src} = 700$ kHz). Hence,

PET property	Effect	target	Solution / opportunity
Sensitivity	Narrow bandwidth	250-675 kHz	Apply 250-675 kHz
Resonance	Ringy signal	$n \times 110$ kHz	Damping, deconvolution
Spectrum characteristics	Does the signal match the source spectrum ?	Conditionally, yes.	Apply 350-550 kHz, and apply 3-period signal
Large dimension	Changing waveform (temporal divergence)	≤ 700 kHz,	- Positive interference for first peak and trough - Negative interference for later phases - A-priori knowledge of material velocity recommended
Directivity	Less energy at high offsets	$< 35°$ < 160 mm	- Increase water depth - Reduce D_{eff}

Table 2.5: List of the piezoelectric transducer (PET) properties, the resulting target frequencies, incidence angles, and offsets, and other solutions or alternatives.

cessing steps, the image quality could be greatly improved by knowing the velocities of the media within a model in advance. Since we know the media that we use to build the model, we can as well measure their velocity beforehand by sounding through a known thickness of the medium.

An alternative to this approach is to use the a-priori knowledge of the waveform to our advantage: Because the waveform is a function of offset and reflector depth, the energy distribution is unique for each offset, and we can use it to determine the reflector depth. Additionally, if the specific waveform for each offset is known, a shaping filter or cross-correlation wavelet can be designed for each offset, so that after filtering, the signals are sufficiently similar for a stack. Only we need to know the waveform for each offset and depth. The disadvantage of this solution is that the amplitude decays more than the waveform changes with increasing offset. Hence, it is more applicable to stay within the offset limits imposed by the directionality. The analytical solution to the changing waveform problem predicts the temporal divergence of the signal and shows that the loss of high frequencies is due to different path lengths and not to attenuation alone. The shape of the signal though is very different to the recorded shapes because the analytical function does not respect the interactions between the piezocrystal, the damping material, and the cylinder walls. Hence, the analytical solution in no way can replace experiments.

For all our experiments, we chose a water depth of 10 cm comparable to the water depth in experiments where sandbox models are seismically surveyed. At this water depth level, a 20-cm offset is equivalent to an incidence angle of 45°. The directivity results though suggest, that the incidence angle should not fall below 35° for a source frequency of 500 kHz, which corresponds to an offset of 14 cm. To increase applicable offsets, the water depth has to be increased. Furthermore, an increased water depth reduces the temporal divergence due to smaller length differences of raypaths.

In conclusion, we are restricted to 350-550 kHz and water depths ≥ 10 cm. Hence, the emitted wavelength is between 4.2-2.7 mm, allowing to resolve features of $\sim$2-1.5 mm vertical dimension. This frequency range is very suitable to image the structures in sandbox models. Higher frequencies generate wavelengths that approximately as big as the grain size of the material, so that each grain causes a reflection and obscures the image of larger structures, whereas smaller frequencies do not resolve the structures in sandbox models. The lateral resolution is dependent on the p-wave velocity of the medium, the depth of the reflection, and in this case of the effective diameter of the PETs, which has to be added as a constant to the normal fresnel zone calculation. In the worst case, i.e. the lowest source frequency of 350 kHz source signal and the deepest reflection at 15 cm through wet sand, it is going to be

about 46 mm. The models, therefore, should contain lateral variation longer than that, and shear bands should cut through at least a 46-mm width.

To do amplitude-versus-offset (AVO) analyses on field data, very often a plane-wave solution (Zoeppritz) is used, although the wave propagation is spherical. Alhussain et al. (2008) have experimentally confirmed the spherical wave effect on the AVO response by laboratory ultrasonic measurements using omni-directional p-wave transducers with a 220 kHz dominant frequency. The plane-wave solution (Zoeppritz) that is widely used for AVO analysis agrees well for moderate incidence angles up to $25°$ (their Figure 2), but is not valid at large angles. However, within the beam our PETs produce something between a plane wave and a spherical wave, and hence the AVO implementations are applicable to data collected with our PETs approximately up to incidence angles of $32°$.

Further improvement of the sources and receivers can only be achieved by using smaller transducers that have the same or higher energy output and the same frequency bandwidth. Unfortunately, those transducers cannot be fabricated yet. However, our design of a smaller piezocrystal being glued onto the brass plate did reduce the effective diameter, at high frequencies even to diameters less than that of the piezocrystal. Further improvement of this technique possibly will lead to transducers with zero effective diameter and high energy output.

The next step on the way towards seismic imaging of sandbox models, is to find suitable granular material. In the experiments reported here, the transmitting medium was water. The energy losses at the grain-to-grain contacts are very high, so that the penetration depth is not expected to be more than a few centimeters. Careful sieving and saturation with boiling or hot water can reduce attenuation caused by unwanted scattering or attenuation due to remaining air bubbles. In a two layer model, energy arriving at the first material interface should be reflected and refracted to approximately equal amounts, so that a sufficient amount of energy passes into the second medium to resolve structures within. To create such models, we can measure the velocity and density of available materials to find suitable impedance contrasts, and at the same time we can bypass a velocity analysis in the processing.

2.6   Conclusion

In this study, we tested the properties of specially designed piezoelectric transducers (PET) for their usefulness in seismic reflection surveys of sandbox models, covering three aspects, namely the frequency sensitivity, the directionality, and the changing waveform. We presented an analytical solution to the changing waveform and compared it to the recorded ones.

The special design of our PETs, where a smaller diameter (5 mm) piezocrystal is glued onto a bigger diameter (12 mm) brass plate, in fact reduced the directionality, so that the effective diameter is smaller than that of traditional PETs. The directivity experiments show, that the incidence angle should not fall below $35°$ for a source frequency of 350-550 kHz, which corresponds to an offset of 14 cm for a water depth of 10 cm. The changing waveform is a minor problem for those offsets and frequencies. However, an a-priori knowledge of the p-wave velocity of the materials is recommended to bypass the velocity analysis during further processing. The analytical solution to the changing waveform problem predicted the temporal divergence of the signal and showed that the loss of high frequencies is due to different path lengths and not to attenuation alone. However, it did not reproduce the recorded waveforms because it does not respect the internal dynamics of the PETs.

With respect to the PETs, we have shown that reflection processing on such a small scale is feasible for source frequencies of 350-550 kHz and for incidence angles $<35°$. This frequency range

allows to resolve structures of $\sim$2-1.5 mm dimension, which is sufficient to resolve the structures within sandbox models. However, the bandwidth of the generated signals is relatively small for seismic surveying. In order to broaden the spectrum, we recommend to pulse in several of these narrow frequency bands and stack those as a pre-processing step.

3 Sound Velocity and Impedance of Granular Materials

3.1 Introduction

Analog sandbox simulation techniques have been applied to study geological processes to provide qualitative and quantitative insights into the evolution of mountain belts and basins. (e. g. Koyi, 1995, 1997; Storti et al., 2000; Lohrmann et al., 2003; Gartrell et al., 2005; Hoth et al., 2007). However, the continuous evolution of internal structures of sandbox models can only be directly observed in 2-D profiles through glass walls confining the 2-D models or indirectly by surface observations (e. g. PIV - particle image velocimetry, Adam et al., 2005). 3-D images can only be obtained by either very expensive and very elaborate X-ray tomography (Colletta et al., 1991) on small models (few centimeters), or, after the deformation is finished, by solidifying the model with transparent resin and cutting slices. This method provides high resolution 2-D slices to analyze the 3-D-structures, that have developed until the time of solidification. However, after solidification, further deformation of the model is impossible. A non-invasive method that obtains full 3-D information of the subsurface is provided by using seismic imaging, my focus in this study. The objective is to combine the analog sandbox simulation techniques with seismic physical modeling of these models based on the work of Sherlock (1999) and Sherlock and Evans (2001), who were the first to perform zero-offset seismic surveys at the mm-scale on static sandbox models. When thus doing seismic physical modeling of granular models, three aspects require particular attention: Scaling, transducer properties, and material properties. While scal-

ing and the transducer properties have been thoroughly investigated by Buddensiek et al. (2009), the elastic properties of granular media under atmospheric pressure are investigated here. The goal is to find a combination of granular materials which can be used for model building such that seismic energy is reflected at interfaces. Internal scattering and attenuation due to the granular nature of the medium (Purnell, 1986) needs to be as low as possible, such that energy can penetrate deeper parts of the model.

In order to record reflections of structures within a model, materials of sufficient impedance contrast should be identified. Impedance is defined as the product of density and acoustic velocity of the material, which both can be measured independently. While the bulk density of a material is easily determined by measuring the weight of a known volume, the sound velocity of granular material under atmospheric pressures is more difficult to obtain. A high interest of the petroleum industry in the elastic properties of porous sedimentary rocks gave rise to many studies investigating acoustic wave velocities (hereafter called "velocity"), predominantly on consolidated and unconsolidated granular rocks, mostly under high pressure condition (e. g. Wyllie et al., 1958; Elliott and Wiley, 1975; Domenico, 1977; Han et al., 1986). Far fewer scientists studied elastic wave propagation in granular material under atmospheric pressure (e. g. Wyllie et al., 1956; Brandt, 1960; Talwani et al., 1973; Prasad and Meissner, 1992) and the combination of their results, when measuring the same material, is not consistent due to a number of factors, which I will discuss in detail in the following. For the same reason, also my results are very variable and occasionally erroneous. The primary purpose to find materials of suitable impedances could partly be fulfilled. A second purpose of this paper is to be a guideline for anyone who may continue this work.

In the following, I summarize the results of previous studies with respect to the boundary

conditions imposed by the intended application of the materials in seismic physical modeling: (1) The granular material needs to be completely fluid saturated so that the piezo-electric sensors that I use as sources and receivers are directly and well coupled to the propagating medium. (2) The experiments are conducted under room pressure and temperature. (3) The seismic source signal contains very high frequencies ($\sim$ 500 kHz) corresponding to wavelengths $\sim$ 5 times the grain diameter to be able to resolve small scale structures. Hence, severe attenuation and scattering can be expected, which has limited the application of seismic imaging methods on sandbox models to this day (Purnell, 1986; Sherlock, 1999). The materials, whose velocities I tried to measure experimentally by transmission through a known thickness, are quartz and garnet sand and glass beads of different grain sizes. As saturation fluid I use tap water at room conditions. In this unconsolidated/uncemented, un-pressurized and saturated condition, the sand is not in suspension, but is slightly compacted and has some rigidity.

The next section provides background information on existing theories of acoustic wave propagation in porous media, previous experiments investigating the properties and sample preparation procedures that affect the acoustic velocity in granular materials. Then, my experimental setup and its parameters will be described, before I present the results and discuss their meaning towards my goal to perform seismic imaging of sandbox models.

3.2 Acoustic velocity of saturated, granular media

3.2.1 Theoretical and numerical approaches and their comparison to experimental data

The key question in all theoretical approaches regarding the acoustic velocity of saturated porous media is whether there is water movement relative to the mineral frame. In models where water movement is disregarded, the effective density is the sum of the mass of water and solids in a unit volume; and Hook's elasticity equations can be used to derive wave velocities and elastic constants within the frequency range in which these parameters are effective, unless attenuation is involved in the study (Hamilton, 1972). Gassmann (1951) derived a first theoretical approach for low frequencies assuming elastic propagation through grains and ignoring viscoelastic properties of the fluid. Because of the low frequency assumption however, this approach is not applicable to ultrasonic laboratory measurements. Also, experimental results (e.g. Paterson, 1956; Wyllie et al., 1956, 1958) compared the variation with external pressure to computed values derived from Gassman's theoretical equations and reported a very poor fit for the low pressures used. Under the same elasticity assumption, the time-average equation (Wyllie et al., 1956) was able to fit their results much better, but only for pressures >30 MPa (which is equivalent to a 3-km water load) and with 100% water saturation (Blangy et al., 1993). Nevertheless, the fluid does move relative to the frame, and weakly cemented sands are not elastic, and are not at all sensitive to the actual modulus of the grains (Han, 1994; Sherlock, 1999).

Most viscoelastic models are based on Biot's theory (Biot, 1956a,b), in which the propagation of elastic waves in a porous elastic solid containing a compressible viscous fluid is derived. Biot's theory is valid for a broad frequency range

with an upper frequency limit where the wavelength approaches the pore size (Biot, 1956b). Nevertheless, his and descended theories (e.g. Pride et al., 2004) are only partly applicable to sandbox models, because unconsolidated sand cannot be approximated by a porous elastic solid because the rigidity is smaller. Models for solid rocks and for suspensions developed by Mehta (1983) include almost all multiple scattering processes but only for low frequencies. Again, not only the low frequency condition but also assuming suspension does not reflect high frequency wave propagation in settled, but unconsolidated sand. Basically, for water-saturated unconsolidated sediments, at least one of the fundamental assumptions (to specify some: solid porous rock, suspension, particles are spheres, Poiseuille / Darcy / squirt or no flow, the frequency range) of any existing theoretical model (Hamilton, 1972; Prasad and Meissner, 1992) is inapplicable to the conditions in sandbox experiments and/or the parameters needed to calculate the velocities and attenuation (wet frame moduli, tortuosity, shear modulus) are difficult to quantify (Chotiros, 1995; Sherlock, 1999).

In a numerical simulation, Agnolin and Roux (2008) found that the elastic moduli in dry or lubricated granular media depend much more on the coordination number than on density. The coordination number z is not related to density, but depends on the procedure (shakes, taps, vibration, lubrication, and undulatory shear) employed to assemble the sample, and is defined by:

$$z = \frac{2C}{N_{act}},\qquad(3.1)$$

where N_{act} is the number of force carrying grains and C is the number of contacts. High z-values correspond to higher average velocities than low z-values. A comparison to experimental data shows, that real samples behave like those with a low coordination number and high density. Unfortunately, the coordination number cannot yet be measured experimentally, because not even X-ray tomography is able to distinguish between in-

finitely close and contacting grains. Since it is not obtainable, it can only be addressed in experiments via grain sorting and packing as independent parameters. Poorly sorted sands have a lower ratio of contacts to force carrying contacts than well sorted sands, and hence coordination number and velocity decrease. Tighter packing and/or pressure, on the other hand, increases the coordination number and thus the velocity. Additionally, attenuation can be related to the coordination number, since it is largely due to energy lost due to friction between grains (Stoll, 1977). Hence, the higher the number of contacts the higher is the attenuation, however, if the number of force carrying grains increases, attenuation decreases because of less friction between these grains.

3.2.2 Parameters affecting the acoustic velocity (experimental studies)

In lack of reliable theoretical equations, several experimental studies qualitatively and quantitatively investigated the effects of various parameters on the sound velocity and attenuation in unconsolidated saturated media. While in consolidated rocks the p-wave velocity is mostly controlled by density, pressure, cementation, and temperature, the influence of these factors on the velocity of granular material is not yet fully understood. Several parameters are thought to control the acoustic velocity of (saturated) granular media, and have been investigated with ambiguous results: mineralogy, permeability, grain size, sorting, packing and shape, clay content, pressure, pore pressure, temperature, pore fluid, and the degree of saturation. In the following, I will summarize the effects of the parameters that are of interest for this study: Porosity is treated here as a dependent parameter of grain sorting and packing, because it cannot be changed without changing at least one of those. Since our experiments are performed under a constant air-conditioned temperature of 22°C, the effect of

temperature on the acoustic velocity is disregarded.

Mineralogy. Velocity measurements on quartz sand, basalt powder, volcanic ash (Talwani et al., 1973) and garnet sand (Sherlock, 1999) demonstrated that mineralogy plays only a minor role in the velocity of an unconsolidated sediment.

Permeability. To measure the velocity as a function of permeability, Wyllie et al. (1956) changed the permeability of samples of uniform glass spheres by a factor of 4.6×10^4 by varying the diameter of the spheres from 0.028 mm to 6 mm, and keeping porosity, mineralogy and packing constant. They conclude that the velocity of the granular materials is affected by neither the change in permeability nor by grain size. Another conclusion, that has not been made, is that the effect of permeability on the velocity is essentially canceled by the effect of grain size. Dispersion, however, is affected by permeability: A decrease in permeability decreases the frequency at which dispersion is greatest.

Grain size. The experimental results regarding the effect of grain size are most ambiguous: Using dry and saturated material, Talwani et al. (1973) and Prasad and Meissner (1992), respectively, found that the velocity is increasing with grain size, whereas Wyllie et al. (1956) recorded no difference (or a difference that is canceled by the effect of the change in permeability) in both dry and wet conditions. Sherlock (1999) shows that the energy velocity (calculated using the onset of the first arrival) increases with grain size, whereas the group velocity (calculated using the maximum amplitude travel time) remains constant (Figure 3.1). Regarding the signal quality, his results show that with increasing grain size (115 - 275 μm) the energy is distributed over a greater period of time with a shift of the maximum amplitudes towards later phases. Also, grains that are large relative to the wavelength, act as individual reflectors and contribute to the significant amount of noise within the data. Finer grain sizes ($\sim$ 200 μm) reduce the degree of
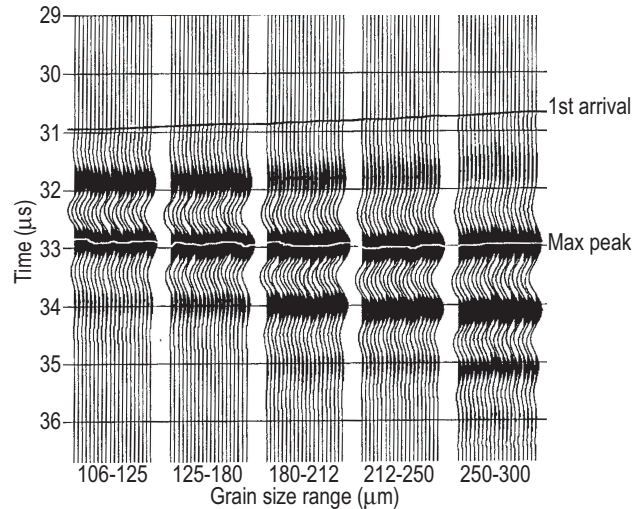

Figure 3.1: Experiment example modified after Sherlock (1999). Recorded signals from sounding through five well sorted sands of different grain sizes. The energy velocity (calculated using the onset of the first arrival) increases with grain size, whereas the group velocity (calculated using the maximum amplitude travel time) remains constant.

Rayleigh scattering, however, too fine grain sizes inhibit the complete saturation due to the reduced permeability and affect the dispersion behavior (Sherlock, 1999).

Grain sorting. Contradicting each other again, Wyllie et al. (1956)'s results show an increasing velocity with increasing porosity (that is better sorting), whereas Talwani et al. (1973) report that the effect of porosity is canceled by the effect of increasing the number of grains, even though both times porosity was essentially varied by change of sorting. Surprisingly, Talwani et al. (1973) found that velocity variations are almost completely reversible upon pressure cycling despite an irreversible change in porosity, i.e. sorting. Both results can be explained by the coordination number: Wyllie et al. (1956) prepared their samples to have the same packing while changing sorting, which increases the number of contacts C and therefore the coordination number. Due to the pressure cycling of Talwani et al. (1973), not only the sorting was changed but also the packing so that the coordination number remained constant. Also affected by sorting is the
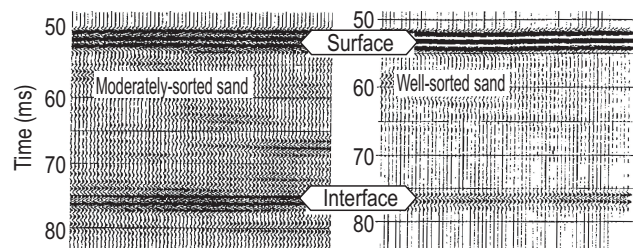
Figure 3.2: Experiment example modified after Sherlock (1999). Recorded signals from sounding through differently sorted sands showing that well-sorted sand generates less noise than moderately-sorted sand of the same average grain size.

signal quality, since poorly sorted sands contain more inhomogeneities in density and grain distribution than well sorted sands, similar to stratigraphic structures in fluvial systems. Unfortunately, these inhomogeneities cause unwanted reflections in a medium that is preferably homogeneous (Figure 3.2; Sherlock, 1999).

Packing. The packing of the grains affects the velocity significantly, since it directly affects the coordination number. Tight packing is equivalent to a high coordination number and therefore high velocity and low attenuation. Differences in packing can change the velocity up to 100 m/s (Sherlock, 1999; Agnolin and Roux, 2008). Different packing densities can be obtained by changing the method of sample preparation: pouring the grains into the container results in a porosity of 39%, sprinkling or sieving in 37.7%, and vibration in 37% (Sherlock, 1999). While vibration effectively reduces the porosity, it tends to smear the boundaries between an interface of two media. The sprinkling/sieving as well as a higher degree of sorting results in a more homogeneous distribution of grains (Sherlock, 1999).

Clay content. Sherlock (1999) investigated the effect that 1% to 50 % clay (kaolinite powder) have on the acoustic velocity of sand under atmospheric pressure. His results are consistent with those at pressures > 10 MPa of Marion et al. (1992), who found that the acoustic velocities in unconsolidated sand-clay (kaolinite) mixtures increase from 0 - 40 % clay content as a result of porosity reduction. The addition of clay increases the cohesion between sand grains, and hence increases the frame' s bulk and shear moduli and therefore also the acoustic velocity. As the clay content further increases, the velocity decreases because the pores are already filled up by the clays, so that the excess clays become part of the sand matrix. However on more practical terms, Sherlock (1999) was not able to obtain repeatable, consistent results, without confining pressure and mechanical mixing to force the saturation. Besides the high variability between measured velocities of the same proportions of sand-clay mix, the results show a time dependence of the velocity due to swelling of the clay minerals and a very poor data quality for clay fractions greater than 0.6 wt%.

Differential pressure, confining pressure, pore pressure. All our physical modeling experiments are performed under room conditions; however, the uniaxial tester in which I perform the velocity measurements can apply confining pressures up to 750 kPa. Therefore, I will review briefly on the pressure dependence of the velocity: A change in effective or differential pressure, which is equal to the confining pressure minus the pore pressure, causes a change in velocity. When the volume of water is greater than the pore volume of a sediment, as is the case with saturated sands, all of the pressure from the water above is carried by the pore fluid, that is, the differential pressure is hyrdostatic. Hence, the acoustic velocity in unconsolidated marine sediments is independent of the depth of overlying water (Brandt, 1960). Confining pressure on the granular material can only be imposed by externally applied forces (overlying sediment, a piston), with water allowed to leave the system. The velocity increases with confining pressure due to increasing inter-granular forces at the grain contacts, which attendantly increases the bulk and shear moduli of the assemblage of particles (Stoll, 1977). However, if the pore pressure is increasing when

applying confining pressure, the acoustic velocity decreases, unless the material contains a fraction of gas, i.e. the saturation is < 100%. In that case, an increase in pore pressure reduces the compressibility of the gas, which tends to raise the velocity (Mavko et al., 1998). As a result, the pressure dependence of v_p is smaller in completely saturated granular media than when the sample is dry or partly saturated. Also, a change in pore pressure changes the degree of saturation as gas goes in and out of solution. Domenico (1977) was able to fit his velocity observations for differential pressures between 2.8 to 35 MPa to the exponential equation $V = (AP_d)^n$, where V can be either P- or S-wave velocity, P_d is the differential pressure, and A and n are constants. He used $A = 4500$ and $n = 0.55$ for his unconsolidated brine-saturated sand. Nevertheless, at low pressures, velocities are remarkably scattered and do not fit to empirical (Domenico, 1977) or theoretical equations (Gassmann, 1951; Biot, 1956a,b; Wyllie et al., 1958).

Pore fluid. The pore fluids have first order effects on the pore space compressibility, which is inversely proportional to the seismic velocity, and affects the sensitivity of the velocity to changes in stress, pore pressure and saturation (Mavko and Mukerji, 1995). Increasing viscosity of the pore fluid shifts the dispersion to a lower frequency (Batzle et al., 1996). However, in water saturated sands dispersion is negligible or absent (Hamilton, 1972, and references within).

Degree of saturation. Experimental results of Elliott and Wiley (1975) and Domenico (1977) show that the compressional wave velocity in unconsolidated sand at pressures >10 MPa decreases over the range from dry sand to about 10% partial water saturation due to the overall density increase of the rock. In the saturation interval of 10% to 90%, the velocity is more or less constant, which implies that the effect of the increasing modulus due to increasing water saturation is canceled by effect of the density increase. As water saturation further increases from 90% to 100%, the velocity increases sharply due to the large increase of the bulk modulus. Since a fraction of gas has significant effects on the velocity and the attenuation, it is desirable to achieve nearly 100% saturation (100% saturation is impossible to achieve under Darcian flow conditions, Bacharach and Nur, 1998). The saturation can be increased by the use of hot water due to the lower surface tension, and by the use of highly permeable materials and/or fluids of low viscosity. Further improvement can be achieved by a saturation time of a few days and/or applying vibration, or a vacuum chamber. These methods can increase the velocity by 100 m/s (Sherlock, 1999). Well-sorted sands with high porosity and permeability approach the maximum velocity, i.e. the maximum saturation ($\sim 100\%$), after two or three days, whereas samples containing clays were still changing after a week of saturation (Sherlock, 1999). Applying vibration to the samples bears the disadvantage that it changes the packing and grain contacts, even though it effectively reduces the air bubbles. A vacuum chamber has been effective to extract all air within samples, however, such a facility was not available for this research.

Suspension. The transition from suspension to compacted material occurs when porosity attains the porosity of loose packing (Marion and Yin, 1988). For marine sediments the transition from suspension to compaction should occur in the interval over which compressional velocity ranges from 1.55 km/s to 1.7 km/s. In this transition zone attenuation is highest (Green and Esquivel-Sirvent, 1999). When depositing the sand under water, the sand is very close to suspension and even after a week of settling, the signal quality is not even close to experiments, where the model was saturated after it was built (Sherlock, 1999). When the model was first sieved and then saturated, the grains are not in suspension, but in loose contact. Hence, attenuation in granular material, that is near suspension and only nearly 100% saturated, is extremely high.

In summary, the velocity and attenuation data become remarkably scattered as differential pressure approaches zero. The disparity not only occurs between the theoretical and experimental values but also among the experimental values for samples of the same material (Purnell, 1986; Nur, 1996; Sherlock, 1999), because the acoustic properties of sediments at low pressure depend mainly on the nature of the grain contacts. On the other hand, Weaver and Sachse (1995) derive by means of radiation and diffusion theory, that the ultrasonic energy in a bead will be transported out of the bead primarily by means of coupling to the water, and not by means of the elastic contacts with neighboring beads. However, even then the velocity and attenuation depend on the surface area of the grains. Hence, no matter which process actually drives the energy propagation in saturated granular media, velocity and attenuation are highly sensitive to small changes in grain size, sorting, compaction and saturation (Sherlock, 1999). These variations are very difficult to control when preparing the models and hence the experiments show little repeatability.

3.2.3 Systematic errors

Sample thickness. Because of the very high attenuation intrinsic to granular material at low pressures, the thickness of the sample has to be small to be able to record energy that has propagated through the sample. Unfortunately, the error in a first arrival pick results in an error in velocity that is inverse proportional to the sample thickness. Hence, the smaller the thickness is, the greater becomes the error in velocity. The maximum length over which energy can be detected with certainty depends on the energy that the source can emit, i.e. its diameter. Sherlock (1999) was able to use samples of no more than 5 cm in thickness while using a 12-mm diameter piezo-crystalline source, whereas Wyllie et al. (1956) used samples of 25.4-cm thickness, but unfortunately they do not mention the energy output or diameter of their piezo-crystalline sensors. An-
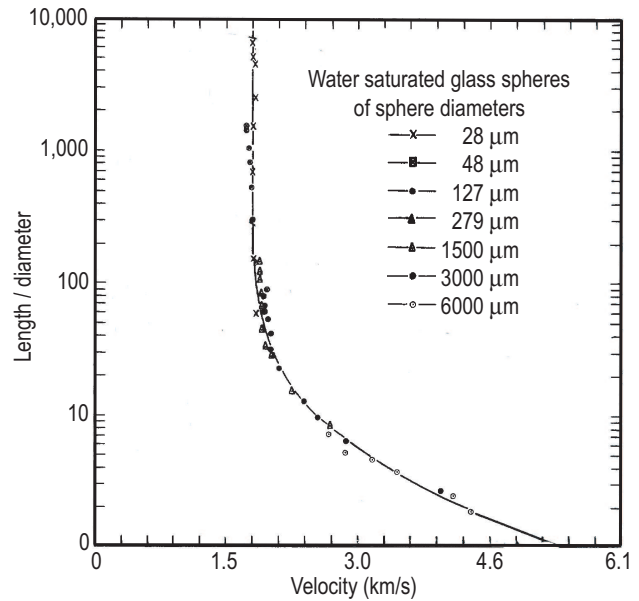

Figure 3.3: Experiment example modified after Wyllie et al. (1956): Velocity as a function of aggregate length/ particle diameter for water saturated glass spheres of various diameters.

other disadvantage of a small thickness are the edge effects of the flat surfaces of the specimen. The flat surfaces disturb the random arrangement of grains within the sample over a distance of numerous sphere diameters leading to an overestimation of velocity (Figure 3.3; Wyllie et al., 1956). For sample-thickness-to-sphere-diameter ratios > 100, or preferably even 1000, this effect becomes negligible (Wyllie et al., 1956).

Travel time picks. The method of picking the travel time has the most significant effect on the determined velocities due to the small sample thickness. While the time sampling allows a precision of $0.2\ \mu s$, the human error is much higher: It is very difficult to pick the onset of the first arrival, because the comparison to records taken under pressure shows that first peaks and troughs are easily missed due to attenuation, and one tends to pick the onset of a later, higher amplitude phase. Also, with the different attenuation of two materials, the first arrival picks are possibly picked at different points of the wavelet. This may also be the reason, why the results of previ-

Force range F:	0-10 kN
Pressure range P:	0-3.5 MPa
Volume change δV:	0-11.7
Piston velocity range v:	4-40 mm/s
Temporal resolution dt:	0.05 s
Voltage precision δU:	<0.0001
Pressure precision δP:	<0.1 kPa
Lid weight F_{lid}:	47.68641 N
Time sampling δt:	0.2 μs
Number of time samples:	8192
Frequency range:	50-1000 kHz
Amplitunde range:	100 -3000 mV

Table 3.1: Specifications of the uniaxial compression tester and the sound velocity measurement.

ous researchers seem to be so contradictory (Wyllie et al., 1958, versus Talwani et al., 1973). Quite possibly the method and tolerance levels for picking first arrivals can be hold accountable for the discrepancies. A meaningful estimation of error is the standard deviation of several measurements of the same material with the "same" preparation method. In the experiments of Sherlock (1999), the values for velocity varied by 50 m/s.

In the following chapter, the experimental setup to measure the velocity by sounding through a known thickness of material is described. Then, I present and discuss the results, and close with some conclusions.

3.3 Experimental setup and data evaluation

The device to measure the sound velocity of materials is integrated in the sample holder of the uni-axial compression tester (Figure 3.4, Table 3.1) for measuring the bulk modulus of granular material in GFZ analog laboratory.

The sample holder is a cylindrical aluminum pot of 260 mm inner diameter and an inner height of 85 mm. The bottom piece is attached to the cylinder walls, while the lid with a weight of 47.69 N (= 3.6 kPa) and diameter of 258 mm is placed on top of the sample and acts as the compressing piston. Since the lid diameter is 258 mm, water can slowly escape along the sides, so
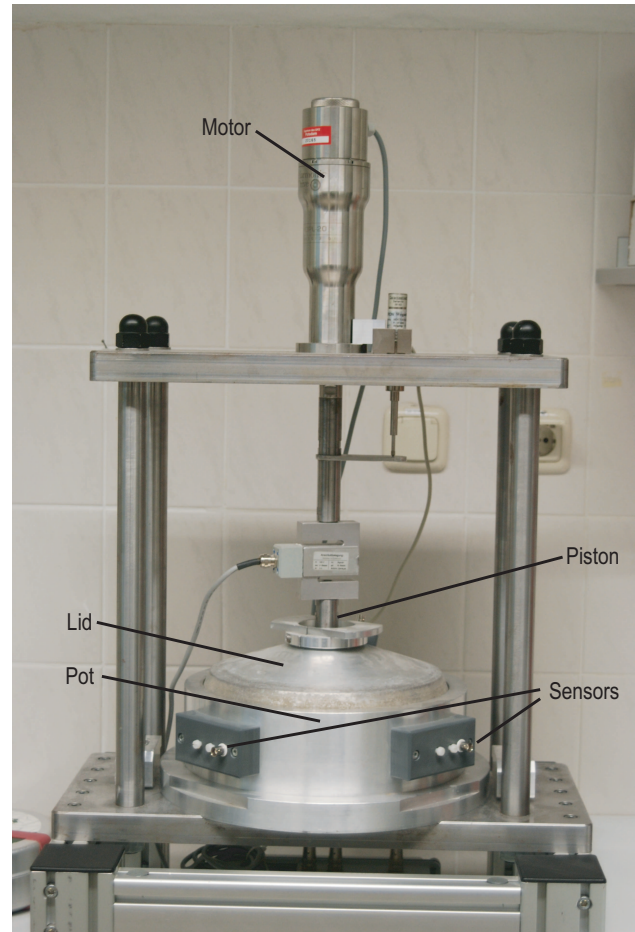

Figure 3.4: Photo of the uniaxial tester developed in the geodynamics laboratory of the GFZ Potsdam.

that the pore pressure supposedly remains hydrostatic and the confining pressure equals the effective pressure.

Six sensors consisting of piezo-electric crystals of 17.5 mm diameter and 3 mm height and a damping filling of 8 mm are built into the sample holder (Figure 3.5). For horizontal sounding, four sensors are built into the walls of the cylinder, 90° apart, facing the cylinder center. The other two sensors are built into the bottom and the lid to test the vertical direction. To ensure good coupling between the sensors and the granular material, the sensors are in direct contact with the material during the measurement. To inhibit that most energy travels through the holder wall instead of through the medium, the sensors are
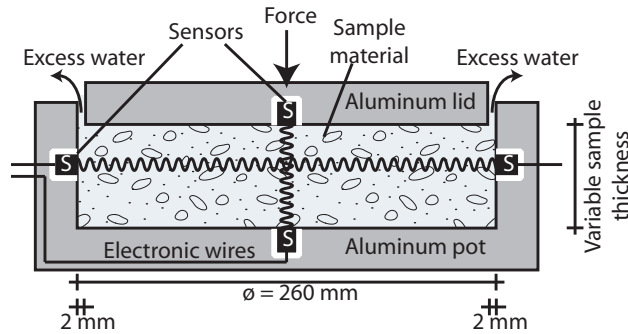
Figure 3.5: Cross-section of the sample holder of the uni-axial tester (not to scale) showing one pair of horizontal and the two vertical sensors (black boxes). The sensors are surrounded by a rubber sleeve (white); the cables are wired through carved tunnels in the sample holder. The wiggle-lines between the sensors delineate two of the three directions (two horizontal, and one vertical measurement) in which the acoustic wave velocities can be measured.
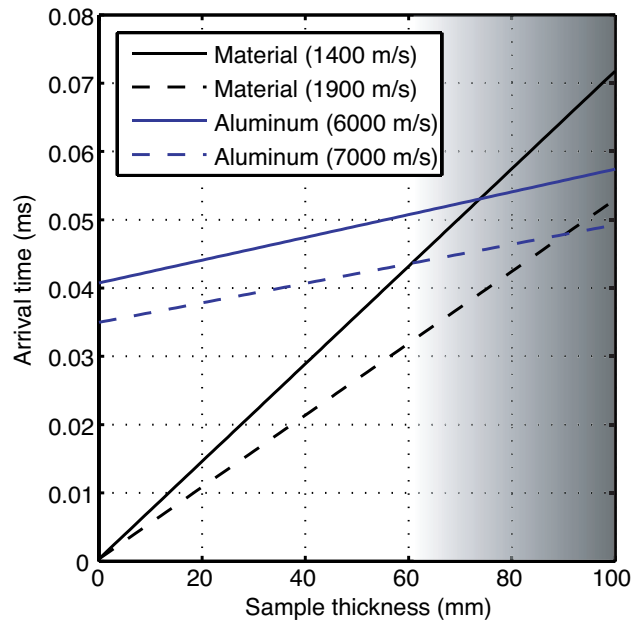

Figure 3.6: To show which thickness is sufficient to guarantee that waves traveling through the sample (black) arrive before the wave traveling through the sample holder (blue), the arrival times of both waves are shown as a function of sample thickness. The arrival times are calculated for a minimum and a maximum velocity of the granular material (1400 m/s and 1900 m/s) and the aluminum (6000 m/s and 7000 m/s) of the sample holer. Below a 60-mm sample thickness, the wave through the material arrives first. Above 10 cm, the wave through aluminum will arrive earlier. Between 6 and 10 cm, it depends on the actual velocities of the media.

de-coupled from the sample holder by a rubber sleeve. In case that the sensors are not fully de-coupled from the holder walls, a relatively wide diameter (260 mm) delays the wave through the holder, so that it arrives later than the direct wave through the sample if its thickness is < 60 mm (Figure 3.6). Also, the wide diameter prevents that reflections of container walls interfere with the direct wave.

After a sample material is filled into the cylinder, and the lid placed on top of it, an engine pushes the lid down onto the sample and compresses it. The maximal vertical compression is 10 mm, and the maximal force applied 10 kN ($= 753$ kPa). The specifications of the axial tester are given in Table 3.1. A force sensor measures the force applied while a distance sensor measures the sample thickness while up- and unloading. At designated force values between 50 N ($= 3.6$ kPa) and 10 kN ($= 753$ kPa), the compression is paused and sound velocity measurements are taken in both the horizontal and vertical directions. A schematic illustrating the functions performed by the PC control unit and the axial tester is shown in Figure 3.7. For each measurement, one emitter and a corresponding receiver sensor are activated by a relay circuit. Each sen-

sor can act as emitter or receiver, and each combination of sensors is applicable. To test the velocity in three dimensions for anisotropy measurements, it is sensible to pick two opposing sensors as emitter-receiver couple.

The waveform of the source signal can be chosen to be a step function or a number of periods (1-10) of a frequency (50-1000 kHz) in a $cosine^4$ envelope. For all measurements presented here, I used a step function as source signal. The recorded signals were stacked 64 times and stored for further evaluation. The sampling rate is 5 MHz for a trace length of 8192 samples. The recorded signals were then analyzed and the onset of the pressure wave is hand-picked. The arrival time precision is dependent on the data
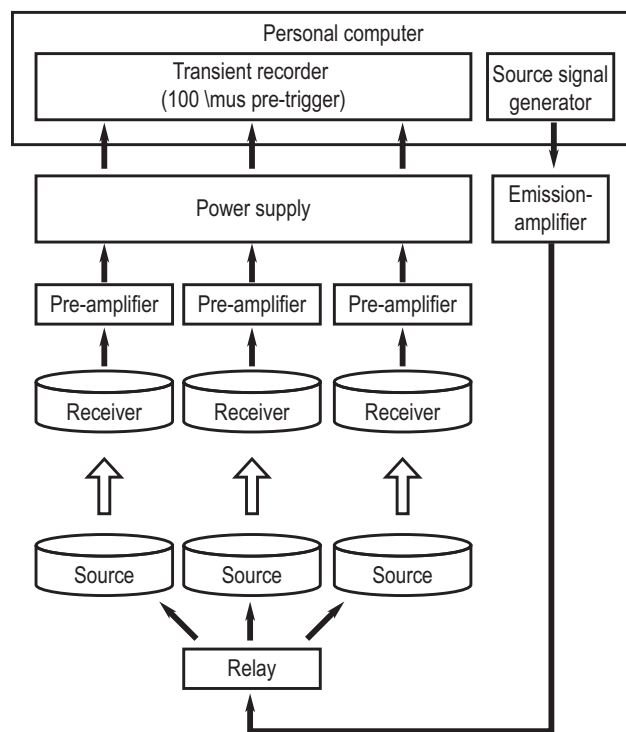
Figure 3.7: Schematic illustration of the functions performed by the PC control unit and the axial tester.

quality which varies with the material that is being analyzed as will be shown in the next section. To validate the reliability of the recorded signals, the pot is filled with tap water as a calibration medium. Although the reliability of results of the material measurements are arguable, the water measurements always produced clear signals referring to 1485 m/s.

The materials investigated here include quartz sand with grain sizes < 400 μm, glass beads with grain sizes ranging from 200-300 μm and 300-400 μm, and garnet sand with grain sizes between 125-250 μm. As saturation fluid, I decided to use hot tap water ($\sim$60°C) instead of oil, brine, glycerine, or other fluids, for a number of reasons: Firstly, water is easily available, cheap, and easily removed from the tank. Secondly, it has a lower viscosity than oil and brine, so that it saturates the sands quickly and more thoroughly, and dispersion can be disregarded. To improve the saturation of the sand, we use hot water since it

has a lower surface tension than cold water. All materials were tested in saturated condition, after the water had cooled down to room temperature, and the complete sensor surface was in direct contact with water. For the first experiments on quartz sand, I first sieved in the sand, then saturated it over a four-day period as Sherlock (1999) suggested. These experiments showed the extreme pressure dependence indicating remaining gas. Then, the first measurement of glass beads resulted in a constant arrival time and little variation in the signal at later times. Assuming a short circuit due to seepage, I checked the compartment containing the electric wires, which in fact were wet. Hence, the order of filling was reversed to decrease the saturation time and therefore the amount of seepage. Consecutive checks of the humidity showed that the wires stayed dry during the following experiments. However, drying the wires and the compartment, and reversing the preparation order, did not change the result that the arrival time stayed constant over pressure. The problem for modeling experiments, that sand deposited under water does not settle in time, is not an issue here, because the heavy piston lid compresses the sand such that it is not in suspension. However, this reversed order and the fact, that the prepared sample in the holder was subject to shaking when the sample holder was lifted up into the axial tester inevitably changed the grain settling and the grain-to-grain contact, so that they are not the same as in the seismic sandbox models and the applicability of the results is questionable. Nevertheless, these experiments show the pitfalls of this method irrespectively of the preparation method.

Because of the expected variability between velocity results of two samples of the same material, the experiments were repeated several times and also at different thickness levels of approximately 80, 34 and 20 mm height. For these lower thicknesses the sample holder needed to be placed upon stilts of 44 and 60 mm height, so that the engine pushing the piston was able to reach the sample. For these small thickness measure-

Thickness	20 mm	36 mm	80 mm
Quartz (400 μm)	50	90	200
Garnet (100-250 μm)	200-80	360-144	800-350
Glass (200-300 μm)	100-66	180-120	400-266
Glass (300-400 μm)	66-50	120-90	266-200

Table 3.2: Length/diameter ratio for materials and thicknesses used in this study.

ments, the length/diameter-ratio in some cases goes below the limit of 100, that was reported by Wyllie et al. (1956). Table 3.2 shows that all 20-mm thick samples contain grains below the limit and therefore the velocity will be overestimated, whereas the ratio for 36-mm thickness is around the limit, where the velocity will be correct within its precision; in our sandbox models, however, the most layers are critically thin with about 2-3 cm. This setup with different sample thicknesses theoretically also allows to determine the attenuation of a material.

3.4 Results

To show the variability in the signal from sample to sample, the recorded seismograms of all sounding experiments (one up- and unloading cycle) on samples of quartz sand (< 400 μm), garnet sand (100-250 μm), and glass beads (200-300 μm and 300-400 μm) are shown in Figures 3.8, 3.9, 3.10, and 3.11, respectively. The first two rows are the results of samples of ~ 80 mm height, the center two rows of ~ 34 mm height, and the last two rows of ~ 20 mm height. In these figures, I also distinguish whether the source signal was emitted by the top sensor or the bottom sensor. When two seismograms are framed by a black box, these measurements were taken on the same sample. Because of the difficulties encountered during the measurements, the collection of the presented experiments displays an uneven distribution of measurements for each material, sample thickness, and sensor configuration. The resulting velocities for each material (Figures 3.12, 3.13, 3.14, 3.15) are presented in

four panels, which show the compression and decompression due to the applied force, the arrival times over the applied force, the arrival times as a function sample thickness, and the velocity as a function of force. A pre-trigger and dead-time delay of 101.67 μs is already subtracted in the seismograms and in the first arrival picks. To compare the velocity measurements and the seismograms, the various experiments are color-coded by file name, which can also be found in the title of the seismograms.

In Figure 3.8, panels (a-c) display the results of $\sim$80 mm thick samples of quartz sand. (a) and (b) are measurements of the same sample, different only in the sensor configuration, while (c) was measured on a second sample of the same material. The curvature of the first arrivals (green line) in all three samples is very similar, only the amplitudes vary from a low amplitude of 200 mV in (a) to 800 mV in (b) and (c). Three reasons can have caused this difference in amplitude: Firstly, the bottom sensor is invariably better or equally well coupled to the medium than the top sensor, so that when the bottom sensor acts as the source, more energy is transmitted into the medium, and the amplitudes are higher or equal. Secondly, since (a) was the first measurement, it is possible that the coupling of the top sensor improved through time, because grains shifted so that any air bubble that may have been stuck underneath the lid could escape during the first pressure cycle. Thirdly, the attenuation may have been lower because the degree of saturation can have improved during the pressure cycle. However, a higher saturation should also show less pressure dependence than a partly saturated sample. In the same Figure 3.8, the results of the shallower samples displayed in (d-l) show more variability both in amplitude and first arrival curvature. All measurements with the source on the bottom have higher or equal amplitudes than their equivalent measurements with the source being the top sensor, but the same curvature, indicating a better coupling of the bottom sensor. The curvature however, reveals three types of pressure behav-
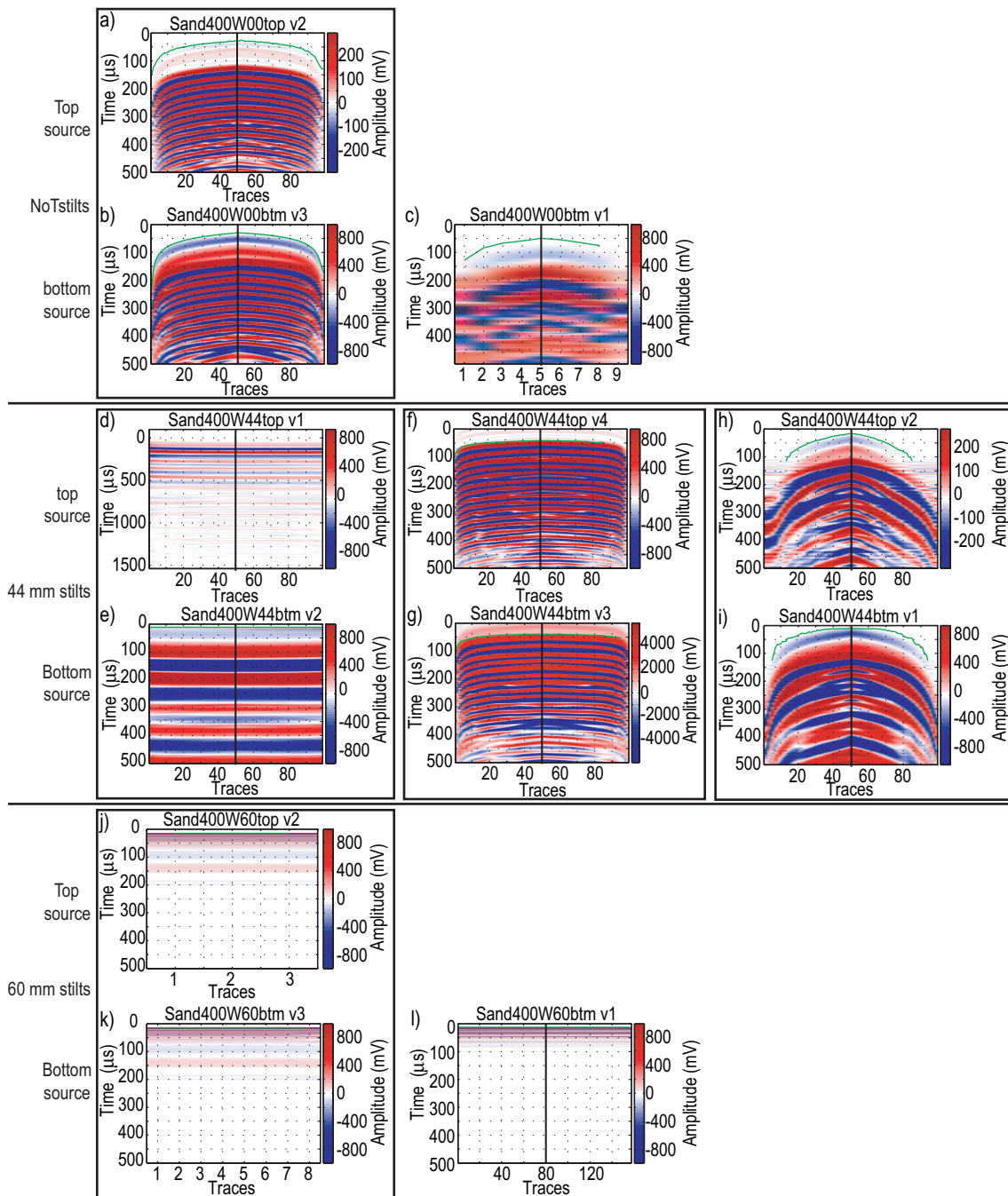
Figure 3.8: Recorded signals through quartz sand for sample thicknesses of ∼80 mm (a-c), ∼36 mm (d-i) and ∼20 mm (j-l). In each panel, the first break pick is outlined in green. The pressure is increasing from left to the center trace (delineated with the vertical black line) and decreasing from the center trace to the right. The experiments of (j-k) were interrupted while uploading.
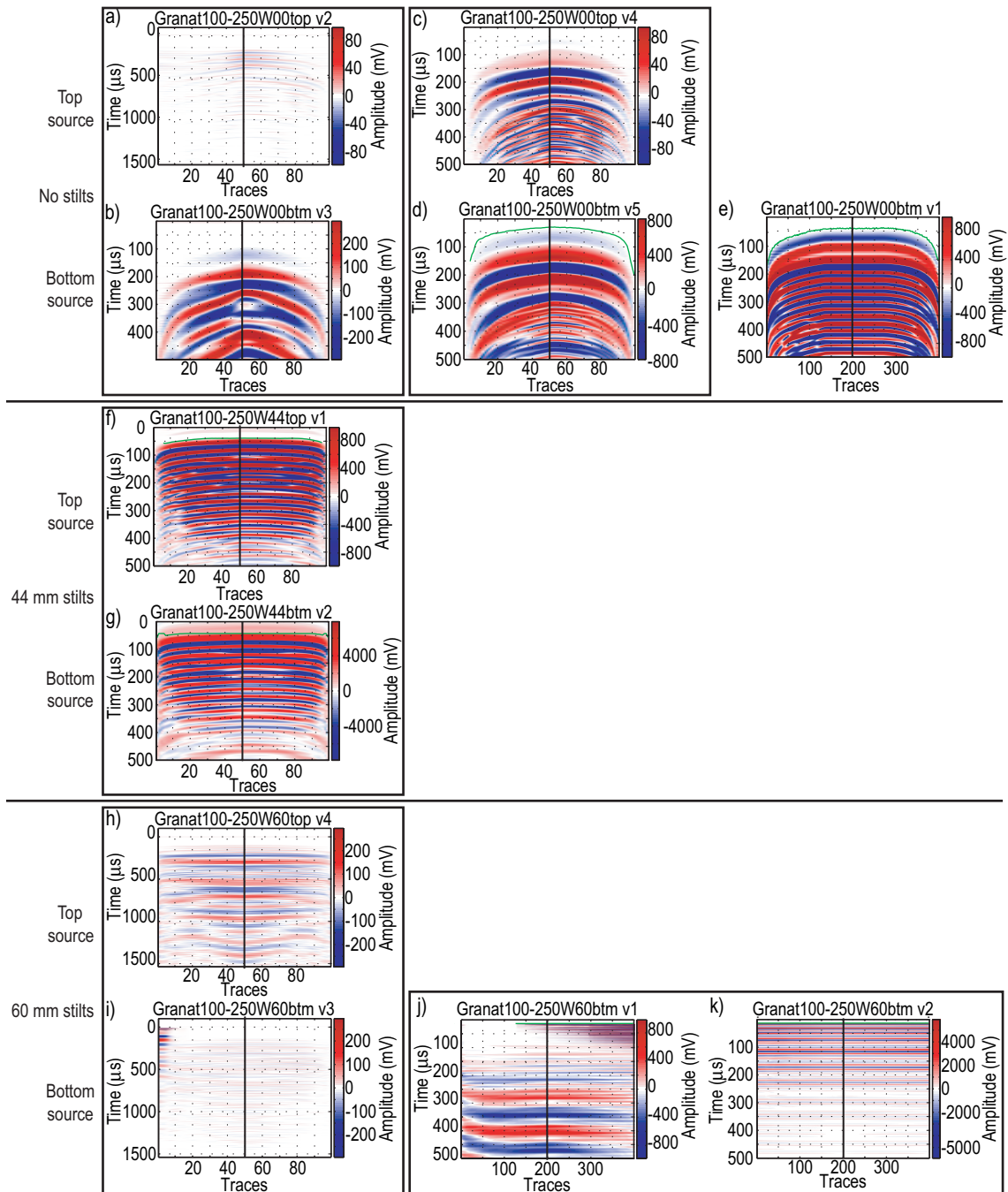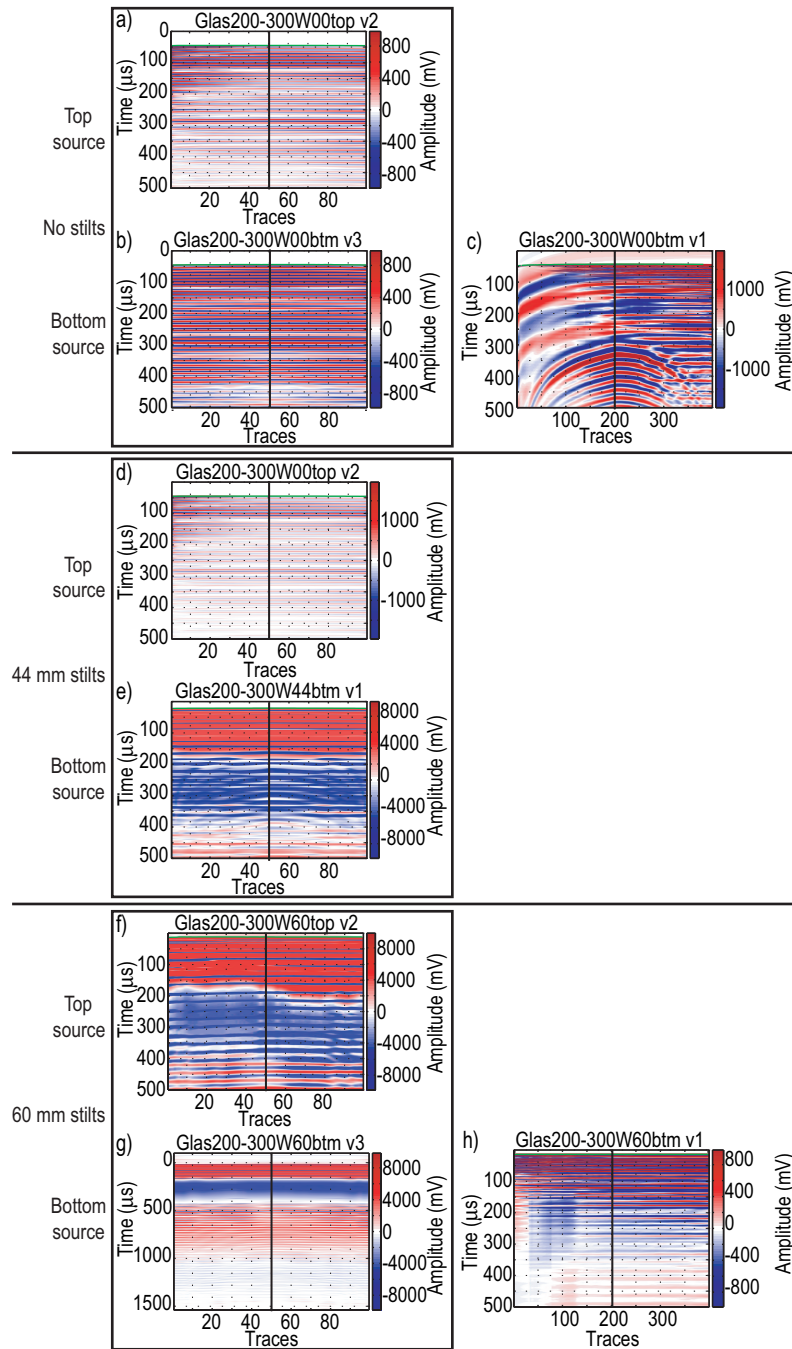
Figure 3.9: Recorded signals through garnet sand for sample thicknesses of ∼80 mm (a-e), ∼36 mm (f,g) and ∼20 mm (h-k). In each panel, the pressure is increasing from left to the center trace (delineated with the vertical black line) and decreasing from the center trace to the right. The first break pick is outlined in green.
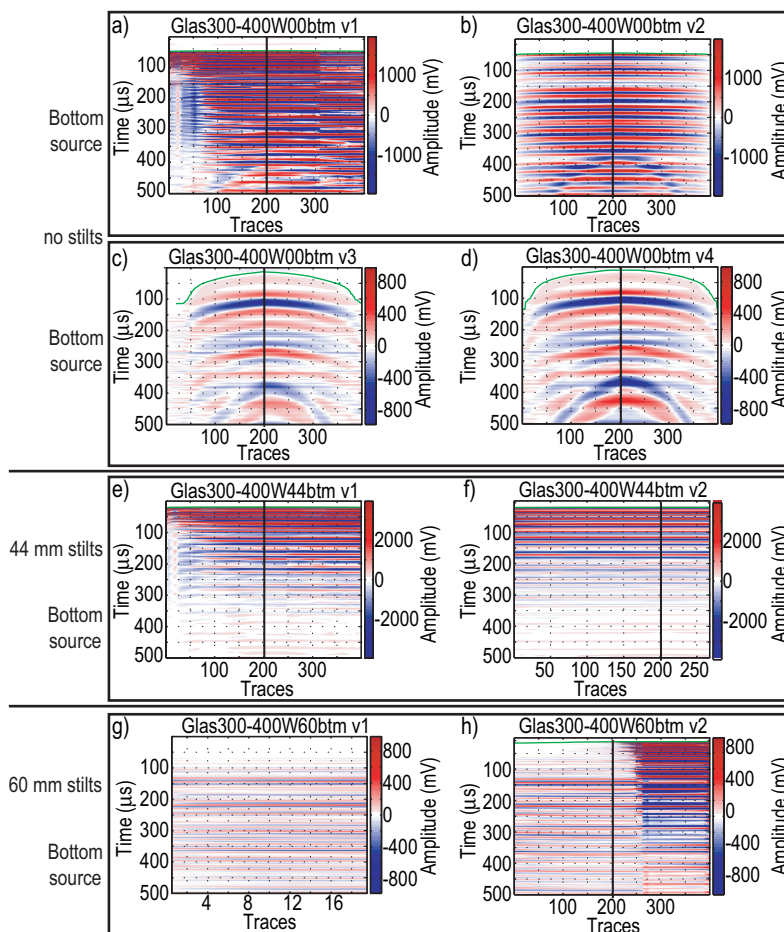
Figure 3.10: Recorded signals through glass beads (200-300 μm) for sample thicknesses of $\sim$80 mm (a-c), $\sim$36 mm (d-e) and $\sim$20 mm (f-h). In each panel, the pressure is increasing from left to the center trace (delineated with the vertical black line) and decreasing from the center trace to the right. The first break pick is outlined in green.

Figure 3.11: Recorded signals through glass beads (300-400 μm) for sample thicknesses of $\sim$80 mm (a-d), $\sim$36 mm (e-f) and $\sim$20 mm (g-h). In each panel, the first break pick is outlined in green. The pressure is increasing from left to the center trace (delineated with the vertical black line) and decreasing from the center trace to the right. In (g), the experiment was interrupted while uploading. For these measurements, only the bottom sensor acted as the source.

ior: (1) Figure 3.8h-i follow the same trend as (a-c): The arrival time (Figure 3.12) is decreasing significantly with increasing pressure, resulting in velocities ranging from <0.5 km/s at low pressures to 3.0 km/s at the "high" pressure end of 753 kPa. (2) In Figure 3.8f-g, the arrival time is decreasing slightly with increasing pressure resulting in velocities below 1 km/s. (3) In Figure 3.8d, e, and j-l, the arrival time stays constant with increasing pressure corresponding to a decreasing velocity, which is around 1.8 km/s with pressure (Figure 3.12). Neither of these results was expected. The velocity of saturated unconsolidated sand is supposed to be around 1.7 km/s and slightly increasing with pressure. In summary, three out of 12 measurements produced a

reasonable result of 1.8 km/s, however, the respective seismograms do not look reliable because there is literally no difference in the signal at different pressure stages, and the velocity decreases with increasing pressure.

The results of the measurements on garnet sand (Figure 3.9) display the same variable behavior of amplitudes due to variable coupling. The amplitudes are always higher when the bottom sensor acts as the source, except for (h) and (i), where the top source measurement obtained higher amplitudes. There, the measurement with the bottom source was conducted first, and the the top source second, hence the coupling to this sample was improved through time. Also, the
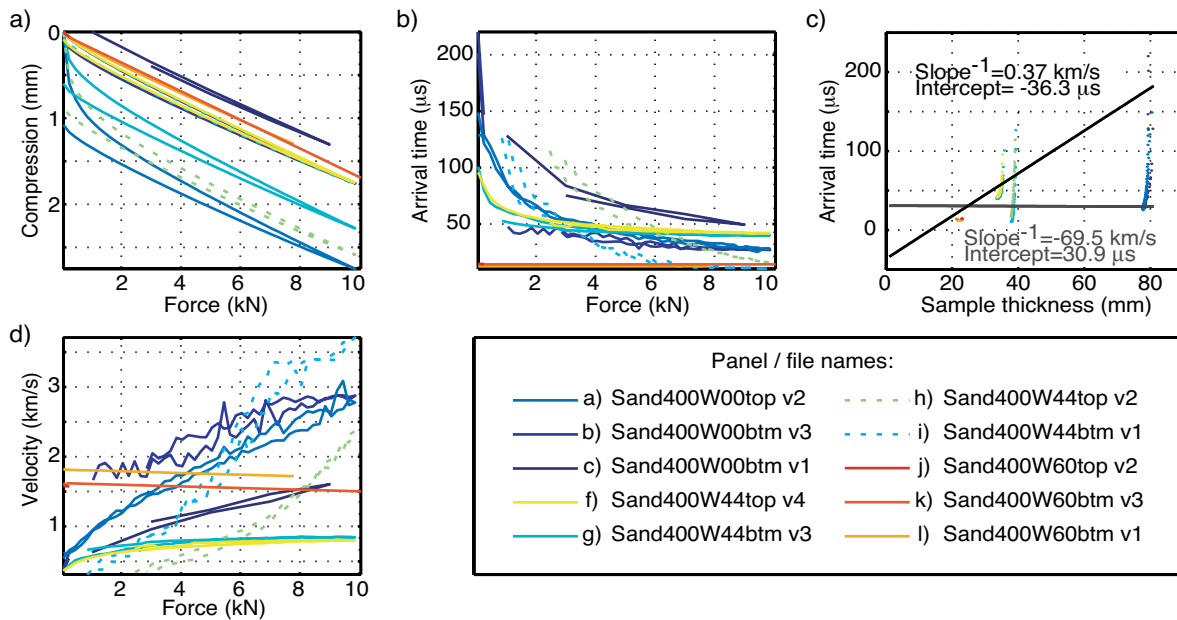
Figure 3.12: Result of quartz sand ($<$400 μm) experiments (a)-(l) shown in Figure 3.8 (colorcoded). a) Compression over force, b) picked arrival time over force, c) arrival time over sample thickness, and d) velocity over force. c) contains two linear regression curves for F$>$4800 N (flat) and for F$<$100 N (steep). The inverted slope value equals the velocity.
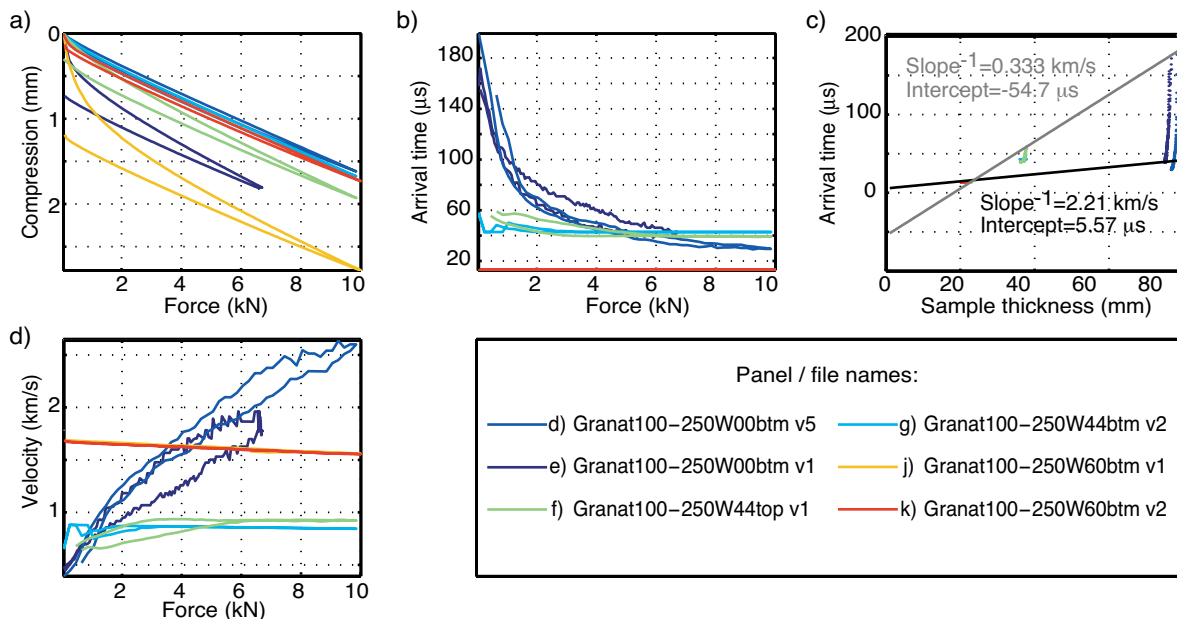

Figure 3.13: Results of garnet sand (100-250 μm) experiments (d-k) shown in Figure 3.9 (colorcoded). a) Compression over force, b) picked arrival time over force, c) arrival time over sample thickness, and d) velocity over force. c) contains two linear regression curves for F$>$9800 N (flat) and for F$<$100 N (steep). The inverted slope value equals the velocity.
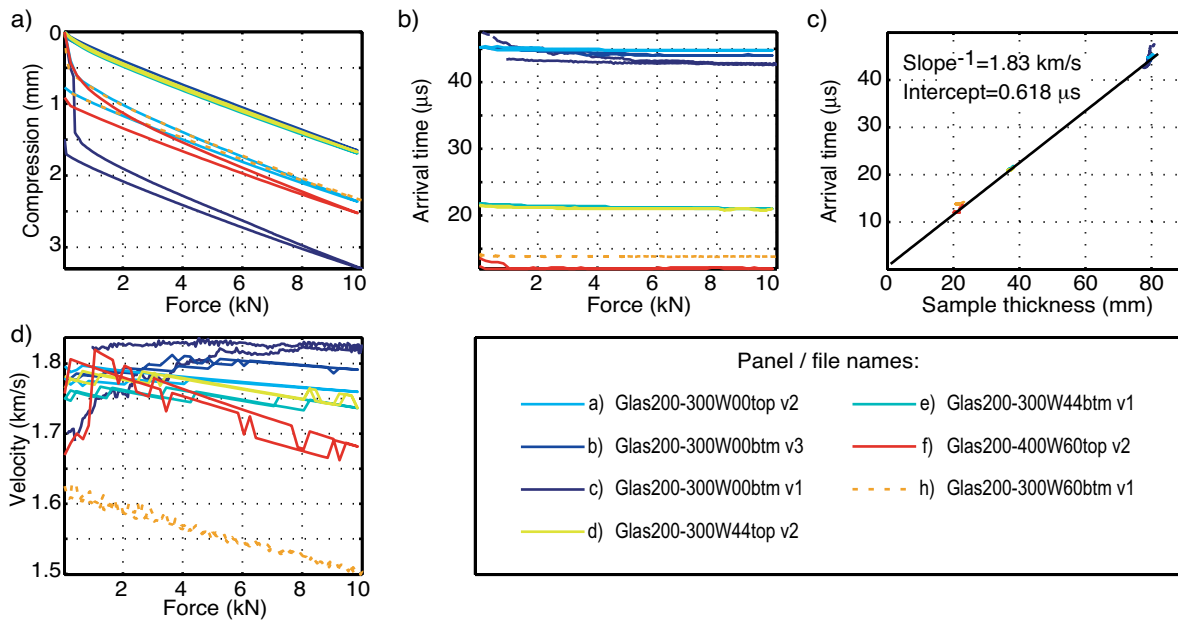
Figure 3.14: Results of glass bead (200-300 μm) experiments (a-h) shown in Figure 3.10. a) Compression over force, b) picked arrival time over force, c) arrival time over sample thickness, and d) velocity over force. c) contains a linear regression curve, whose inverted slope value equals the velocity.
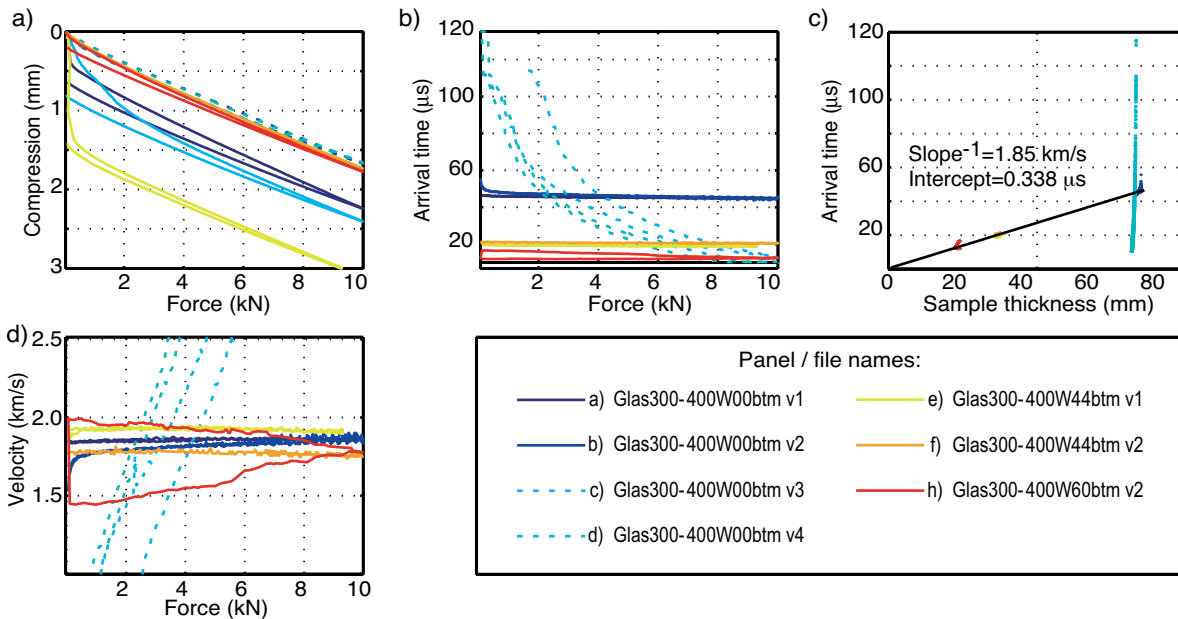

Figure 3.15: Results of glass bead (300-400 μm) experiments (a-h) shown in Figure 3.11. a) Compression over force, b) picked arrival time over force, c) arrival time over sample thickness, and d) velocity over force. c) contains a linear regression curve, whose inverted slope value equals the velocity.

amplitudes in Figure 3.9i show a serious problem, because the signal is lost at an early stage of pressure increase. The wire compartment however was dry after this measurement. Almost 50% of the garnet sand samples suffered from poor coupling (a, b, c, h, and i). The first arrivals of the poorly coupled samples were impossible to pick. The remaining samples (d, e, f, g, j, and k) display either a very large dependency on pressure (<0.5 km/s to >2.5 km/s) or a constant arrival time corresponding to a decreasing velocity with pressure, which is either at < 1 km/s or near the expected 1.7 km/ (Figure 3.13).

In summary, the results for garnet and quartz sand are inconclusive: Firstly, the first arrivals of the 80-mm samples have a very slow onset and a greater variability in signal strength, which is difficult to pick. Secondly and more importantly, the determined velocities range from 500 m/s to over 3 km/s. Measuring the slope in the third panel of Figures 3.12, 3.13 is an additional way to determine the velocity, however, for quartz and garnet sand, it is difficult to quantify. Two lines mark the slopes for pressures <100 N, and >9800 N, respectively. Neither of the slopes are equal to any of the velocities determined directly. Also, the absolute values of intercept times are quite large and, for low pressure, the regression velocity is negative. Hence, the linear regression is not a reliable measure of velocity for garnet and quartz sand, and thus also not the direct measurements.

The velocity measurement of glass beads of both 200-300 μm and 300-400 μm grain sizes shows more similarity in the seismograms (Figures 3.10 and 3.11): The arrival times are constant except in Figure 3.11c and (d), where the first arrival is very pressure dependent and of a low amplitude, indicating that the sample was less than 100% saturated. This results in an unrealistic range between <500 m/s and >3 km/s (Figure 3.15). The constant arrival times of the remaining measurements though resulted in reasonable velocities of $\sim$1.8 km/s, which is confirmed by the slopes in Figures 3.14c and 3.15c.

Regarding the amplitudes in both glass bead measurements (Figures 3.10 and 3.11), the amplitudes for the highest thickness (no stilts) are around 800-1500 mV, for a medium thickness (44-mm stilts) between 2000 and 8000 mV, and for the thinnest sample (60-mm stilts) at 800 and at 8000 mV. It is expected that the amplitude increases with decreasing thickness; and hence this discrepancy is explained with variable coupling of the transducers to the medium. In Figure 3.11, panels (g) and (h) are good examples to support this hypothesis: Where (e) and (f) have amplitudes of about 3000 mV, (g) and the first part of (h) come up to 800. Then, at trace 280 the signal amplitude increases significantly, probably because the grains of the sample shifted so that the sensor was better coupled to the medium. Overall, the amplitudes of the measurements on glass beads are higher than those on quartz and garnet sand, showing that glass beads are less attenuative.

3.5   Discussion

Besides a significant variability in amplitudes due to uneven coupling, the seismograms reveal three types of pressure behavior:

(1) A very high pressure dependency of the velocities, found mostly in the quartz (Figures 3.8 and 3.12) and garnet sand (Figures 3.9 and 3.13) samples, indicates that they contain a fraction of air. Garnet and quartz sand are less well rounded than the glass beads which inhibits the complete saturation. Garnet and quartz sand are therefore not well-suited materials for seismic physical modeling, since the fraction of gas not only changes the velocity and increases attenuation, but is also distributed unevenly, so that the velocity within the sample is heterogeneous.

(2) The velocity is decreasing slightly with increasing pressure resulting in velocities below 1 km/s. The velocity measured is closer to that of dry samples than of saturated samples, and is

probably due to bad coupling of the transducers to the material and hence erroneous.

(3) The arrival time is constant for all pressure stages resulting in a decreasing velocity with increasing pressure, which is contradictory to theory. However, in case of all glass bead experiments and their varying thickness, these constant arrival times correspond to the realistic velocity of 1.85 km/s, and even the slowness slope in Figures 3.14 and 3.15 comes to the same result, indicating that the constant arrival time may actually be a true reading. The intercept times for both glass bead readings in Figures 3.14c and 3.15c are close to zero, which also confirms the reliability of the measurements. Hence, it can also be assumed that the inverse-proportional pressure dependence is real. This phenomenon can only be explained by increasing pore pressure that causes the velocity to decrease. Even though it takes a few minutes to assume the next pressure stage in an experiment, the rim between the lid and the cylinder walls may be too small for the water to leave the system in time. However, it seems to be a too unfortunate coincidence, that the arrival time difference due to the shortening of the sample is exactly compensated by the decreasing velocity due to pore pressure.

To resolve this puzzle, I suggest to perform further experiments, where this case is reproduced, and then conduct several measurements at one pressure stage over an extended time period to find out whether the proposed pore pressure is reduced by time. If further experiments show that pore pressure can be ruled out, the error can possibly be found in the electronics: When the arrival time stays constant and there is little variation later in time for all pressure stages, it is quite reasonable to assume, that the data are erroneous. Consecutive checks confirmed that the wire compartments were dry during the experiments, but there may be other flaws in the circuitry and the file storage. An error because the sensors are not fully de-coupled from the cylinder can be ruled out, because even then the first arrival would decrease linearly with the sample thickness.

A clear loss of high frequencies from small (20 mm) to greater (80 mm) thicknesses indicates that frequency dependent attenuation studies are likely more promising than expected. Also, the ability to measure the velocity in three directions is ideal for anisotropy studies. Unfortunately, the materials I used are too attenuative to record energy over the 26-cm diameter of the sample holder. Either a smaller container needs to be equipped with sensors, or a less attenuative material has to be found. A smaller container bears the disadvantage, that energy travelling trough the cylinder walls may arrive earlier than energy through the sample. Hence, the sensors need to be fully de-coupled from the holder.

In Figure 3.10c and to a lesser degree in several other seismograms, two different wave types can be identified, one being the first arrival at $\sim$ 50 μs, that is almost independent on pressure, and much later in time (at 300 μs at trace 200) a second wave that is very dependent on pressure. This later wave probably has a much earlier onset that cannot be depicted without filtering the ringing of the first incoming wave. Nevertheless, the curvature is similar to the first arrival waves in dry samples (Figure 3.16). Hence, I assume that this second wave is the frame wave, and the first wave the fast wave through both water and frame. The water wave is probably hidden behind the ringing of the faster first arrival wave.

Dispersion is not regarded as an important issue in this case, because the sands I use are relatively permeable and our source signal has a very narrow frequency band, so that the velocities of the transmitted frequencies are assumed to be equal.
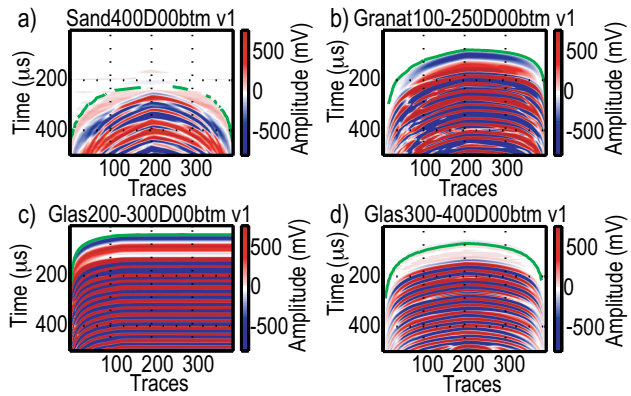
Figure 3.16: Recorded signals through ∼80 mm of dry samples of a) quartz sand (<400 µm), b) garnet sand (100-250 µm), c) glass beads (200-300 µm), an d) glass beads (300-400 µm). In panels a, b, and d, the pressure is increasing from left to the center and decreasing from the center to the right. In panel c), pressure is increasing to the center and then constant for following traces. The first break pick is outlined in green.

3.6   Conclusion

To measure the acoustic velocity of quartz sand, garnet sand, and glass beads, a known thickness of the material has been sounded by transmission and the first break arrival time determined by hand in seismograms. The measurements were taken at several pressure steps between 3.6-753 kPa and at 3 different sample thicknesses. Only the glass bead readings produced reasonable results of 1.8 km/s. The variability in the measurements of quartz and garnet sand was so huge due to a remaining fraction of air, that the true velocity cannot be deduced. Because the rough surfaces of the quartz and garnet grains inhibit full saturation both materials are not suitable for seismic physical models. Strikingly, in some experiments the arrival time remains constant with increasing pressure, which is equivalent to a velocity decrease with pressure indicating pore pressure. The reasonable velocities determined for glass beads indicate that the reading is true, however, it seems to be extremely unlikely that the decreasing velocity exactly compensates the de-

creasing thickness such that the arrival time stays constant.

The velocity measurements are by far not sufficiently precise to base model building parameters upon them. An alternative, more successful approach is introduced in Chapter 4: Applying the information that the coordination number z has an first order effect on the impedance, we performed reflection experiments on a model that simultaneously shows the impact of 16 different combinations of material and interface preparation techniques on the reflections of this interface. The results show that interfaces of layers of granular materials can be resolved depending on the interface preparation more than the material itself.

4 Seismic Imaging of Sandbox Models

Abstract

Analog sandbox simulations have been applied to study structural geological processes to obtain qualitative and quantitative insights into the evolution of mountain belts and basins. These sandbox simulations provide either 2-D information during the deformation or pseudo-3-D information after the deformation is finished. To extend the structural information to 3-D, we combine the analog sandbox simulation techniques with seismic physical modeling of sandbox models. The long-term objective of this approach is to image seismic events of static and actively deforming 3-D analog models. To achieve this objective, a small-scale seismic apparatus, composed of a water tank, a PC control unit including piezo-electric transducers, and a positioning system, was built for laboratory use. For the models, we use granular material such as sand and glass beads, so that deformations can develop during the simulation. The granular models are required to be completely water saturated so that the sources and receivers are directly and well coupled to the propagating medium. Ultrasonic source frequencies ($\sim$500 kHz) corresponding to wavelengths $\sim$5 times the grain diameter are necessary to resolve small-scale structures.

In three experiments of different two-layer models, we show that (1) interfaces of layers of granular materials can be resolved depending on the interface preparation more than on the material itself. Secondly, we show that the decompaction between the sand grains caused by a string that has been pulled through the grains, simulating a shear zone, causes a reflection that can be detected in the seismic data. In the third model, we perform a seismic reflection survey across a model that contains both the prepared interface and a shear zone, and apply 2-D-seismic reflection processing to improve the resolution. Especially for more complex models, the clarity and penetration depth need to be improved to study the evolution of geological structures in evolving models with this method. However, these experiments show that seismic imaging of shallow sandbox models, that are structurally evolving, is feasible.

4.1 Introduction

Analog sandbox simulations have been applied to study geological processes to obtain qualitative and quantitative insights into the evolution of mountain belts and basins (e. g., Koyi, 1995, 1997; Storti et al., 2000; Lohrmann et al., 2003; Gartrell et al., 2005; Hoth et al., 2007). However, the evolution of internal structures within sandbox models can only be directly observed in 2-D profiles through glass walls confining the models or indirectly by surface observations (e. g., PIV - particle image velocimetry, Adam et al., 2005). 3-D images can only be obtained by either very expensive and very elaborate X-ray tomography (Colletta et al., 1991) on small models (few centimeters), or, after the deformation is finished, by solidifying the model with transparent resin and cutting slices. This method provides high resolution 2-D slices to analyze 3-D-structures. However, after solidification, further deformation of the model is impossible. A non-invasive method that offers full 3-D information of the subsurface is offered by seismic imaging. Since the 1920s, seismic physical modeling has been a successful tool for research in wave phenomena (i.e. the kinematics of wave propagation and the validation of wave theoretical predictions). In the first experiments, optical methods were used to record surface motion (Tsuboi, 1994) or wavefronts through transparent media (Rieber, 1936, 1937; Schmidt, 1939). These experiments were performed on models such as

rods (1-D), or elastic plates (2-D and 3-D) (e. g., Berryman et al., 1958; Redwood, 1960; Purnell, 1986; Zhang et al., 1996; Wandler et al., 2007, among many others). However, before 2001 virtually all models were made of solid materials, and thus were static. Models in which the material is deformed while monitoring require viscous or granular media such as sand, but severe attenuation and scattering of seismic waves in sand prevented the application of seismic imaging methods on sandbox models (Purnell, 1986). Sherlock (1999) and Sherlock and Evans (2001) were the first to try to overcome these problems and performed zero-offset seismic surveys at the mm-scale using piezoelectric transducers (PET) on sandbox models. Currently, seismic physical modeling of granular models is limited to zero-offset traces, investigating fluid flow (Sherlock et al., 2001; Wandler et al., 2007) or fluid pressure (Cobbold and Castro, 1999). However, zero-offset-surveys in granular material suffer from strong scattering. The resulting poor signal/noise-ratio can be improved by multiple-offset surveying, but this application has been inhibited by the directionality of the PETs.

The objective of this study is to combine the analog sandbox simulation techniques with the techniques of seismic physical modeling. To achieve this objective, a new small-scale seismic apparatus for laboratory use was designed and developed, composed of a water tank, a PC control unit including specially built PETs, and a positioning system (Krawczyk et al., 2007). The goal is to apply 3-D seismic imaging methods to sandbox models subject to deformation. For the models, we use granular material such as sand and glass beads, so that the model can deform during the simulation. Because of its Mohr-Coulomb behavior, granular material localizes deformation along shear zones of reduced frictional strength (Byerlee, 1978), which are characterized as a zone of decompaction (Colletta et al., 1991; Lohrmann, 2002), i.e. lower density. The shear bands are a few grain diameters wide (2-3 mm), while the structural layers have thick-

nesses of a few millimeters to centimeters. The granular models are required to be completely water saturated so that the sources and receivers are directly and well coupled to the propagating medium. Ultrasonic source frequencies ($\sim$300-650 kHz) corresponding to wavelengths $\sim$5 times the grain diameter are necessary to be able to resolve small-scale structures. Higher frequencies generate wavelengths that are approximately as big as the grain size of the material, so that each grain acts as a scatter point causing strong attenuation.

When doing seismic physical modeling of solid or granular models, three aspects require particular attention: Scaling, transducer properties, and material properties. Scaling and the transducer properties are thoroughly investigated by Buddensiek et al. (2009). They have shown that the PETs, that we use here, are suitable to be used for seismic reflection surveys on such a small scale for source frequencies of 350-550 kHz and for incidence angles $<35°$, which corresponds to a 14-cm offset at water depths of 10 cm.

The elastic properties of a material control the wave propagation behavior, and are essential to know in order to conduct controlled experiments. This is particularly important to establish acoustic impedance contrasts between layers. However, the acoustic velocity of unconsolidated granular material under atmospheric pressure is very difficult to obtain because of high attenuation. In a numerical study, Agnolin and Roux (2008) found that the elastic moduli of granular media depend much more on the procedure (shakes, taps, vibration, lubrication, and undulatory shear) that was employed to assemble the sample than on its mineralogy. This numerical study is supported by the experimental results of Sherlock (1999) who performed reflection experiments on layer cake models. By trial-and-error, the results showed that the acoustic velocity of a granular material is of minor importance for establishing the necessary acoustic impedance con-

trasts within sandbox models. In fact, the reflections in the Sherlock (1999) models were invariably stronger than was predicted by the calculated impedance contrast. Most significant was the way the two sands combine at the interface and the contrast in grain sizes between layers. Sherlock (1999) was able to generate reflections of interfaces with near-zero-impedance contrast by having two layers of sands of different grain sizes. The impedance contrast was positive for the smaller and the bigger grains as the bottom and top layer, as well as vice versa. The reflection was stronger, however, with the small grain size on top. The author explains this phenomenon as a consequence of the combination of the two sands at the layer interface. While the porosity within both sands is equal, at the interface the small grains can settle in the spaces between the big grains and increase the density locally. Since it is impossible to deposit grains of one size onto the surface of grains of another size such that the porosity is actually higher than in either of the two layers, any interface will cause a positive reflection. Only the amplitudes will vary depending on the order of deposition. In contrast to the higher packing density at interfaces, shear zones in proper analog simulations are characterized by a decompaction of the grains along the shear plane (Colletta et al., 1991; Lohrmann, 2002). While the model is undeformed, grains are interlocked and have a homogeneous friction. Upon stress accumulation, the grains first are subject to compaction, until localized failure leads to decompaction at the shear zone of up to 10 μm (Lohrmann, 2002) as a result of the unlocking of the grains.

In this paper, we show results of reflection surveys across three types of models: The "reflectivity model" simultaneously shows the impact of 16 different combinations of material and interface preparation techniques on the reflections of this interface. The "shear band model" shows seismic images of a two-layer model before and after a string has been pulled through to simulate a shear band. The "channel model" is
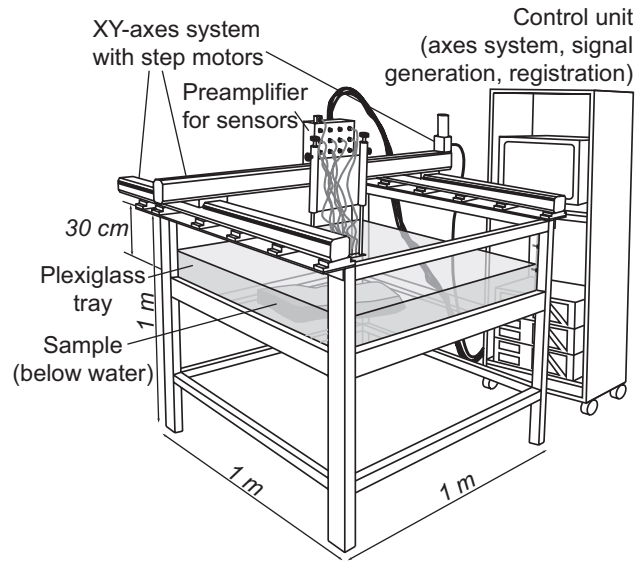

Figure 4.1: Experimental device and setup of the midget-seismic system in the laboratory. The system consists of a plexiglas tank, a control unit including piezo-electric transducers, and a positioning system.

prepared with the material combination and interface preparation technique that produced the strongest reflection in the "reflectivity model". Additionally, it contains three depressions in the interface simulating buried river channels at different offsets, and one shear band. In the next section, the experiment setup, the acquisition parameters, and processing steps will be described in detail. Then the results are presented followed by a discussion and the conclusions.

4.2 Experiment setup

4.2.1 Hardware setup

The major components of the mini-seismic system include a PC control unit, a positioning system and a plexiglas tank (Figure 4.1). The functions performed by each module are shown in Figure 4.2 and the technical specifics are given in Table 4.1 (Krawczyk et al., 2007). Before seismic acquisition, the sand models are sieved into the (center of) the tank. Next, hot tap water is slowly filled into the tank and, for good coupling,

PC system with control unit:	Industry PC (type IPC-9401).
Signal generator:	PCI-board (type MI6030);
	Max. output 125 MHz (14 bit);
	Max. 8 Msamples;
	Max. output amplitude ±3 V.
Signal amplifier:	AC voltage signal amplifier;
	Input -2 to +2 V;
	Input resistor 200 Ohm;
	Output -141 to +141 V;
	Output resistance 2 kOhm;
	Band width 20 Hz-500 kHz (-3 dB), 20 Hz-1000 kHz (-6 dB).
Preamplifier:	(Type VV30) 30 dB voltage amplification and impedance tuning;
	Frequency range 1 kHz-2 MHz;
	Max. output amplitude ±3 V.
Transient recorder:	Three 4-channel PCI-boards (type MI4022);
	For each channel signal amplifier and AD-converter;
	Max. sampling 20 MHz (14 bit);
	Max. memory 2 Msamples/channel.

Table 4.1: Technical specifications of the components in the ultrasonic recording system (Krawczyk et al., 2007).

Number of receivers:	12
Source-receiver offset:	18-150 mm
Receiver spacing:	12 mm
Shot spacing:	3 mm
Coverage:	12 fold
Source frequency:	300 to 650 kHz, interval 50 kHz
Source signal:	3 periods length (tapered with a $\cos^4$)
Sampling rate dt:	0.05 μs
Vertical stacking:	256

Table 4.2: List of acquisition and recording parameters.
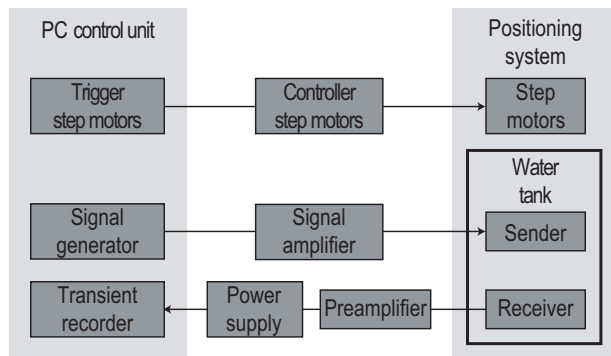
Figure 4.2: Schematic illustration of the functions performed for these experiments by the PC control unit and the positioning system modified after Krawczyk et al. (2007).

the sources and receivers are lowered into the water. After a saturation time of three to four days (Sherlock, 1999, and in Chapter 3), the seismic experiment is started. As sources and receivers, we use specially designed piezo-electric transducers (PETs) with a reduced directionality. The PETs have been tested for this multiple-offset application by Buddensiek et al. (2009). Using one transducer as a source, we record twelve receiver transducers simultaneously; the maximum number of receivers that the system can handle. The positioning system orders step motors to move the rack of PETs in the horizontal plane to any location within the tank to a precision of 0.12 mm/motor step. The transducer-rack can be build with any source-receiver geometry, however, we use a geometry comparable to marine streamer surveys as shown in Figure 4.3. The source and the receiver spacing is 18 mm to 150 mm, while the receiver spacing is 12 mm. Therefore, an offset in y-direction by ±6 mm was necessary, so that the receivers are not in contact with each other. Overall, the sources and receivers are inline, so that when the rack is pulled through the water tank in x-direction, the survey geometry is similar to that of marine streamer surveys. The shot spacing was 3 mm. The acquisition and recording parameters are given in Table 4.2. The system can excite the source transducer with different center frequencies between 100 kHz and 1 Mz. As recommended by Buddensiek et al. (2009), we use 300 kHz to 650 kHz and stack each frequency record vertically 256 times. Where indicated, we performed frequency stacks to broaden the bandwidth as a processing step.
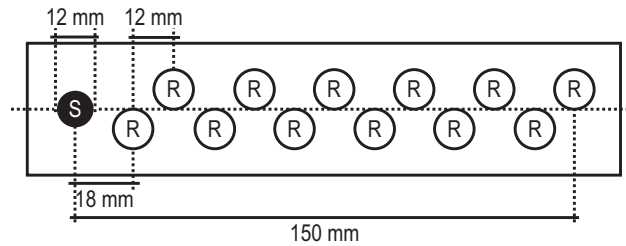
Figure 4.3: Source-receiver geometry of the transducers rack used for all our experiments. The black transducer circle delineates the source transducer (S), the white circles delineate the receiver transducers R.

4.2.2 Reflectivity model

To determine which procedure creates the strongest interface reflection, the reflectivity model contained 16 fields of interface variations according to Figure 4.4. The model borders and interfaces were outlined by thin strings taped into the tank. Thin boards were set up to prevent sand from spilling over the edges into other fields. For example, to build the bottom layer, a thin board was set up where the glass bead and the garnet sand layer meet. After both materials were sieved to a thickness of 2 cm, the board was removed. Then, for the interface preparation, the designated area was graded flat by stamping lightly with a flattening tool. Then, boards were set up at a height of 2 cm to build a borderline for the glass powder that was to be sprinkled on. The glass powder, composed of glass beads of 40-70 μm diameter, filled the intergranular space between the grains of the underlying material. In the designated area, the glass powder was graded flat. Next, the walls for the top layer were positioned and the according material was sieved in (Figure 4.5). Finally, hot tap water was slowly filled into the tank to a water depth of 10 cm above the model surface, and after a saturation time of three days, the seismic experiment was started.

Seismic profiles were acquired above the four material combination lines, so that the interface preparation varied inline (Figure 4.4). The seismic profiles were shot ~4 cm above the model surface, to ensure that only reflected en-
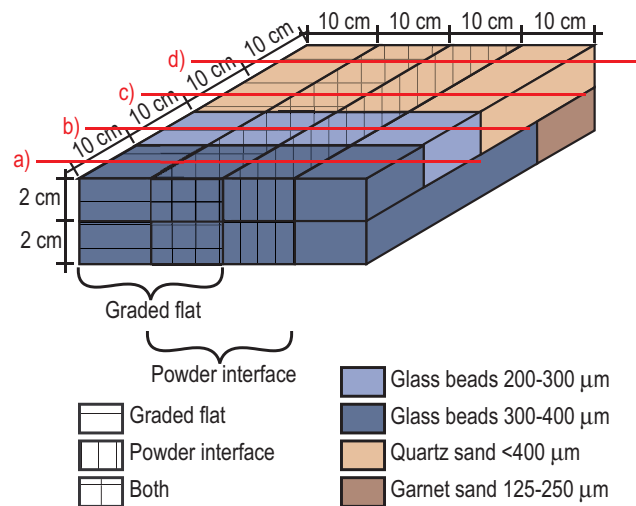

Figure 4.4: Illustration of the model used to test the reflectivity of an interface with various combinations of material and interface preparation. To prevent collapsing slopes to the sides, a sufficiently wide rim needs to be added to each side of the model. The red lines, labeled a), b), c) and d), indicate the location of the seismic profiles.
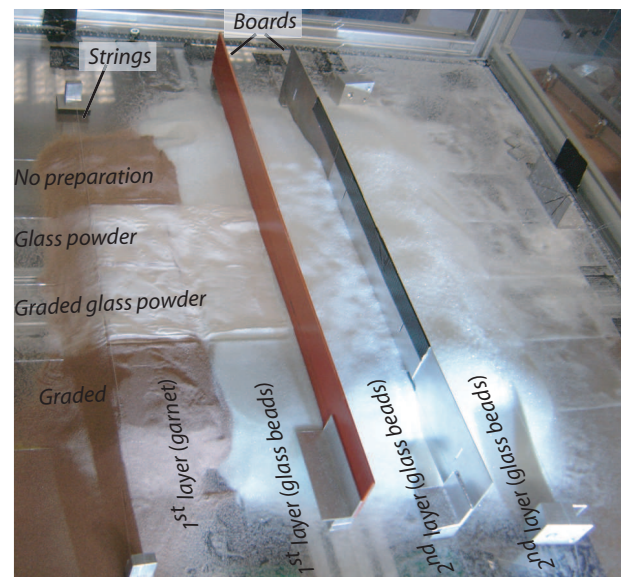

Figure 4.5: Preparation of the reflectivity model (Figure 4.4). The first layers and the interfaces are completely prepared. While on the right-hand side, the top layer is finished, the interface differences can still be seen on the left-hand side of the model. The boards are removed after the model is finished.
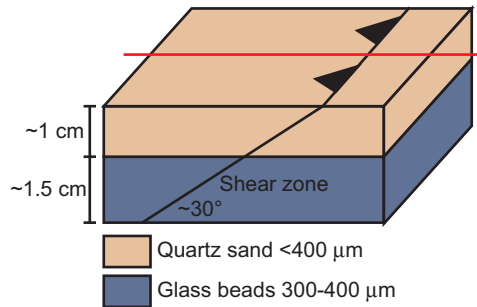
Figure 4.6: Illustration of the shear band model with a shear zone that was created by pulling a string through both layers. The red line indicates the location of the seismic profile.

ergy from the material combination underneath was recorded.

4.2.3 Shear band model

The shear band model (Figure 4.6) has a 2-cm thick bottom layer composed of 300-400 μm glass beads, which is covered by a 1.5-cm thick top layer of sand (<400 μm). In this undeformed, homogeneous state, a seismic profile was shot across the model. Next, a string was pulled through the model, so that the interlocking of the grains broke apart and caused a decompaction similar to a shear zone. The string, that was taped onto the bottom of the tank before sieving, was pulled through the model at a shallow horizontal angle perpendicular to the shotline. Then, a second profile with the same geometry as the first line was acquired. Hence, we have two seismic images of the same model, one before and one after a shear zone, to show the capability of this approach to resolve these structures. The profiles were shot approximately 10 cm above the model surface, so that the incidence angles of the reflections are fairly steep. This enables our transducers to record energy at far offsets.

4.2.4 Channel model

The channel model is a two-layer model that contains three channels at different offsets and one shear band (Figure 4.7). The bottom layer is com-
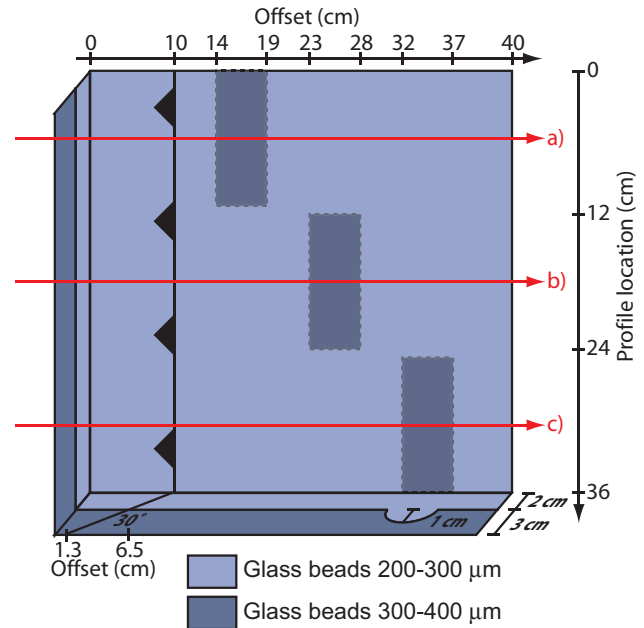

Figure 4.7: Illustration of the channel model, which includes three channels at different offsets and a shear zone. The darker blue squares in the model center indicate the hidden channels in the horizontal plane. The red lines, labeled a), b), and c), indicate the location of the seismic profiles.

posed of 300-400 μm glass beads, that were first sieved to a 2-cm height. Then a template was set on top so that further sieving prevented beads from falling into the designated channels (Figure 4.8a). Thus, another centimeter was added to the first layer (Figure 4.8b). After removal of the template, the interface was prepared applying the technique which showed the clearest reflection in the reflectivity model. First, the bottom layer was flattened with a tool and the channels gently by hand. Second, the glass powder (40-70 μm) was sprinkled on to a very thin layer, which again was graded flat. Finally, the first layer and the interface containing the channels were hidden underneath a second layer of 200-300 μm glass beads. The total thickness of the model was 5 cm. After the 3-day saturation time, a string was pulled at a 30° angle through the model (Figure 4.8c). Three seismic profiles were shot across the channels and the shear zone as indicated in Figure 4.7.
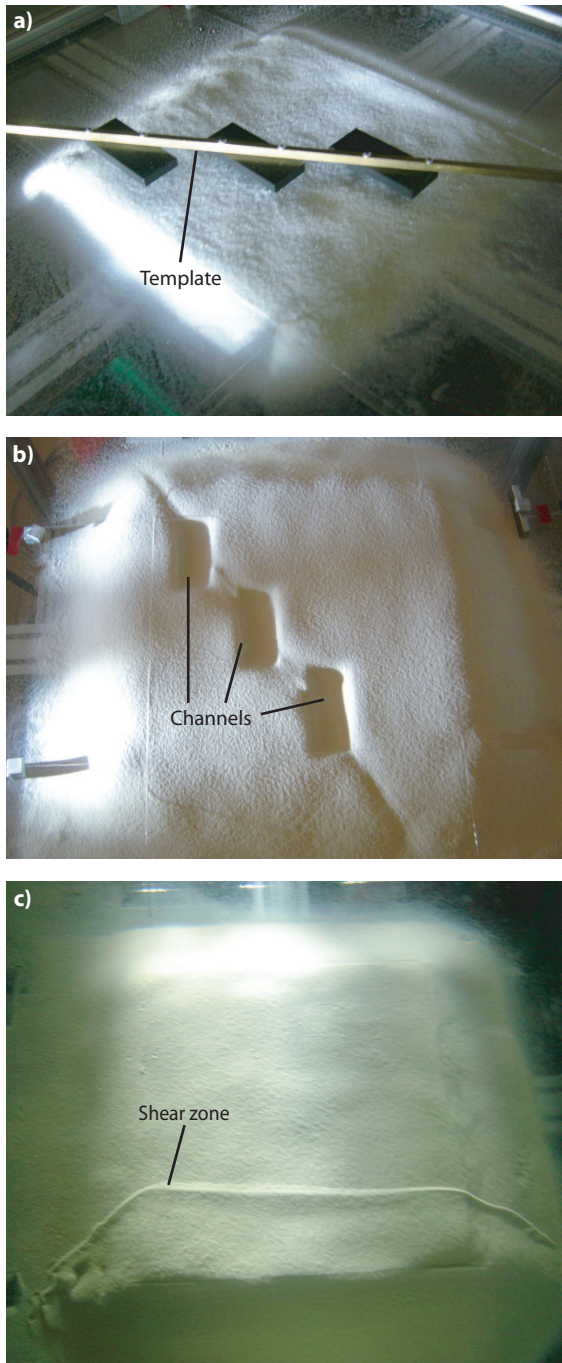
Figure 4.8: Photos of three model building phases of the channel model. a) A template to prevent sand from falling into the channels-to-be is placed above the bottom layer. b) Another centimeter of sand was sieved on top of the template, with three channels of 1-cm depth. c) The second layer hides the channels. After the saturation period, a string was pulled through the model. The surface expression shows where the string exited the model.

Reflectivity model	Shear band model	Channel model
Selection: 18-mm offset, 450 kHz	Selection: all offsets, all frequencies	Selection: all offsets, all frequencies
	Frequency stack	Frequency stack
	Spherical gain	Spherical gain
AGC (0.04 μs window)	BP filter (75,125, 750,800 kHz)	BP filter (75,125, 750,800 kHz)
	NMO stack (const. vel. 1485 km/s)	NMO stack (const. vel. 1485 km/s)
	Migration (T-K method)	Migration (T-K method)

Table 4.3: List of trace selection and processing sequence applied to the three models.

As in the shear band model, the profiles were shot approximately 10 cm above the model surface.

4.3   Results and interpretation

The selection of offset traces and source frequency data, and the processing sequence varied slightly from model to model. The details for each model are described in Table 4.3.

4.3.1   Reflectivity model

Because the seismic profiles were shot relatively near the model surface, the incidence angle decreases quickly with offset. Since the transducers are only sensitive at steep incidence angles, only the nearest offset traces (18 mm) show the differences in the interfaces clearly. Shots of eight different source frequencies were recorded. However, in order to show fairly unmodified data, we use only the data from the 18-mm offset trace of the 450 kHz source frequency shots, and discard everything else. Simple post-processing involved only an automatic-gain-control (AGC) filter to enhance the reflections of the interface and the plexiglas bottom.

Figure 4.9 shows the four seismic sections of the reflectivity model from Figure 4.4. In all profiles, the surface of the model is clearly seen at

~0.065 μs. The source signal, the reflection of the plexiglas bottom, and subsequent ringing can be clearly seen in profiles a and b, while scattering in profiles c and d adds considerable noise to the signal.

In profile a (Figure 4.9a), in which both layers are of the same material (glass beads of 300-400 μm grain size), shows small reflections at ~0.1 μs where the interface has been prepared with powder and with powder and grading. No reflection can be seen, when the interface has just been graded and, naturally, when it was not manipulated at all. The periodic signal following the plexiglas bottom reflection at ~0.13 μs shows that the wave is bouncing back and forth within the plexiglas.

The strongest reflection of the interface was recorded in Profile b (Figure 4.9b) at ~0.1 μs, where a glass bead layer of grain sizes 200-300 μm is deposited on top of a glass bead layer of size 300-400 μm. Again, the reflection is strongest where the interface was both graded flat and sprinkled with powder. In the sections where the interface was not prepared or only graded, a weak reflection can be detected. While the top layer contains a little noise, diffractions from the interface inhomogeneities sometimes obscure the bottom layer.

Both profiles c and d (Figure 4.9c and d) show no reflection at all, not even of the plexiglas bottom. Internal scattering and noise obscures every coherent signal from a layer within the model. The quartz sand in the first layer attenuated all wave energy, probably due to remaining gas that is sticking to the edges of the sand grains. The only coherent signal at ~0.13 μs is a multiple of the water bottom reflection.

Especially compared to profiles c and d, where silica sand constitutes the top layer, the glass beads in profiles a and b, are a relatively homogeneous medium generating little internal noise. Glass beads of different grain sizes and the interface preparation with both powder sprinkling and grading produce the clearest reflections and are

therefore determined to be the most suitable materials and preparation technique to image structures within, while sand grains are unfeasible for seismic imaging.

The declining slope to the right of profiles a and b is a result of the saturation. When the model was dry, the slope on the right hand side was as even as it is over the center. However, during the saturation, the slope collapsed. Hence, at least a 10-cm rim should be added around the model to prevent it from collapsing on the border.

4.3.2   Shear band model

The seismic data processing (Table 4.3) of the two profiles across the shear band model (Figure 4.6) included a frequency stack to broaden the bandwidth and a spherical gain to compensate the loss of spherical divergence. A bandpass filter was applied to remove the frequency content outside the spectrum of the frequency-stacked source signals. Seismic sections (Figure 4.10) of the shear band model before (left panels) and after (right panels) a string has been pulled through are shown as common-offset-gathers (COGs), normal-moveout-corrected (NMO) midpoint gathers, and a migrated section. The COGs at 18-mm offset (Figure 4.10a, b) are the closest equivalent to commonly recorded zero-offset data, which cannot be recorded with this setup.

In this experiment (Figure 4.10), only minor noise obscures the signal, even though the top layer is made of sand, which can be highly attenuative and add substantial scattering noise, as was shown in the reflectivity model. The plexiglas bottom at 3.5-cm depth generated a very strong reflection indicating that energy propagated through the sand with little loss.

The comparison between the images before and after the string has been pulled through the model, shows that the decompaction between the grains is sufficient to be a reflector. The trace of the string can be observed down (see arrows) to
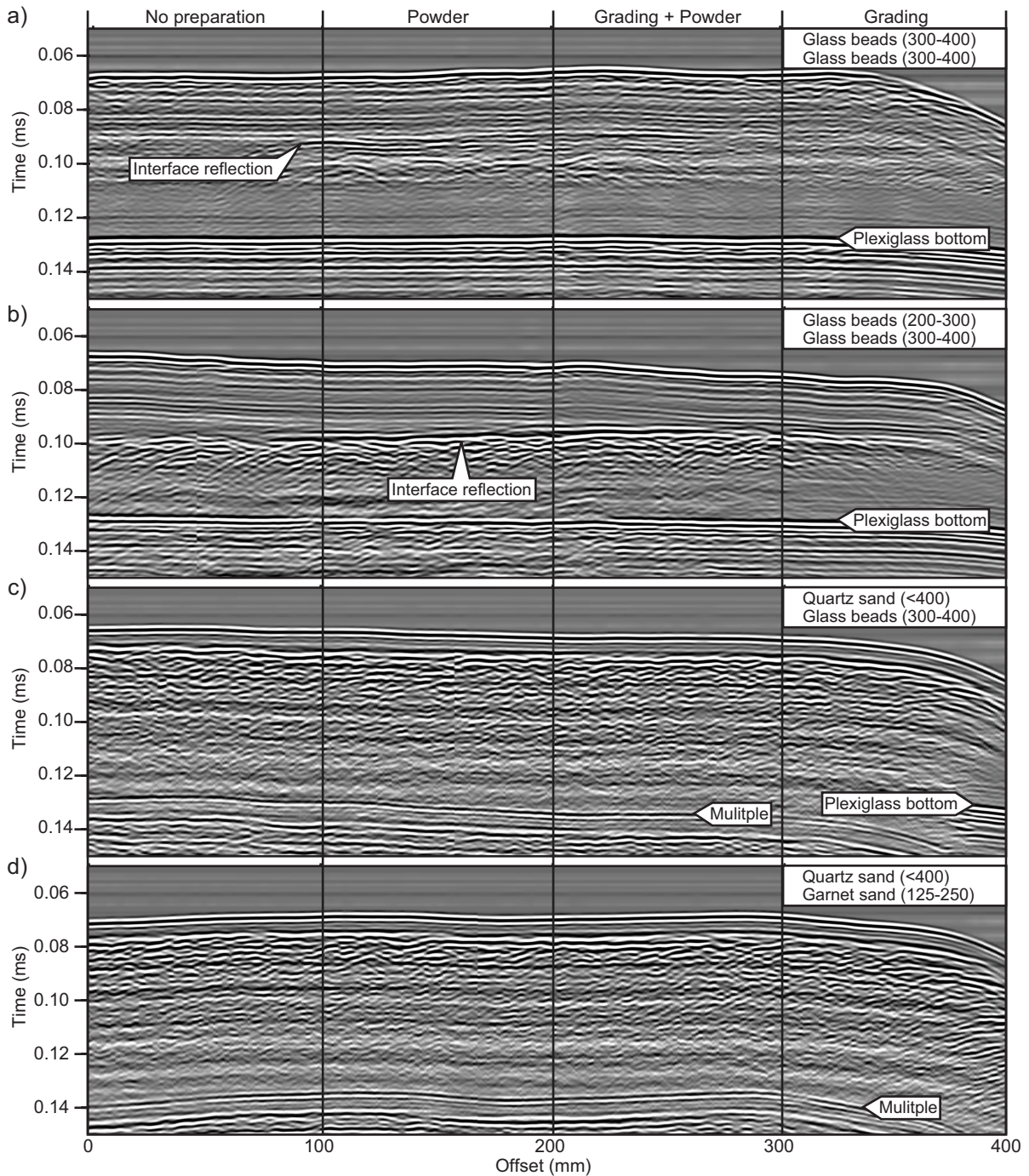
Figure 4.9: Seismic profiles a-d across the reflectivity model (for their location, see Figure 4.4). The data are are common-offset-gathers with 18 mm offset. The source center frequency was 450 kHz. An automatic-gain-control filter has been applied to the raw data. The clearest reflection of the interface was recorded in Profile b, where the surface of the bottom layer was both graded flat and sprinkled with a powder of glass beads that filled the intergranular space. Glass beads contain less internal noise than quartz and garnet sand.
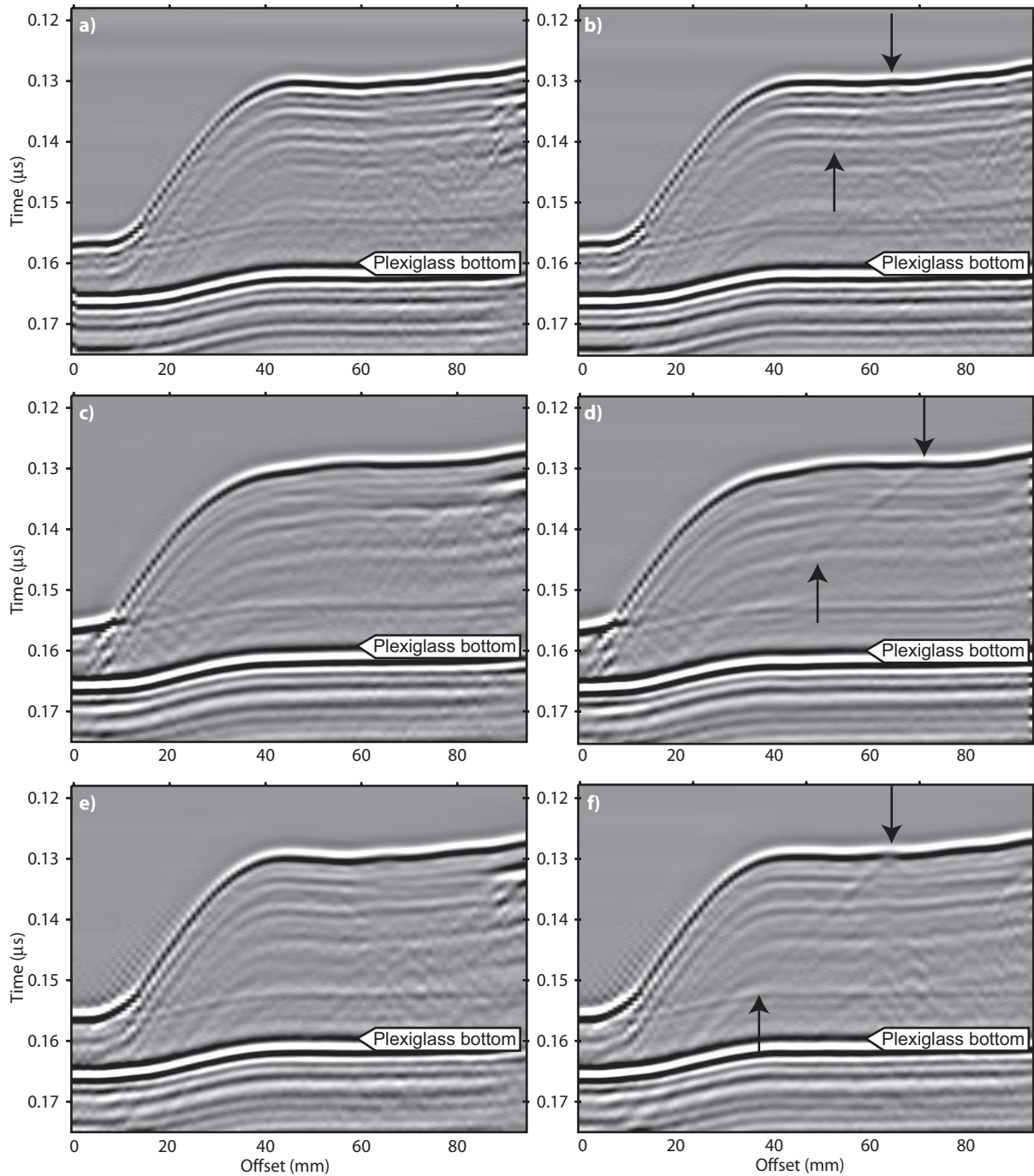
Figure 4.10: Seismic profiles across the shear band model (Figure 4.6) before (left) and after (right) a string was pulled through the model. (a) and (b) show unprocessed common-offset-gathers of the 18-mm offset trace. In (c) and (d), the data have been normal-moveout (NMO) corrected and stacked, and in (e) and (f) migrated (f-k migration). Even though the top layer is made of sand, which has proven to be highly attenuative, the shear zone (highlighted by arrows) can be followed down through the glass bead layer, almost to the plexiglas bottom. However, the interface of both layers cannot be clearly determined.

almost half the model depth in the unprocessed common-offset-gathers (Figure 4.10b). The stack of multiple-offset traces after normal-move-out (NMO) correction improves the quality, so that the shear zone can be traced down almost to the model bottom (Figure 4.10d), and the migration corrects the dip of the shear zone (Figure 4.10f) to $\sim 30°$. Despite the good resolution of the shear band, the interface of both layers is not resolved. However, multiple-offset data processing improved the seismic image of the shear zone at mm-scale, even though the source and receivers are relatively big compared to the wavelength.

4.3.3 Channel model

As indicated in Figure 4.7, three seismic profiles were shot across the channel model. Raw data before and after the frequency stack (Figure 4.11), show that the frequency stack provides a better resolution than the smaller-bandwidth signal. Subsequently, a spherical gain and a band pass filter were applied as indicated in Table 4.3. Seismic sections of the profiles are shown as common-offset-gathers (COG), normal-move-out corrected (NMO) stacks, and after migration in Figures 4.12, 4.13, and 4.14, respectively.

The signal quality is fairly good in all three profiles (Figure 4.12). The material interface caused clear reflections at ~ 0.15 μs. At the channel, the amplitudes are a little smaller, because it was impossible to uniformly grade the slopes. Due to diffractions from the channel and the horizontal part of the interface, the bottom layer is more noisy than the top layer. The plexiglas bottom can be clearly depicted in all three profiles, although the amplitudes vary. Where the interface reflection is strong, the plexiglas bottom reflection is smaller, and vice versa. Hence, for a model containing an interface reflector, the penetration depth of seismic energy is approximately 5 cm. The shear band can be detected primarily by the diffraction of the surface expression of the

model. It is by far not as clear as in the shear band model images (Figure 4.10).

The NMO stacks (Figure 4.13) show an improved signal, though some ringing remains. The shear band reflection has a little higher amplitude than in Figure 4.12. Generally, the low-frequency content has increased. After migration (Figure 4.14), the diffractions of the channel interfaces are collapsed and the profiles now have well-defined channel geometries. Also, the diffractions of the shear band surface expression are collapsed. The shear band can now be traced down almost to the interface. However, it cannot confidently be traced down to the model bottom, where its location is indicated by the arrows. Considering, that the strong reflector of the plexiglas surface has fairly small amplitudes underneath strong interface reflections, it is not surprising that the relatively small impedance contrast of the decompaction at the shear band cannot be resolved at this depth.

Since the data are time-migrated (Figure 4.14), the resolution in time and depth has to be derived from the two-way-time in μs. The two-way-time of the model surface, the interface and the plexiglas bottom is on average at 0.12 μs, 0.144 μs, and 0.187 μs, respectively. For a water velocity of 1485 m/s, this amounts to a depth of 9 cm between the transducer rack and the model surface, which is correct. The layer thicknesses were supposed to be 3 cm for the bottom and 2 cm for the top layer with a variation of a few millimeters due to the sieving precision. Assuming a constant velocity throughout the model, this amounts to a traveltime ratio between 1.3 and 1.8. The two-way-traveltime was 0.024 μs in the top layer and 0.044 μs in the bottom layer, resulting in a traveltime ratio of 1.8, the estimated upper limit. Top layer thickness of 2 cm and channel depth of 1 cm fit very well to the two-way-time of 0.024 μs and 0.012 μs, respectively, assuming a velocity of 1600 m/s for the top layer. If bottom and top layer have the same velocity, the bottom layer is 5 mm thicker than planned. This inconsistency
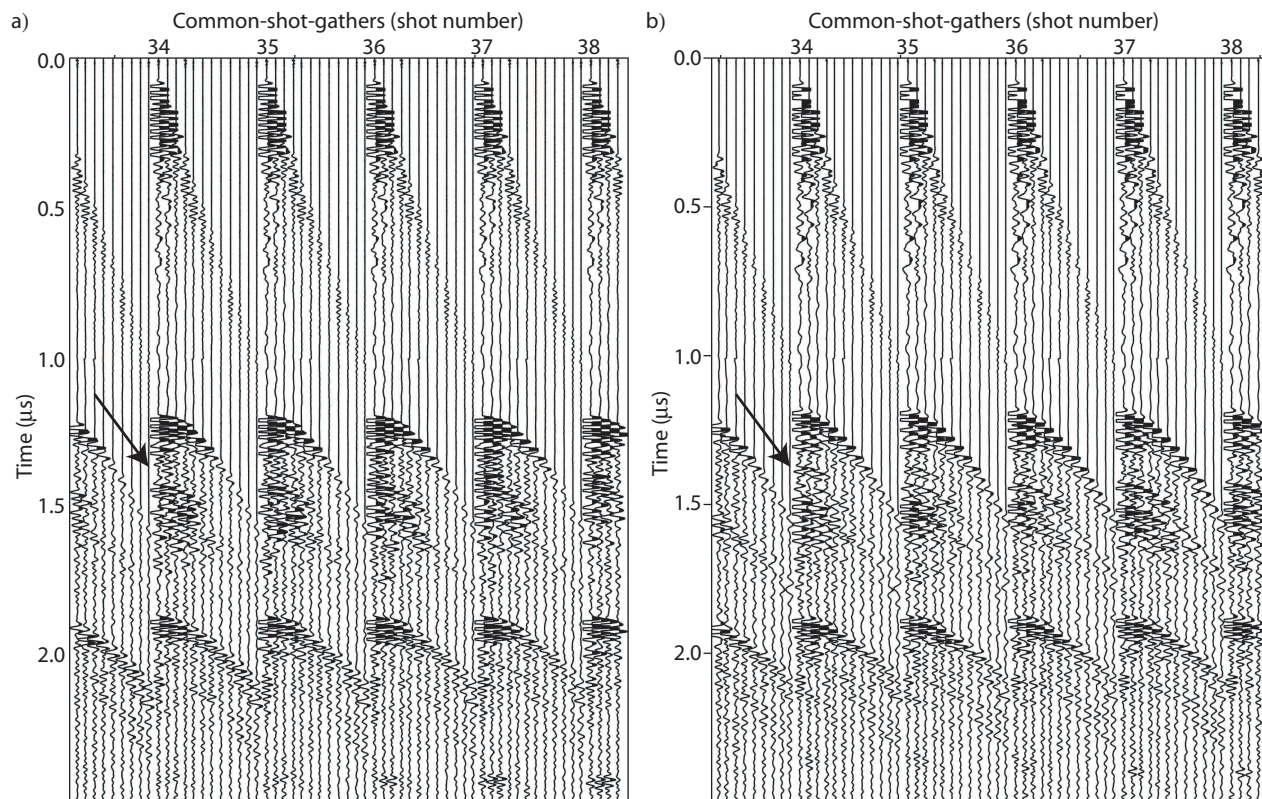
Figure 4.11: Common-shot-gathers (CSG) of the channel model, of (a) the 450-kHz recording after a spherical gain and (b) after the frequency stack followed by spherical gain. The reflection of the interface at ∼1.35 μs (arrow) is resolved better after the frequency stack.

between the model and the results can be caused by imprecise sieving, but also by a slightly false velocity assumption in the migration. More elaborate processing techniques and a more precise velocity model would improve the image quality.

4.4   Discussion

4.4.1   Results

In the following section, the results are discussed with regard to the ability to image interfaces, penetration depth, shear bands, and the general data quality. A summary of the imaging potential of all models is given in Table 4.4.

The seismic sections of the reflectivity model (Figure 4.9) and channel model (Figure 4.14) clearly showed that seismic surveys across glass beads models are more promising to produce

	Reflectivity glass beads	Reflectivity sand	Shear band sand	Channel glass beads
Interface	Yes	No	No	Yes
Shear bands	N/A	N/A	Yes	Mediocre
Penetration depth	≥4 cm	<4 cm	≥ 2.5 cm	∼5 cm

Table 4.4: Summary of the imaging potential of the reflectivity, the shear band, and the channel model, for the material saturation that was achieved and the PETs that we use as source and receivers.

clear reflections of interfaces, if they are carefully prepared. The downside of models containing interfaces is, that a substantial part of the energy is reflected. Thus, the energy-output of our source achieves a penetration depth of approximately 5 cm, which could not be improved by additional vertical stacking. None of the experiments was able to image an interface within sand. In nature, most structural geologic information is achieved by imaging interfaces, and faults are usually inferred from horizon offsets. Hence, if

it is planned to use this laboratory setup to run seismic surveys as we do in nature and compare them to the results found in nature, it is essential to have reflections of interfaces. Then, we will only get information of the first 5 cm of the model, and the internal structure has to be transferred accordingly from field to model data. The penetration depth in models with a weaker interface reflector, is probably a few centimeters higher. Because of the required resolution of 1-3 mm, the source frequency cannot be lowered to achieve a higher penetration. Alternatively, a higher energy output of the source can improve the penetration depth. However, if it is desired to perform multiple-offset processing, the source should, at the same time, emit a broad beam in the same frequency range.

Unlike field surveys, the seismic sections of the shear band model (Figure 4.10) and the channel model (Figure 4.14) showed that the decompaction due to shearing, is imaged as a reflector itself. This shear band can be traced well down to 2.5 cm depth within sand, while the seismic expression of the shear band in glass beads is much smaller. The difference between both models lies mostly in the material. The shear band model was made of sand, which has a rougher surface, i.e. friction. Therefore, the grains are prone to stay in their displaced position after the string was pulled through. The smooth glass beads are more likely to fall back into place, so that the decompaction is not a permanent expression. In this case, not even less attenuation or a stronger source would enable us to resolve the shear zone. Nevertheless, seismic imaging is able to locate zones of decompaction within models that have undergone deformation. Analog model simulations under deformation first encounter compaction before localized de-compaction occurs along the zone of failure (Lohrmann et al., 2003). Therefore, the density contrast of shear zones versus undeformed material is even higher, and should be resolved even better in evolutionary models than in this simple simulation. If interfaces are present, the faults and their offset can be seismically imaged

in glass bead models down to 2 cm. If additional interfaces are present below the depth-resolution for faults, the faults and their offset can be inferred from horizon offsets. In sand models, only the faults are well-resolved, but not the interfaces that are needed to infer an associated offset.

The seismic sections of the impedance model (Figure 4.9) show that the image quality over the glass bead profiles (a and b) is much better than over the sand profiles (c and d). The data quality of the shear band model (Figure 4.10), which also contained sand was in comparison quite good because of the smaller model dimension. Because the shear band model was shallower and narrower than the others, the hot water was able to seep in before cooling down, so that a higher degree of saturation was achieved. A bigger 3-D model composed of sand would contain more internal noise and attenuation. Since it is difficult to saturate sand models due to the rough surface of the grains, the imaging quality is variable from model to model and within one model. This result shows that sand, or any other granular material with a rough surface, is not suitable for seismic imaging with the preparation and saturation method that we use.

The discussion about the texture of the grain surfaces indicates a conflict of interest: A rough surface of the grains, i.e. higher friction, (1) creates proper shear bands that can be resolved in the seismic data, but (2) inhibits the saturation, which causes attenuation and noise. To avoid this conflict, the saturation needs to be improved. We used hot water of ~50° to saturate, and waited for 4 days until the signal did not undergo further change. Further saturation can be achieved by a vacuum chamber, vibrations, a longer saturation time, and/or saturation with near boiling hot water. A vacuum chamber is not available for a setup of this size and vibration cannot be used, since it disturbs the packing, particularly at an interface. If the saturation time is supposed to take more than four days, we recommend using des-
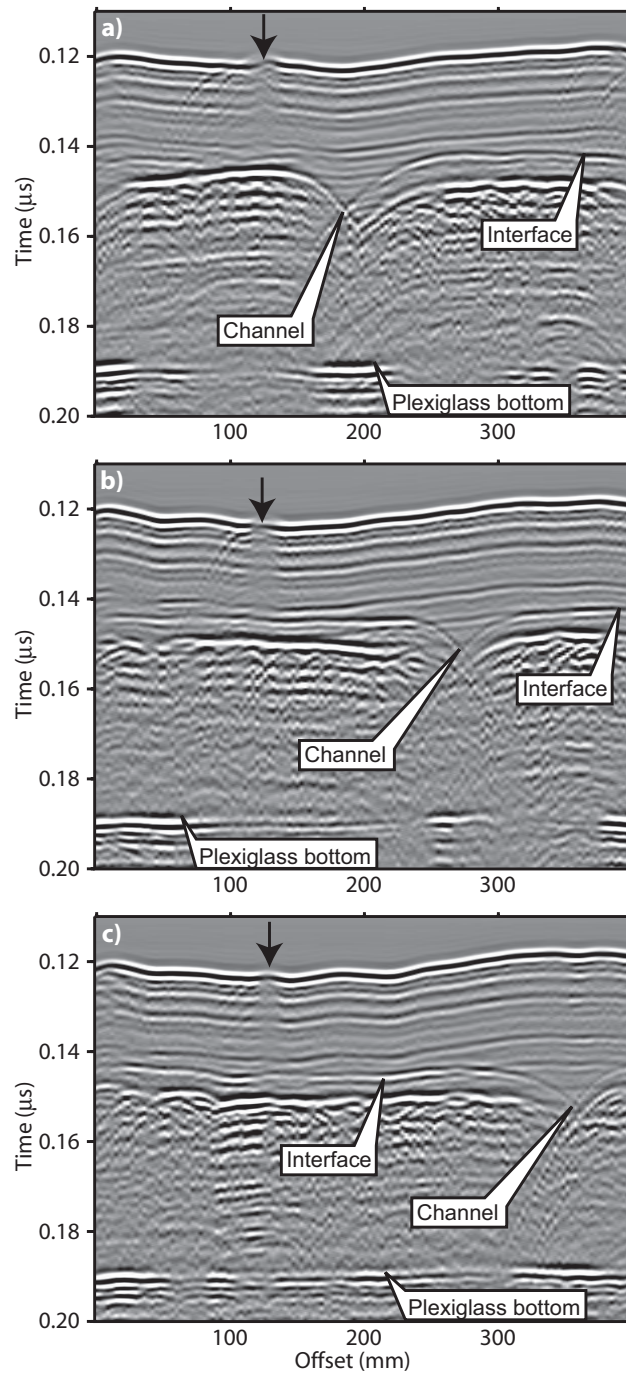
Figure 4.12: Common-offset-gathers (COG) of profiles a, b, and c across the channel model (Figure 4.7). The channel is clearly resolved in each of the profiles, however, the shear band (location indicated by arrows) is obscured by diffractions of its surface expression.
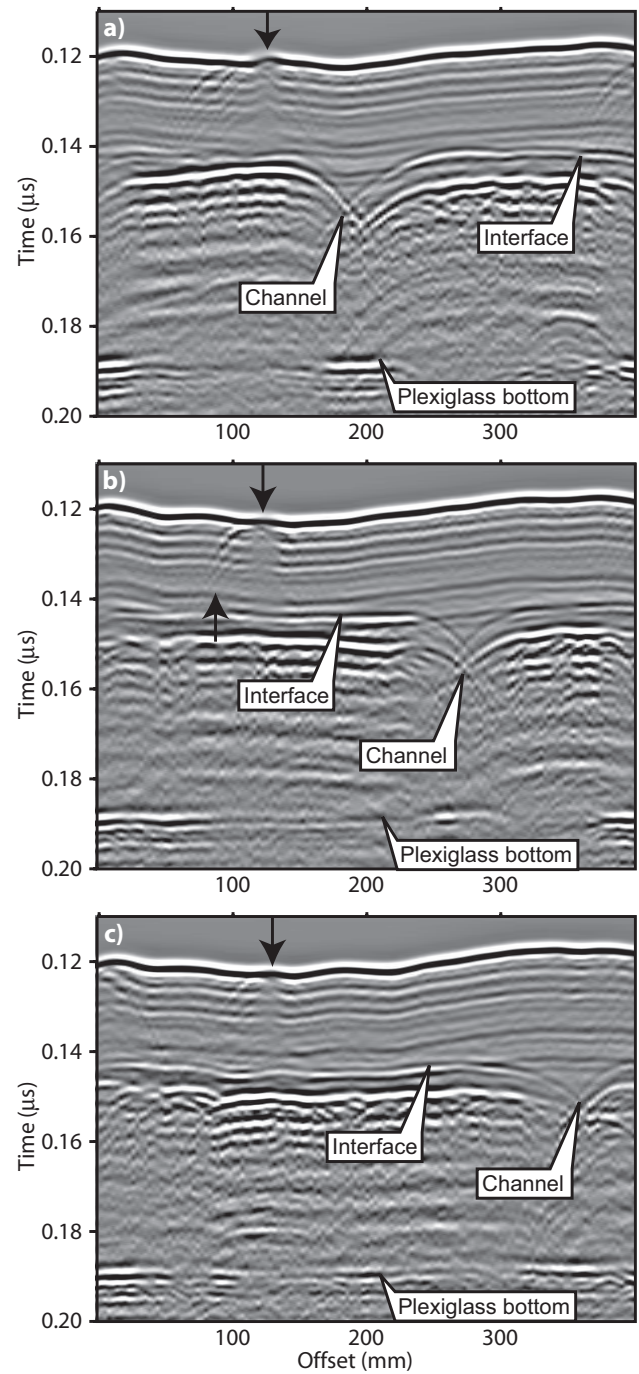
Figure 4.13: Normal-moveout (NMO) corrected and stacked sections of profiles a, b, and c across the channel model (Figure 4.7). The NMO stack improved the resolution of the shear band (location indicated by arrows) in (c) compared to the COGs in Figure 4.12.
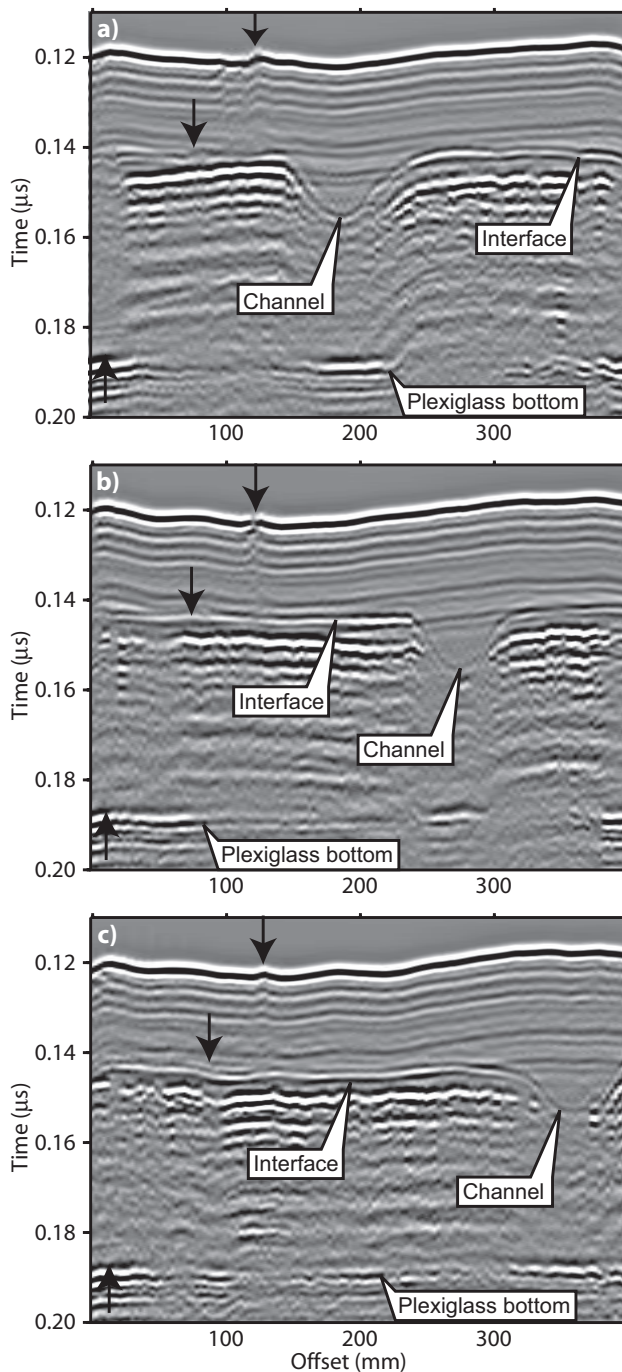
Figure 4.14: Migration images of profiles a, b, and c across the channel model (Figure 4.7). The diffractions of the channels and the shear band are removed. The channels are very well resolved, however, the shear band (location indicated by arrows) is less pronounced than it was in the shear band model (Figure 4.10).

tilled water because of algae and other organic growth.

Despite the limitations encountered during this experiment, recording multiple-offset traces and reflection processing was able to improve the image quality. Since we are able to resolve the interfaces within glass bead models, we can interpret faults in laboratory data like in field data.

4.4.2 Application to analog sandbox modeling

The application of seismic imaging techniques on analog sandbox models is most sensible, if the model deformation compares to the deformation pattern occurring in nature. A direct comparison of model and nature is possible, because suitable analog materials, such as sand or glass beads, exhibit a similar Mohr-Coulomb behavior as sediments and rocks of the upper crust. Thus, analog models are scaled geometrically to nature by the density and frictional properties of the material used in the experiments (Byerlee, 1978; Davis et al., 1983; Lohrmann et al., 2003).

When scaling the frictional properties of sedimentary rocks down to model size, the angle of internal friction is supposed to be between $20°$-$40°$, while the cohesion can be almost negligibly small (e.g. Lohrmann et al., 2003; Schreurs et al., 2006). Among the various materials that have been ring-shear-tested for these properties, sand is the most suitable because it has an appropriate angle of friction. Its cohesion, however, is too high. The angle of internal friction and cohesion of saturated glass beads have yet to be measured, to determine whether they are a suitable modeling material. For this purpose, special equipment to measure the frictional properties of saturated granular material has to be developed. When calculating the scaling factor, one has to account for the seismic experiments being performed under water, because the normal stress is reduced due to the higher density of water compared to air.

Depending on the geologic setting, the material properties, which support the seismic data quality (well-rounded, well-sorted grains), do not necessarily coincide with the required angle of friction. Among various granular materials, that have been tested for these properties, very often quartz sand of grain size <400 μm is used for regular sediments, glass beads as detachment horizons, barium sulphate for internally stronger rocks (Schemmann, 2008). For example, Lohr (2007) found that a cohesive material such as a mixture of sand (<0.63 mm, poorly-rounded) and gypsum (fine grained powder) was most suitable to simulate the structures of an extensional regime in the Northwest German Basin. For seismic modeling however, this material mixture is not appropriate because its packing is invariably inhomogeneous causing high attenuation and internal noise.

Usually, for sandbox experiments the geometric scaling factor is assumed to be 10^{-5}, even though it is recognized that it can range between 10^{-4} to 10^{-8} (Koyi, 1997; Storti et al., 2000; Hoth et al., 2007). Please note, that with the scaling factor ranging between five orders of magnitude, 1 cm in the laboratory can correspond to 100 m to 100 km in nature. Hence, the scaled seismic penetration depth and resolution depend strongly on the chosen scaling factor. No matter which scaling factor is chosen, the penetration depth in the model is 5 cm for our transducers and the resolution is a few millimeters. Choosing a lower scaling factor increases the penetration depth on the cost of the resolution. The only solution to effectively increase the penetration depth without decreasing or increasing the resolution, is a stronger source with the same wave propagation properties and frequency.

The following discussion is based on the results obtained with our equipment and, according to the convention of analog modeling studies, on a scaling factor of 10^{-5}, so that 1 cm in the model corresponds to 1 km in nature. Thus, the model and acquisition parameters and the scaled values are given in Table 4.5. Since time is not scaled by the geometric factor, frequency and velocity values are not scaled. However, they do determine the wavelength which is proportional to the resolution. For comparison, we show the values for a seismic survey across a widely deformed area in the Northwest German Basin, which led to an analog modeling study by Lohr (2007). However, the values for conventional seismic surveys can vary significantly depending on the rocks in the subsurface and the desired resolution. These scaling values demonstrate that the laboratory resolution is below that of field surveys. However, the resolution of shear bands is much better in laboratory surveys than in field experiments, where faults with small offsets are often not recognized. Nevertheless, to be comparable to field surveys, the penetration depth in the laboratory should be ≥ 15 cm, i.e. 3 times higher than it is now. In order to achieve that, the amplitude at the source has to be 9 times higher and the energy output at least 81 time higher. This is if one only considers the spherical loss and not attenuation, which is substantial in granular media.

The low penetration depth comes as no surprise, but has to be considered when planning seismic surveys across evolving analog models. For example, seismic surveys across models that are to build mountains (Schreurs et al., 2006) are not likely to show the required depth and detail of fault structures. Hence, until a source with an 100 times higher energy output is available, we suggest ultrasonic seismic surveys across rather shallow models. For example, accretionary wedge models with a low basal friction (Lohrmann et al., 2003) generate wedges of less than 6-7 cm height. Also, the extension models presented in Schreurs et al. (2006) remain fairly shallow with thicknesses of ≤ 3.5 cm. In that case, 1.5 cm of sedimentation could be added and theoretically still be resolved by seismic imaging. The sedimentation of grains in a water saturated basin, however, is creating several new issues, because smaller grains might

	Laboratory	Lab values ×10⁵	Sedimentary basin
Frequency:	∼500 kH		50 Hz
Velocity:	∼1500 mm/ms		2500 m/s
Wavelength:	∼3 mm	300 m	20 m
Shear zone width	3 mm	300 m	∼100 m
Penetration depth:	50 mm	5000 m	≥15 km
Grain size:	0.4 mm	40 m	elastic continuum

Table 4.5: Scaling between the laboratory study here and nature (example from NW German Basin; Lohr, 2007). The geometric scaling factor is assumed to be 10^{-5}, as it is commonly estimated for analog modeling studies (Koyi, 1997; Storti et al., 2000; Hoth et al., 2007).

not settle but stay in suspension, which has even worse acoustic properties.

Nevertheless, even with model thicknesses above the penetration depth, the 3-dimensional albeit shallow information gained by seismic imaging of the models would add beneficial to PIV imaging, which provides a 2-D image of high spacial and temporal resolution over the entire depth of the model. To obtain temporal information about fault development using seismic imaging, the deformation has to be intermitted at regular intervals to perform the seismic survey. Since the analog deformation is convergence-velocity independent, the long turn-around time for one experiment does not impede this procedure.

4.5   Conclusion

We have performed seismic physical modeling experiments across three different sandbox models. We used piezo-electric transducers as sources and receivers, where the source frequency was at ∼500 kHz. We recorded with 12 receivers that are offset between 18 and 150 mm from the source. The models were made of saturated granular materials like quartz and garnet sand and glass beads of various grain sizes.

The reflectivity model results show that the resolution of interfaces within granular materials

depends more on the interface preparation rather than on the material itself. The clearest reflection of the interface was recorded when the surface of the bottom layer was first sprinkled with a powder of glass beads that filled the intergranular space, and then patted flat. The seismic sections over layers composed of glass beads had less internal noise and attenuation than those made of sand. This is due to the rough surface of sand grains, where tiny gas bubbles stick to the sand during the saturation process. The remaining gas causes the attenuation.

The shear band model shows that the decompaction between the sand grains created by a string that has been pulled through the grains to simulate a shear zone, produces a reflection that can be detected in the seismic data. However, this shear band is better resolved in sand than glass beads. This again is due to the surface texture of both materials: Glass beads are so smooth that they fall back into place after the string is removed, while sand grains are more likely to stay in their displaced position.

The channel model is a two-layer model, that has the material combination and interface preparation technique that produced the strongest reflection in the reflectivity model. It also contains three channels at different offsets, and one shear band created by pulling a string through the model at an angle of 30 degrees. This model clearly resolved the depressions of the channels, but was not as successful as the sand model to resolve the shear band. Hence, here we are left to interpret fault structures by the offset of layer reflections as it is done in field experiments. Since a lot of energy is reflected at the interface, the penetration depth is approximately 5 cm for our transducers.

As long as no source with a considerably higher energy output and spherical wave emission is fabricable, we suggest performing ultrasonic seismic surveys across rather shallow models. In any case, we suggest to do ultrasonic seismic surveys in combination with PIV imag-

ing, which provides a 2-D image of high spacial and temporal resolution over the entire depth of the model. To obtain temporal information about fault development using seismic imaging, the deformation has to be intermitted at regular intervals for the seismic survey.

Lastly, we have shown that seismic reflection processing with multiple offsets was able to improve the seismic image of the structures compared to the common-offset-gathers. This is essential since most seismic physical modeling across sandbox models was done using zero-offset-surveys, which suffered from scattering from the grains. The directionality of traditional transducers has prevented the application of multiple-offset surveys, which can improve the poor signal/noise-ratio.

Besides a better control over the emitted source signal, the application of more elaborate processing techniques such as spectral whitening, deconvolution, other filters and migration techniques, and a more precise velocity model could possibly improve the resolution of our seismic images. To increase the penetration depth, both the saturation of the material needs to be improved as well as the energy output of the sources while conserving the spherical energy emission and frequency content. Despite all the encountered limitations, we have shown that mulitple-offset seismic imaging of shallow sandbox models, that are structurally evolving, is feasible.

5 Final Conclusions

5.1 Achievements

After a general introduction to analog sandbox modeling and scaling of these models, Chapter 1 introduced the project of "Seismic Imaging of Sandbox Models". The long-term objectives are defined as (1) the imaging of seismic and seismological events of actively deforming and static 3-D analog models, and (2) the assessment of the transferability of model data to field data in order to improve field data acquisition and interpretation according to the addressed geological problem. This dissertation presents the ground work necessary to achieve these goals.

First, it was shown in Chapter 2, that the piezo-electric transducers (PETs) can be used as source and receivers in seismic reflection experiments on millimeter scale for source frequencies of 350-550 kHz and for incidence angles $<35°$, which amounts to offsets less than 14 cm for a water depth of 10 cm. This frequency range allows the resolution of structures down to $\sim$2-1.5 mm dimensions, which is sufficient to resolve the structures within sandbox models. The special design of our PETs amounts to a reduced directionality compared to traditional transducers by maintaining the energy output. However, to inhibit ringing, a better control over the emitted source signal should be achieved. Additionally, the energy output is fairly low for a highly attenuative material such as sand, so that the penetration depth is only 5 cm. To be comparable to that of field surveys, the penetration depth in the laboratory should be 3 times higher than it is now, which amounts to an at least 81 times higher energy output, by maintaining the spherical energy emission and frequency content at the same time. Nevertheless, to this date, we have the most suitable transducers available to bridge the gap between the unwanted directionality and the desired energy output.

Then, in order to identify granular materials of sufficient impedance contrast to record reflections of layer interfaces, the wave propagation properties of various granular materials were investigated in Chapter 3. The results of measuring the velocity of quartz sand, garnet sand, and glass beads of different grain sizes, were inconclusive, because the acoustic properties of sediments at low pressure depend mainly on the nature of the grain contacts. Therefore, the velocity and attenuation are highly sensitive to small changes in packing, which are difficult to control. However, the use of very well-sorted materials consisting of well-rounded grains, independent of mineralogy, reduces the inhomogeneities and therefore improves the data quality.

An alternative, more successful approach to generate reflections of layer interfaces, is presented in Chapter 4: Since the procedure employed to assemble the grains has a first-order effect on the acoustic velocity, an interface that was prepared in a different way (sieving powder, grading flat) than the grains of the layers above and below, causes a reflection. Since it is not only desired to seismically image layer interfaces, but also shear bands within a deforming model, I showed that the decompaction between the sand grains created by a string that has been pulled through the grains, produces a reflection that can be detected in the seismic data. The shear band is better resolved in sand than in glass beads. Finally, results are presented that show that multiple-offset surveys and seismic reflection processing improves the data quality and resolution significantly. This result is an improvement to previous studies (Sherlock, 1999; Sherlock and Evans, 2001), in which zero-offset surveys were conducted under the assumption that the directionality of the transducers inhibits an improvement of resolution. In our case, this assumption does not hold true due to our improved PETs and to the survey geometry which

is optimized for the properties of these particular PETs.

It should be mentioned that the seismic data quality and resolution varied between models even though supposedly the same model was prepared several times. This is not unusual for sandbox modeling, where experiments tend to have a natural variation and occasional boundary effects with the glass walls which inhibit the interpretation (Schreurs et al., 2006). However, in this case, where the models have to be completely water saturated, an additional variation is imposed by the difficulty to achieve 100% saturation. One has to be prepared to perform one experiment up to ten to twenty times to finally obtain valuable data.

With these experiments and results, the feasibility of further developments in seismic imaging of sandbox models is established: Within their limits, the sources and receivers are capable of recording data of sufficient quality. If the models are prepared with appropriate materials and preparation technique, the data quality is sufficient to resolve shear bands and interfaces. Compared to field surveys, however, the penetration depth of our laboratory surveys is far below those of surveys investigating the fault structures in nature. On the other hand, while faults in field data are usually only inferred from horizon offsets, so that a fault with a small offset can easily be missed, the laboratory data were able to resolve a shear structure itself, even though it had no offset.

5.2   Perspectives

Seismic imaging of actively deforming and static 3-D analog models. Seismic imaging of actively deforming and static 3-D analog models is most sensible, if the materials used to build the model are subject to time-independent Coulomb behavior including strain hardening before failure and strain softening after failure, order to be able to compare the deformation to that in nature.

When scaling sedimentary rocks down to model size, the angle of internal friction is supposed to be between 20-40°, while the cohesion can be almost negligibly small (e.g., Lohrmann et al., 2003; Schreurs et al., 2006). Among the various materials that have been ring-shear-tested for these properties, sand is the most suitable because it has an appropriate angle of friction. Its cohesion, however, is too high. Saturated glass beads, on the other hand, have a lower friction than dry glass beads, dry sand, and saturated sand. Nevertheless, its angle of internal friction and cohesion have yet to be obtained, to determine whether they are also a suitable modeling material. Depending on the geologic setting, the material properties, which support the seismic data quality (well-rounded, well-sorted grains), do not necessarily coincide with the required angle of friction. For example, Lohr (2007) found that a cohesive material such as a mixture of sand ($<$0.63 mm, poorly-rounded) and gypsum (fine-grained powder) was most suitable to simulate the structures of an extensional regime in the Northwest German Basin. For seismic modeling, however, this material has high attenuation, and inhomogeneous packing, which degrades the data quality.

Additionally, even if the perfect medium is found for both structural modeling and seismic imaging, the low penetration depth of our transducers limits the information gained to $\sim$5 cm below the model surface. Because the geometric scaling factor can range between 10^{-4} to 10^{-8} (Koyi, 1997; Storti et al., 2000; Hoth et al., 2007), these 5 cm penetration can correspond to 500 m to 500 km in nature. However, increasing the scaled penetration depth by changing the scaling factor, proportionally decreases the scaled resolution. Usually, for sandbox experiments the geometric scaling factor is assumed to be 10^{-5}, so that the seismic data have a penetration depth corresponding to 5 km and a resolution of $\sim$200 m. These scaled values demonstrate that the laboratory penetration depth and resolution is far below those of surveys investigating the fault struc-

tures in nature due to the small power output of our transducers. However, the resolution of shear bands is much better in laboratory surveys than in field experiments, where faults with no offsets are often not recognized.

Until a source with an 100 times higher energy output is available, I suggest to do ultrasonic seismic surveys across rather shallow models, such as accretionary wedge models with a low basal friction (Lohrmann et al., 2003) or extension models similar to the benchmark experiments in Schreurs et al. (2006). In any case, the 3-D though shallow information gained by seismic imaging is valuable, particularly in combination with PIV imaging, which provides a 2-D image of high spacial and temporal resolution over the entire depth of a model (Adam et al., 2005). To obtain temporal information about fault development by seismic imaging, the deformation has to be intermitted at regular intervals for the seismic survey. Since the analog deformation is convergence-velocity independent, the only disadvantage of this procedure is the very long turnaround time for one experiment. Considering that only one out of ten experiments generates valuable data, this can be extremely time-consuming.

A comparison between model data and field data suffers from the different reasons that cause reflections. In sandbox models any fault or shear zone is a zone of decompaction, while interfaces are a zone of locally higher density. In nature, reflections are due to impedance contrasts which depend on the densities and acoustic velocities of the neighboring materials. Therefore, comparisons between reflection amplitudes and other seismic attributes of model and natural data are invalid. However, this system is ideal to test acquisition parameters on structural geological models to see which resolves the structures best. For this purpose, though, we recommend solid models with actual density contrasts, which have the advantage of almost loss-less wave propagation (compared to granular models), and the possibility to create models with proper impedance

contrasts. Most seismic physical modeling laboratories (e. g. University of Houston, University of Calgary, Curtin University of Technology, Delft University of Technology) nowadays work on solid models for exactly that reason and with exactly that objective.

An alternative idea is to apply seismic imaging to analog models containing viscous material for deformation. The viscous material bears the advantage of lower attenuation compared to sand. For example, when studying mantle deformation (Schellart, 2004b,a, 2005; Boutelier and Cruden, 2008; Boutelier and Chemenda, 2008), several different viscous materials of different density and therefore impedances are used, so that seismic reflection imaging and seismic tomography would provide detailed information about the subsurface structures. Some analog models use a combination of a viscous material and sand, for example the extension experiments in Schreurs et al. (2006), experiments that incorporate a viscous décollement (Costa and Vendeville, 2002) or a preexisting basement fault (Gartrell et al., 2005). Analog experiments on diapir growth (Childs et al., 1993; Vendeville et al., 1995; Guglielmo et al., 2000, among many others) are often simulated by a viscous material representing the diapir material, overlain by denser, granular material acting as the sediment cover. When the cover is thin, active seismic experiments would be able to image both the diapir growth and sediment deformation due to the growth. Additionally, it might be possible to obtain information about the sub-diapir structures, if the velocities in the viscous material are not much higher than in the granular material. Regarding salt structures, and associated hydro carbon traps, sub-diapir imaging could be the most profitable use of this setup, since field data lack this desperately wanted information.

Seismological imaging of actively deforming 3-D analog models. The seismological aspect of this study has been neglected so far. The idea is to passively

record seismic energy while deforming a model. If the deformation is localized along fractures, which is true for Mohr-Coulomb materials, the location and the fracture propagation can be resolved spatially and temporally by recording their acoustic emissions. The recording instruments must be sensitive in the frequency range, that these emissions generate, which is unknown to this date. The transducers that have been used for the active seismological surveys are most sensitive at 400 kHz, which is probably too high to record these earthquakes. However, broad band transducers are available and are commonly used to record the acoustic emissions in highly-pressurized rock samples (i.e., Stanchits et al., 2006) or in mining tunnels (Plenkers et al., 2008; Nakatani et al., 2009). Once, suitable recording instruments have been deployed in the tank, it has to be investigated whether the signal is corrupted by the noise, that is generated by the engines driving the deformation and the conveyor belt sliding on the base. It can be assumed that the amplitude of this noise is much higher than that of the "earthquakes" generated by the deformation of the model. However, the frequency range of the noise quite likely does not overlap with that of the earthquakes, so that it might not be recorded by the sensors or can be easily filtered from the data.

Acknowledgements

References

Adam, J., J. L. Urai, B. Wieneke, O. H. Oncken, K. Pfeiffer, N. Kukowski, J. Lohrmann, S. Hoth, W. van der Zee, and J. Schmatz, 2005, Shear localisation and strain distribution during tectonic faulting - new insights from granular-flow experiments and high resolution optical image correlation techniques: Journal of Structural Geology, **27**, 283–301.

Agnolin, I. and J. N. Roux, 2008, On the elastic moduli of three-dimensional assemblies of spheres: characterization and modeling of fluctuations in the particle displacement and rotation.: International Journal of Solids and Structures, **45**, 1101–1123.

Alhussain, M., B. gurevich, and M. Urosevic, 2008, Experimental verification of spherical-wave effect on the avo response and implications for three-term inversion: Geophysics, **73**, C7–C12.

Bacharach, R. and A. Nur, 1998, High-resolution shallow-seismic experiments in sand, part i: Water table, fluid flow, and saturation: Geophysics, **63**, 1225–1233.

Batzle, M., D. Han, and J. Castagna, 1996, Attenuation and velocity dispersion at seismic frequencies: 66th Annual SEG Meeting, Expanded Abstracts, 1687–1690.

Berryman, L. H., P. L. Goupillard, and K. H. Waters, 1958, Reflections from multiple transition layers: Geophysics, **23**, 244–252.

Biot, M., 1956a, Theory of propagation of elastic waves in a fluid saturated porous solid; I-low frequency range: Journal of the Acoustical Society of America, **28**, 168–178.

——, 1956b, Theory of propagation of elastic waves in a fluid saturated porous solid; II-high frequency range: Journal of the Acoustical Society of America, **28**, 179–191.

Blangy, J. P., S. Strandenes, D. Moos, and A. Nur, 1993, Ultrasonic velocities in sands - revisited: Geophysics, **58**, 344–356.

Boutelier, D. A. and A. I. Chemenda, 2008, Exhumation of UHP/LT rocks due to the local reduction of the interplate pressure: thermo-mechanical physical modeling: Earth and Planetary Science Letters, **271**, 226–232.

Boutelier, D. A. and A. R. Cruden, 2008, Impact of regional mantle flow on subducting plate geometry and interplate stress: insights from physical modelling: Geophysical Journal International, doi: 10.1111/j.1365–246X.2008.03826.x.

Brandt, H., 1960, Factors affecting compressional wave velocity in unconsolidated marine sand sediments: Journal of the Acoustical Society of America, **32**, 171–179.

Buddensiek, M. L., C. M. Krawczyk, N. Kukowski, and O. Oncken, 2009, Performance of piezoelectric transducers in terms of amplitude and waveform: Geophysics, in press.

Byerlee, J., 1978, Friction of rocks: Pure Applied Geopysics, **116**, 615–626.

Childs, C., S. J. Easton, B. C. Vendeville, M. P. A. Jackson, S. T. Lin, J. J. Walsh, and J. Watterson, 1993, Kinematic analysis of faults in a physical model of growth faulting above a viscous salt analogue: Tectonophysics, **228**, 313–329.

Chotiros, N. P., 1995, Biot model of sound propagation in water-saturated sand: Journal of the Acoustical Society of America, **97**, 199–214.

Cobbold, P. R. and L. Castro, 1999, Fluid pressure and effective stress in sandbox models: Tectonophysics, **301**, 1–19.

Colletta, B., J. Letouzey, R. Pinedo, J. F. Ballard, and P. Bale, 1991, Computerized X-ray tomography analysis of sandbox models: examples of thin skinned thrust systems: Geology, **19**, 1063–1067.

Costa, E. and B. C. Vendeville, 2002, Experimental insights on the geometry and kinematics of fold-and-thrust belts above weak, viscous evaporitic décollement: Journal of Structural Geology, **24**, 1729–1739.

Davis, D., J. Suppe, and F. A. Dahlen, 1983, Mechanics of fold-and-thrust belts and accretionary wedges: Journal of Geophysical Research, **88**, 1153–1172.

Dellinger, J. and L. Vernik, 1994, Do traveltimes in pulse-transmission experiments yield anisotropic group or phase velocities?: Geophysics, **59**, 1774–1779.

Domenico, S. N., 1977, Elastic properties of unconsolidated porous sand reservoirs: Geophysics, **42**, 1339–1368.

Ebrom, D. A. and J. A. McDonald, 1994, Seismic physical modeling, *in* McDonald, J. A., ed., Seis-

mic Physical Modeling, 1–3, Soc. of Expl. Geophys., 15 edition.

Elliott, S. E. and B. F. Wiley, 1975, Compressional velocities of partially saturated, unconsolidated sands: Geophysics, **40**, 949–954.

Gartrell, A., C. Hudson, and B. Evans, 2005, The influence of basement faults during extension and oblique inversion of the makassar straits rift system: Insights from analog models: AAPG Bulletin, **89**, 495–506.

Gassmann, F., 1951, Elastic waves through a packing of spheres: Geophysics, **16**, 673–685.

Green, D. H. and R. Esquivel-Sirvent, 1999, Acoustic behavior at the fluid/solid transition of kaolinite suspensions: Geophysics, **64**, 88–92.

Guglielmo, G., B. C. Vendeville, and M. P. A. Jackson, 2000, 3-D visualization and isochore analysis of extensional diapirs overprinted by compression: AAPG Bulletin, **84**, 1095–1108.

Hamilton, E. L., 1972, Compressional-wave attenuation in marine sediments: Geophysics, **37**, 620–646.

Hampel, A., J. Adam, and N. Kukowski, 2004, Response of the tectonically erosive south peruvian forearc to subduction of the Nazca ridge: Analysis of three-dimensional analogue experiments: Tectonics, **23**, TC5003.

Han, D., 1994, Weak cementation effect on velocities of sands: 64th Annual SEG Meeting, Expanded Abstracts, 1069–1072, Soc. of Expl. Geophys.

Han, D., A. Nur, and F. D. Morgan, 1986, Effects of porosity and clay content on wave velocities in sandstones: Geophysics, **51**, 2093–2107.

Hilterman, F. J., 1970, Three-dimensional seismic modeling: Geophysics, **35**, 1020–1037.

Hoffmann-Rothe, A., N. Kukowski, and O. Oncken, 2004, Phase dependent strain partitioning in obliquely convergent settings: Bollettino di Geofisica, **45**, 93–97.

Hoth, S., S. A. Hoffmann-Rothe, and N. Kukowski, 2007, Frontal accretion - an internal clock for bivergent wedge deformation and surface uplift: Journal of Geophysical Research, **112**, 1–17.

Hubbert, M. K., 1937, Theory of scale models as applied to the study of geological structures: Geological Society American Bulletin, **48**, 1459–1520.

Kaufman, S. and W. L. Roever, 1994, Laboratory studies of transient elastic waves, *in* McDonald, J. A., ed., Seismic physical modeling, 103–111, Soc. of Expl. Geophys., 15 edition. Reprinted from Proceedings of the Third World Petroleum Congress, 1951, pages 537-545.

Koyi, H. A., 1995, Mode of internal deformation in sand wedges: Journal of Structural Geology, **17**, 293–300.

———, 1997, Analogue modeling: From a qualitative to a quantitative technique: A historical outline: Journal of Petroleum Geology, **20**, 223–283.

Krautkrämer, J. and H. Krautkrämer, 1986, Werkstoffprüfung mit Ultraschall: Springer Verlag.

Krawczyk, C. M., M. L. Buddensiek, J. Philipp, N. Kukowski, and O. Oncken, 2007, Midget seismic in sandbox models - hardware setup and first data generation: 69th Annual EAGE Conference, Expanded Abstracts, Expanded Abstracts, E042.

Lohr, T., 2007, Seismic and sub-seismic deformation on different scales in the NW german basin: PhD thesis, Freie Universität Berlin.

Lohrmann, J., 2002, Identification of parameters controlling the accretive and tectonically erosive mass-transfer mode at the south-central and North Chilean forearc using scaled 2D sandbox experiments: PhD thesis, Freie Universität Berlin.

Lohrmann, J., N. Kukowski, J. Adam, and O. H. Oncken, 2003, The impact of analogue material properties on the geometry, kinematics, and dynamics of convergent sand wedges: Journal of Structural Geology, **25**, 1691–1711.

Marion, D., A. Nur, H. Yin, and D. Han, 1992, Compressional velocity and porosity in sand-clay mixtures: Geophysics, **57**, 554–563.

Marion, D. and H. Yin, 1988, A model of porosity and velocity for sand-clay mixtures: Stanford Rockphysics Project, **33**, 303–316.

Mavko, G. and T. Mukerji, 1995, Seismic pore space compressibility and Gassmann's relation: Geophysics, **60**, 1743–1749.

Mavko, G., T. Mukerji, and J. Dvorkin, 1998, The rock physics handbook: Cambridge University Press.

Mehta, C. H., 1983, Scattering theory of wave propagation in a two-phase medium: Geophysics, **48**, 1359–1370.

Nakatani, M., G. Dresen, J. Philipp, Y. Yabe, G. Morena, M. Naoi, K. Plenkers, G. Kwiatek, H. Ogasawara, K. Nagata, H. Kawakata, S. Stanchits,

and J. W. G. (2008), 2009, Acoustic emission observation in a stressed hard rock pillar in a deep gold mine in south africa: Technical overview and evaluation of observation performance: Pure and Applied Geophysics, submitted.

Nur, J. D. A., 1996, Elasticity of high-porosity sandstones: Theory for two North Sea data sets: Geophysics, **61**, 1363–1370.

O'Brien, P. N. S. and M. P. Symes, 1994, Model seismology: Reports on progress in physics, *in* McDonald, J. A., ed., Seismic physical modeling, 21–53, Soc. of Expl. Geophys., 15 edition. Reprinted from Reports on Progress in Physics, Volume 34, 697-718, 753-764.

Paterson, N. R., 1956, Seismic wave propagation in porous granular media: Geophysics, **21**, 691–714.

Plenkers, K., G. Kwiatek, J. Philipp, S. Stanchits, and J.-G. (2008), 2008, Acoustic emission measurements in a deep gold mine in south africa; spectral analysis (jaguars-project): EGU general assembly 2008, Geophysical Research Abstracts, Expanded Abstracts, EGU2008–A–03682.

Prasad, M. and R. Meissner, 1992, Attenuation mechanisms in sands: Laboratory versus theoretical (Biot) data: Geophysics, **57**, 710–719.

Pride, S. R., J. G. Berryman, and J. M. Harris, 2004, Seismic attenuation due to wave-induced flow: Journal of Geophysical Research, **109**.

Purnell, G. W., 1986, Observations of wave velocity and attenuation in two phase media: Geophysics, **51**, 2193–2199.

Redwood, M., 1960, Mechanical waveguides: The propagation of acoustic and ultrasonic waves in fluids and solids with boundaries: Pergamon.

Rieber, F., 1936, Visual presentation of elastic wave patterns under various structural conditions: Geophysics, **1**, 196–218.

———, 1937, Complex reflection patterns and their geologic sources: Geophysics, **2**, 132–160.

Riznichenko, Y. V., 1994, Seismic modelling, development and outlook, *in* McDonald, J. A., ed., Seismic physical modeling, 4–14, Soc. of Expl. Geophys., 15 edition. Reprinted from Studia Geophysica et Geodaetica, 1966, Volume 10, 243-253.

Savic, M. and A. M. Ziolkowski, 1994, Numerical modeling of elastodynamic radiation and scattering: 64th Annual SEG Meeting, 1294–1297.

Schellart, W. P., 2000, Shear test results for cohesion and friction coefficients for different granular materials: Scaling implications for their usage in analogue modeling: Tectonophysics, **324**, 1–16.

———, 2004a, Kinematics of subduction and subduction-induced flow in the upper mantle: Journal of Geophysical Research, **109**, doi:10.1029/2004JB002970.

———, 2004b, Quantifying the net slab pull force as a driving mechanism for plate tectonics: Geophysical Research Letters, **31**, doi:10.1029/2004GL019528.

———, 2005, Influence of the subducting plate velocity on the geometry of the slab and migration of the subducting hinge: Earth planetary Science Letters, **231**, 197–219.

Schemmann, K., 2008, Scale-related strain evolution at convergent margins and effects due to parameter changes - insights from nature and experiment: PhD thesis, Freie Universität Berlin.

Schmidt, O., 1939, Über Kopfwellen in der Seismik: Z. Geophys., **15**, 141–148.

Schreurs, G., S. J. H. Buiter, D. Boutelier, G. Corti, E. Costa, A. R. Cruden, J. M. Daniel, S. Hoth, H. A. Koyi, N. Kukowski, J. Lohrmann, A. Ravaglia, R. W. Schlische, M. O. Withjack, Y. Yamada, C. Cavozzi, C. D. Ventisette, J. A. E. Brady, A. Hoffmann-Rothe, J. M. Mengus, D. Montanari, and F. Nilforoushan, 2006, Analogue benchmarks of shortening and extension experiments, *in* Buiter, S. J. H. and G. Schreurs, eds., Analogue and Numerical Modelling of Crustal-Scale Processes, 1–27, Geological Society, London.

Sherlock, D. H., 1999, Seismic imaging of sandbox models: PhD thesis, Curtin University of Technology.

Sherlock, D. H. and B. J. Evans, 2001, The development of seismic reflection sandbox modelling: AAPG Bulletin, **85**, 1645–1659.

Sherlock, D. H., J. McKenna, and B. J. Evans, 2001, Time-lapse monitoring of immiscible fluid-flow models: The Leading Edge, **20**, 300–307.

Stanchits, S., S. Vinciguerra, and G. Dresen, 2006, Ultrasonic velocities, acoustic emission characteristics and crack damage of basalt and granite: Pure and Applied Geophysics, **163**, 975–994.

Stoll, R. D., 1977, Acoustic waves in ocean sediments: Geophysics, **42**, 715–725.

Storti, F., F. Salvini, and K. R. McClay, 2000, Synchronous and velocity-partitioned thrusting and thrust polarity reversal in experimentally produced, doubly-vergent thrust wedges - implications for natural orogens: Tectonics, **19**, 378–396.

Talwani, P., A. Nur, and R. L. Kovach, 1973, Compressional and shear wave velocities in granular materials to 2.5 kilobars: Journal of Geophysical Reserach, **78**, 6899–6909.

Tsuboi, C., 1994, Experimental studies on elastic waves, part 2, *in* McDonald, J. A., ed., Seismic physical modeling, 67–78, Soc. of Expl. Geophys., 15 edition. Reprinted from Bulletin of the earthquake Research Institute, 1928, Volume 4, pages 9-20.

Vendeville, B. C., H. Ge, and M. P. A. Jackson, 1995, Models of salt tectonics during basement extension: Petroleum Geoscience, **1**, 179–183.

Wandler, A., B. Evans, and C. Link, 2007, AVO as a fluid indicator: A physical modeling study: Geophysics, **72**, C9–C17.

Weaver, R. L. and W. Sachse, 1995, Diffusion of ultrasound in a glass bead slurry: Journal of the Acoustic Society of America, **97**, 2094–2304.

Wyllie, M. R., A. R. Gregory, and G. H. Gardner, 1958, An experimental investigation of factors affecting elastic wave velocities in porous media: Geophysics, **23**, 459–493.

Wyllie, M. R., A. R. Gregory, and L. W. Gardner, 1956, Elastic wave velocities in heterogeneous and porous media: Geophysics, **21**, 41–79.

Zhang, M. D., D. A. Ebrom, J. A. McDonald, and R. Tatham, 1996, Comparison of experimental velocity measurements with theoretical results in a solid-solid composite material: Geophysics, **61**, 1429–1435.

Appendices

Curriculum vitae

Der Lebenslauf ist in der Online-Version
aus Gründen des Datenschutzes nicht enthalten.